Seismic Structure of the Lower Mantle

Thesis by

Daoyuan Sun

In Partial Fulfillment of the Requirements for the degree of

Doctor of Philosophy

CALIFORNIA INSTITUTE OF TECHNOLOGY

Pasadena, California

2009

(Defended May 26, 2009)

To My Family and All My Friends

Acknowledgements

I am fortunate to have had the opportunity to study in the Seismological Laboratory. My six years of stay have been full of pleasure and challenge. I would like to thank many professors, staff and students for giving me such a wonderful and home-like environment.

Among them, I would first like to express my deep gratitude to my advisor, Prof. Don Hamberger, for his patience, encouragement, and support throughout the research. He cares about me and my future as much as my work. He teaches me to appreciate every wiggle in the seismogram. He always guides me to be an observational seismologist. Life is much easier when I get a note from him every day. Working with him is full of fun. Sitting in his office, laughing at our results and enjoying the mountain view makes the whole afternoon enjoyable.

I owe Prof. Paul Asimow and Prof. Thomas Ahrens my gratitude for their guidance in the first phase of my graduate study. Thank them for explaining the complicate phase diagram and shock experiments to me patiently. I learned from them how to look into the earth from the view of mineral physics.

I also express special thanks to Prof. Rob Clayton, my academic advisor, who helped me in choosing courses and discussions on research. Prof. Mike Gurnis is a constant inspiration for my researches. Regular discussions with the geodynamics group improve my work a lot. Thanks Prof. Jennifer Jackson for sharing her great acknowledge on mineral physics.

Thanks to Prof. Joann Stock, Prof. Jean-Philippe Avouac, and Prof. Jason Saleeby for making all those wonderful field trips a great learning opportunity and learning experience. I enjoyed the classes of Prof. Hiroo Kanamori, Prof. Mark Simons, and Prof. Nadia Lapusta.

I thank Sidao Ni for his continual help, useful programs, and great suggestion on my research. I also thank all the graduate students and postdocs in the lab. It is always nice to talk about earthquake after midnight with Yoshi Kaneko. Collaborations with Ying Tan, Alex Song, Risheng Chu, Dan Bower, and Lijun Liu are full of encouragements. Thanks to Thomas Ader, Laura Alisic, Sarah Minson, Ting Chen, and Zhimei Yan for being the amzing officemates. I learned a lot from them about how to make the desk clean. Ravi Kanda, YoungHee Kim, Ozgun Konca, Lingseng Meng, Francisco Ortega, Kristen Phillips, Carl Tape, and Zhongwen Zhan are pleasant to work with and fun to talk to. As classmates back in college, Huiyu Li, Xiangyan Tian, and Qinya Liu are always good friends.

Special thanks to Viola Carter, Evelina Cui, Donna Mireles, and Sue Yamada for all the help they provided. Thanks to Mike and Ken for all the IT support. I also want to thank Papo Gelle and Michael Long for helping on the shock experiments.

Thanks to all my friends for supporting me as always. I am grateful to Prof. Xingjue Shi, my advisor for undergraduate study in University of Science and Technology of China, for guiding me into geophysics and providing all the help. I also want to thank the GPS soccer team. It’s so great to play a game with a full team under the Southern California sun. Thanks Hsin-Ying Yang for supporting and understanding me, which means a lot to me.

Heartfelt thanks to Min for all her care, encouragement, and constant support for the last several years, which makes my life much easier.

Thanks for my sister and my aunts supporting me all the time. I dedicate this thesis to my parents, who have been working hard to make all the wonderful things happen.

Abstract

The lower mantle plays an important role in the thermal and chemical evolution of the earth. Although recent advanced seismological imaging displays the heterogeneous nature of the lower mantle, most results are constrained to large scale and longer wavelength structures. This thesis involved waveform modeling studies of the detailed structures of the lower mantle, especially the African Superdome and D″ layer.

A simple uniform 3% shear velocity reduction model can explain the observed seismological anomalies for the African Superdome (also refer as Africa Large Low Shear Velocity Province or Africa Superplume), but it lacks small scale complexity inside. In parallel with the seismic model, a composition-dependent compressibility model with a high bulk modulus is developed to explain the African Superdome. To validate this dynamic model, we map the modeled chemistry and temperature into P and S velocity models. Synthetic seismogram sections generated for this 2D model are then compared directly with the corresponding seismic observations. These results explain the anti-correlation between the bulk velocity and shear velocity, as well as the sharpness of the edge.

A lower mantle S-wave triplication with a S_{cd} branch occurring between S and ScS has been recognized for many years and has been interpreted in a variety of ways. The triplication is particularly strong when sampling regions beneath the circum-Pacific lower mantle fast velocity belt seen in global tomographic models, where it has been modeled with a 2–3% jump in S-velocity. The D″ discontinuity may arise from a phase change for Perovskite to Post-Perovskite. We model the phase boundary height by mapping S-wave tomography into temperature. A few adjustable parameters involving reference phase boundary height and velocity jump are determined from comparing synthetic seismogram predictions with densely sampled observations. Adding 3D propagational effects caused by these structures through Perovskite to Post-Perovskite velocity jump predicted from mineral physics appears to generate compatible results with S_{cd} waveform observations.

In the last chapter, we develop a new tool based on a decomposition referred to as a multi-path detector which can be used to distinguish between horizontal structure (in-plane multi-pathing) vs. vertical (out-of-plane multi-pathing) directly from processing array waveforms. A lateral gradient coefficient based on this detector provides a direct constraint on the sharpness of the boundaries and material properties. We demonstrate the usefulness of this approach by processing samples of both P and S data from the Kaapvaal array in Southern Africa. The results further validate the case for distinct chemistry inside the African Superdome. We also present evidence of a narrow plume-like feature coming off the top of the large African low-velocity structure in the lower mantle. The plume's diameter is less than 150 km and consistent with an iso-chemical, low-viscosity plume conduit.

List of Figures

Chapter 1

Introduction

In the last decade, global seismic tomography has produced consistent images of the large-scale structure of the Earth's lower mantle, with a belt of high velocity anomalies along the circum-Pacific and low-velocity anomalies beneath the Pacific Ocean and South Africa. Details of smaller-scale structure, i.e., slabs and plumes, are less well resolved and differ between studies. However, resolution of these structures proves crucial to the understanding of the driving mechanisms of plate-tectonics and mantle convection. Do slabs penetrate into the lower mantle and pile up on the core-mantle-boundary (CMB) [e.g., *Grand*, 2002]? Do plumes rise from the CMB to the surface [*Montelli et al.,* 2006]? These issues remain hotly contested [*Anderson*, 2005]. This thesis presents seismological views of lower mantle structures and tries to answer some parts of those questions.

Synthetic seismograms generated from tomography models generally look like those calculated from the 1D reference model and lack the complexity commonly observed in many seismic sections. Such features require sharp jumps in velocity, ie. steep velocity gradients, which are apparently smoothed out in tomographic imaging because of model parameterization and uncertain source information about location and origin time. While waveform modeling can be useful for resolving strong velocity gradients, there remain many challenges in imaging complete 3D structures because of the lack of data coverage [*Helmberger et al.,* 2005]. The two methods complement each other, and comparing observed waveforms with synthetic seismograms generated for models based on tomographic images can be used as a starting point for sharpening features required to fit the waveform data. We view this process in terms of tomography by providing the large-scale geographic framework for the detailed "gedynamic features" sensed by waveform modeling. We apply waveform modeling to the two major structures in the lower mantle: Large Low Velocity Provinces (Chapter 2 and 4) and the D″ layer (Chapter 3).

The African Superdome has been modeled as a ~1500 km high structure with sharp edges and uniform 3% shear velocity drop inside [*Ni and Helmberger*, 2003a,b,c]. To explain the seismological observations, thermo-chemical dynamic convection models are generated [*McNamara and Zhong*, 2004; *Tan and Gurnis*, 2005]. *Tan and Gurnis* [2005] develop a high bulk modulus model starting with a heavy basal layer with distinct chemistry. Its bulk tabular shape remains relatively stable while its interior undergoes significant stirring with low-velocity conduits along its edges and down-welling near the middle. Given our present limitations in source-station geometry, we will rely more on dynamic modeling in designing seismic experiments to better resolve the small-scale structures inside (Chapter 2). We perform a mapping of chemistry and temperature into P and S velocity variations and replace a seismically derived structure with this hybrid model. Synthetic seismogram sections generated for this high bulk modulus model suggest that this model could be a candidate explanation for the African Superdome.

In a typical tomography model, the D″ discontinuity is not included [*Sidorin et al.*, 1999]. To model the lower mantle triplication [*Lay and Helmberger*, 1983], a positive velocity jump across the D″ discontinuity needs to be added in the tomography models. Based on the phase change boundary explanation for the D″ discontinuity, a global phase boundary height map was generated [*Sidorin et al.*, 1999]. This phase boundary is confirmed by both experimental and theoretical results for the the Perovskite to Post-Perovskite phase change [*Hirose*, 2006]. In Chapter 3, we extend this mapping method to explain the complexities of the Scd phase. By allowing phase boundary mapping with localized parameters derived from tomography image, we can produce the rapid lateral change of the D” discontinuity.

The main advantage of the waveform modeling is to capture structures with sharp edges [*Helmberger et al.*, 2005]. Previous studies concentrated on the 2D in-plane structure. Numerous examples indicate that the structures vary more in azimuth than in distance and that the structure is oriented more vertically than radially [Ni et al., 2005]. *Helmberger and Ni* [2005a] developed a hybrid method to calculate 3D synthetics especially for structures with sharp walls. It is a challenge to distinguish in-plane and out-plane multi-pathing, especially for the large amount of existing array data. In Chapter 4, we introduce a Multi-Path Detector (MPD) that exploits the complexity and resolves sharp structures directly by decomposing the waveform. The array of observations is then replaced by a footprint of timing shifts between interfering arrivals, which indicate where the sharp edges are. In particular, we apply MPD for the array in South Africa to resolve the sharp edge of the African Superdome and provide the evidence of a narrow mid-mantle plume-like feature emitting from the top of the large African Superdome.

Chapter 2

Seismological support for the metastable superdome model, sharp features, and phase-changes within the lower mantle*

2.1 Abstract

Recently, a metastable thermal-chemical convection model was proposed to explain the African Superdome. Its bulk tabular shape remains relatively stable while its interior undergoes significant stirring with low-velocity conduits along its edges and down-welling near the middle. Here, we perform a mapping of chemistry and temperature into P and S velocity variations and replace a seismically derived structure with this hybrid model. Synthetic seismogram sections generated for this 2D model are then compared directly with corresponding seismic observations of P (P, P_CP, PKP) and S (S, S_CS, SKS) phases. These results explain the anti-correlation between the bulk velocity and shear velocity as well as the sharpness and level of SKS travel time delays. In addition, we present evidence for the existence of a D" triplication (a putative phase-change) beneath the down-welling structure.

*This chapter appears as Seismological support for the metastable Superdome model, sharp features, and phase-changes within the lower mantle, Daoyuan Sun, Eh Tan, Don Helmberger, and Michael Gurnis, *Proceedings of the National Academy of Sciences* (2007), 104(22), 9151-9155. doi:10.1073/pnas. 0608160104.

2.2 Introduction

The large-scale structure of the lower mantle has been well resolved by global tomography, with a belt of high seismic velocity along the circum-Pacific and two large low shear velocity provinces (LLSVPs) beneath South Africa and the mid-Pacific. The fastest regions appear to contain a sharp positive velocity jump associated with a phase-change from perovskite (PV) to post-perovskite (PPV) [*Helmberger et al.*, 2005], while the slowest regions contain $\delta V_S/\delta V_P$ ratio > 2.5 and an anti-correlated bulk sound velocity V_ϕ and shear velocity V_S [*Masters G*, 2000; *Su WJ*, 1997]. Although both LLSVPs show these properties, their interior structures appear to differ, with the Pacific anomaly showing more complexity compared to the apparently monolithic African anomaly [*Helmberger and Ni*, 2005b; *Wang and Wen*, 2007]. Tomographic studies of the African structure reveal a large-scale feature which extends throughout the lower mantle. Predicted SKS delay patterns up to 3s for some of these tomographic models fit the observations at the South African seismic array well except for magnitude and sharpness, Figure 2.1, where the data require over 6s offsets [*Helmberger and Ni*, 2005b; *Ni and Helmberger*, 2003a]. Note that the SKS ray paths cross the CMB interface at relatively steep angles and their abrupt change in delays require nearly vertical walls to separate the normal Preliminary Reference Earth Model (PREM) from the anomalous structure denoted by the heavy green lines in Figure 2.1b, review by *[Helmberger and Ni, 2005b]*. Such a structure with its sharp sides is suggestive of thermo-chemical convection containing a density increase [*Ni et al.*, 2002].

2.3 Metastable Superdome

The fate of a dense chemical basal layer in a convecting mantle has a well-developed history [*Christensen*, 1984; *McNamara and Zhong*, 2004]. Their results, involving dense piles, look similar to the LLSVPs in tomographic locations and appear compatible with the history of subduction. Stabilized by an intrinsically larger density ($\Delta\rho_{ch}$), the pile will remain at the CMB until exceeded by a thermal density with opposite sign ($\Delta\rho_{th}$). However, if there is a difference in compressibility between the materials within the plume compared to ambient mantle, then metastable conditions are possible. *Tan and Gurnis*, 2005 have generated a sequence of models with differences in zero pressure density ($\Delta\rho_o$), adiabatic bulk modulus (*Ks*) and initial layer thickness. They show that if $\Delta\rho_o$ is 2 to 3% and *Ks* from 4 to 8% larger than the ambient mantle, which are expected for material from subducted slabs (pyroxenite) [*Lee et al.*, 2005], then metastable superdomes can form. The result that best matches the seismic data for the African Superdome, labeled HBMS (High Bulk Modulus Structure), is used in our subsequent analysis (Figure 2.2).

At the base of the mantle, the anomalous material heats, becomes more buoyant than the background, and moves upward. However during ascent, its buoyancy gradually decreases, due to an increasing adiabatic density difference, and rises to a level where it is neutrally buoyant, height of neutral buoyancy (HNB). Above the HNB, the anomalous material becomes denser than the background and sinks. The structure stands high above the CMB (Figure 2.2) and remains metastable depending upon the equation of state and depth-dependence of the coefficient of thermal expansion [*Tan and Gurnis*, 2005].

The existing seismic model of the African Low Velocity Structure (ALVS, Figure 2.1) is similar in shape to the dynamic models but lacks smaller scale complexity and low seismic velocities near the edges. Such features are in some of the seismic models presented by [*Wen*, 2001]. The earlier idealized seismic structure (Figure 2.1b) has a uniform 3% V_S reduction with walls and a flat roof, so that the general character of the anomaly might be imaged more clearly with waveform data available, transforming the blurry tomographic model into this distinct structure [*Ni and Helmberger*, 2003c].

We convert the temperature, composition, and density anomalies in HBMS model to seismic velocity anomalies in favoring the bulk properties of the seismic African Superdome model. The thermo-elastic parameters of the chemical anomalous material are chosen to be similar to those of $MgSiO_3$ perovskite. In the HBMS model, the conversion from temperature (T) and composition (C) to seismic velocities is based on the following parameters:

$$\left(\partial \ln K_S / \partial C\right)_T = 6\%$$

$$\left(\partial \ln \mu / \partial C\right)_T = 1.5\%$$

$$\left(\partial \ln K_S / \partial T\right)_C = -6\%$$

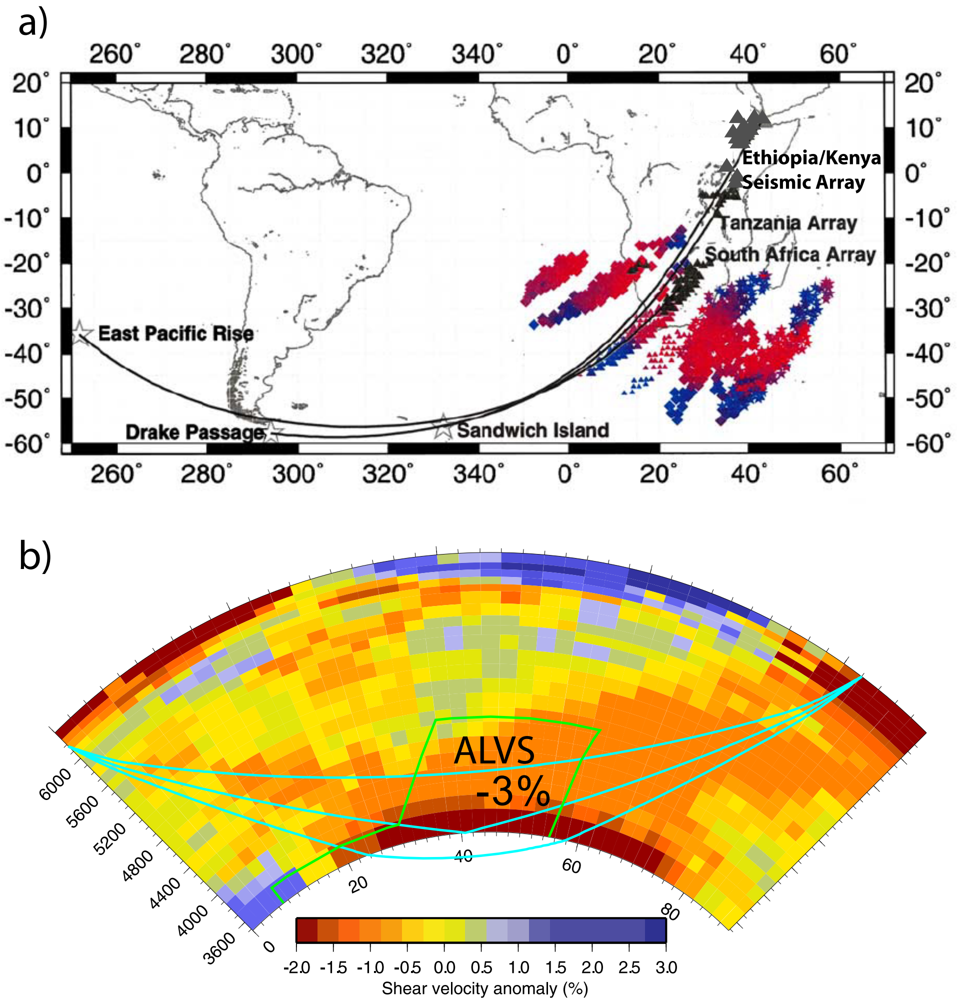

Figure 2.1: A map of events and stations (triangles) used in the construction of a 2D model along a corridor through the African Superdome. We use data from two arrays, South African, and the new Ethiopia/Kenya array [*Langston et al.*, 2002] of events arriving along a great circle in this study. SKS and SKKS exist points at the CMB are given in colored triangles, with blue indicating no delay and red over 5s. To produce the sharp jumps require a monolithic structure denoted in heavy green lines as the African Low Velocity Structure (ALVS), where the S velocity inside the box is reduced by 3% relative to PREM [*Ni and Helmberger*, 2003a]. We have included some example ray paths S, SKS, and S_CS. The background tomographic model is most recently updated *Grand's* model [*Grand*, 2002].

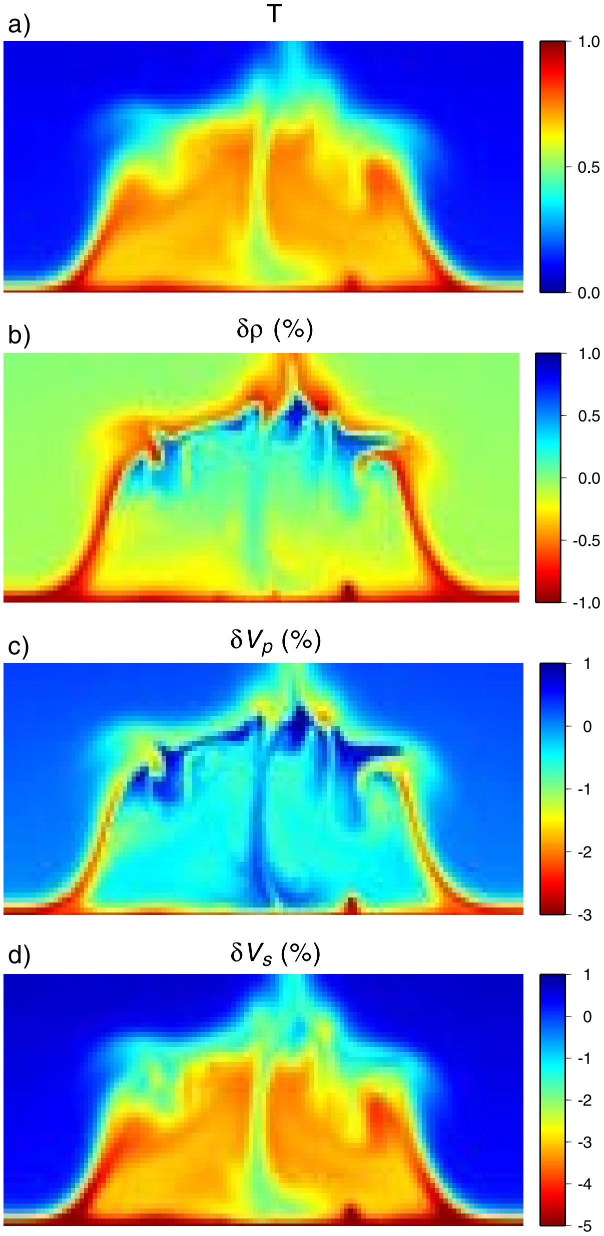

Figure 2.2: Display of a 2D section through a metastable thermo-chemical structure along with predicted V_P and V_S velocities [*Tan and Gurnis*, 2005]. Only the bottom 1200 km of the model is shown. Within the anomaly, the material has a larger bulk modulus (6% larger than ambient) and higher zero pressure density (2.25%). The layer forms a single dynamic structure with the average density near neutral. Note the plumes along the edges and the down-welling near the middle. a. Non-dimensional temperature, b. density anomaly, c. V_P anomaly and d. V_S anomaly.

$$\left(\partial \ln \mu / \partial T\right)_C = -15\%$$

Here, Ks is the bulk modulus, and μ is the shear modulus. The value of $(\partial \ln Ks/\partial C)_T$ is dictated by the dynamic model. The value of $(\partial \ln \mu/\delta C)_T$ is a free parameter and is chosen to fit the seismic observation. When scaled, the dimensional values of $(\partial \ln Ks/\partial T)_C$ and $(\partial \ln \mu/\partial T)_C$ used in the conversion are -3.33x10^{-5} K^{-1} and -8.33x10^{-5} K^{-1}, respectively. More information about the conversion is described by Tan and Gurnis [2007]. For reference, the dimensional values of $(\partial \ln Ks/\partial T)_C$ and $(\delta\mu/\delta T)_C$ for $MgSiO_3$ perovskite are calculated to be -3.29x10^{-5} K^{-1} and -8.62x10^{-5} K^{-1}, respectively [*Oganov et al.*, 2001].

2.4 Predicting Seismograms

Here, synthetic seismograms generated from dynamically derived V_S and V_P models are tested against observed seismic phases and travel times. These synthetics were generated with the WKM technique introduced in [*Ni et al.*, 2000]. The method is basically analytical, which satisfies the wave equation assuming tomographic-type models. The original idea of WKM was proposed by Wiggins and Madrid [1974] based on the comparison of 1D synthetic seismograms generated by complete methods against simple geometric approximations. The first step is to generate the ray paths for the 1D reference model, as in seismic tomography. We compute the ray paths reflecting-off every interface sampling the depth sensitivity of the seismic phase. The ray parameter (p_i) and the travel time (t_i) are used to form a numerical derivative

$$\frac{dp}{dt} = \sum_i \left(p_i - p_{i-1}\right) / \left(t_i - t_{i-1}\right). \tag{2.1}$$

In most tomography, the value of p_i is held fixed along each ray segments and the t_i can vary by adding velocity changes to blocks in various layers. Thus, the ray paths do not change as the velocity is perturbed. We go beyond this approximation by allowing the p_i to satisfy Snell's law again in the perturbed heterogeneous model and compute corresponding changes made in the ray segments. Note that the paths will shift to avoid slow regions (see

Ni et al. [2003]) for a validation study against numerical methods). In general, thin layers increase the accuracy.

To test the HBMS model, we replace the box-like structure (Figure 2.1b) with the HBMS structure (Figure 2.3a), while assuming the same geometry for events and stations and then generate 2D synthetics. Then we compare the predicted synthetic seismograms with the observed seismic data. Specifically, (i) does HBMS display the sudden jump in SKS at the edges and remain relatively flat over extended distances while generating complex SKS waveform when sampling the edges; (ii) does HBMS satisfy the travel time data of diffracted S wave (S_d) and diffracted P wave (P_d), where S_d is delayed much more than P_d; and (iii) does it predict the much larger delayed S_CS−S than P_CP−P. We find that HBMS predicts the bulk characteristics about as well as the idealized seismic model (Figure 2.1b) but also predicts small-scale features near the edges and middle which can be seen in the observed waveform data.

Although the early waveform studies of the African Superdome revealed sharp features based on differential phase relationships (SKS-S and S-S_CS) [*Ni and Helmberger*, 2003a; b; *Ritsema et al.*, 1998], the dense regional array data provided the most definitive evidence [*Wen*, 2001]. Thus, we will concentrate on array data and 2D synthetics generated from

Figure 2.3: This figure presents seismic waveforms predicted by inserting the HBMS model into the earth beneath Africa, essentially replacing Figure 2.1b by Figure 2.2d, and comparing results against seismic observations. We have included the ALVS (Figure 2.1b) results for comparison. Figure 2.3a displays the geometry and geometric ray paths along a 2D cross-section (East Pacific Rise to the South Africa Array) sampling the anomalous structure, SKS (red) and S_d (light blue). Figure 2.3b displays the differential timing derived by cross-correlating the observed waveforms [*Helmberger and Ni*, 2005b], with synthetics relative to predictions from the 1D reference earth PREM. Since the structure is roughly symmetric, we included predictions with events occurs at the left side (heavy line) and the right side (light line) of this model. A comparison of travel time predictions generated from HBMS synthetics against those observed at the South Africa Array [*James et al.*, 2001] are displayed in Figure 2.3c for diffracted S (S_d, solid triangles) and P (P_d, open triangles). Since the diffracted waves sample the top-edge of the structure first, the anomalous travel times have a gradual onset as predicted by the solid curves, heavy from the left, light from the right. Both the data and synthetic predictions display considerable scatter indicative of possible embedded fine-structure which is likely to be time-dependent. However, the magnitude of the anomalous S delays relative to P is well matched.

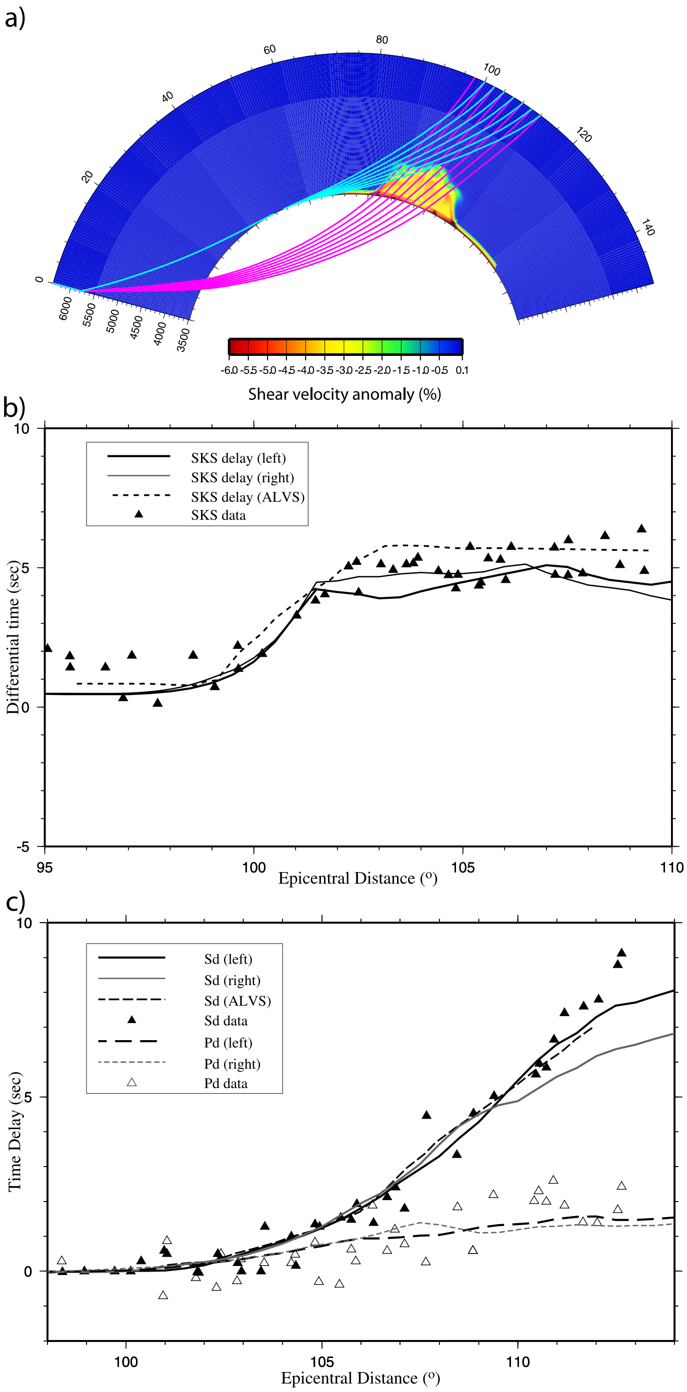
a)
0
20
40
60
80
100
120
140
6000
5500
5000
4500
4000
3500
-6.0 -5.5 -5.0 -4.5 -4.0 -3.5 -3.0 -2.5 -2.0 -1.5 -1.0 -0.5 0.1
Shear velocity anomaly (%)
b)
SKS delay (left)
SKS delay (right)
SKS delay (ALVS)
SKS data
Differential time (sec)
10
5
0
-5
95
100
105
110
Epicentral Distance (°)
c)
Sd (left)
Sd (right)
Sd (ALVS)
Sd data
Pd (left)
Pd (right)
Pd data
Time Delay (sec)
10
5
0
100
105
110
Epicentral Distance (°)

Figure 2.3

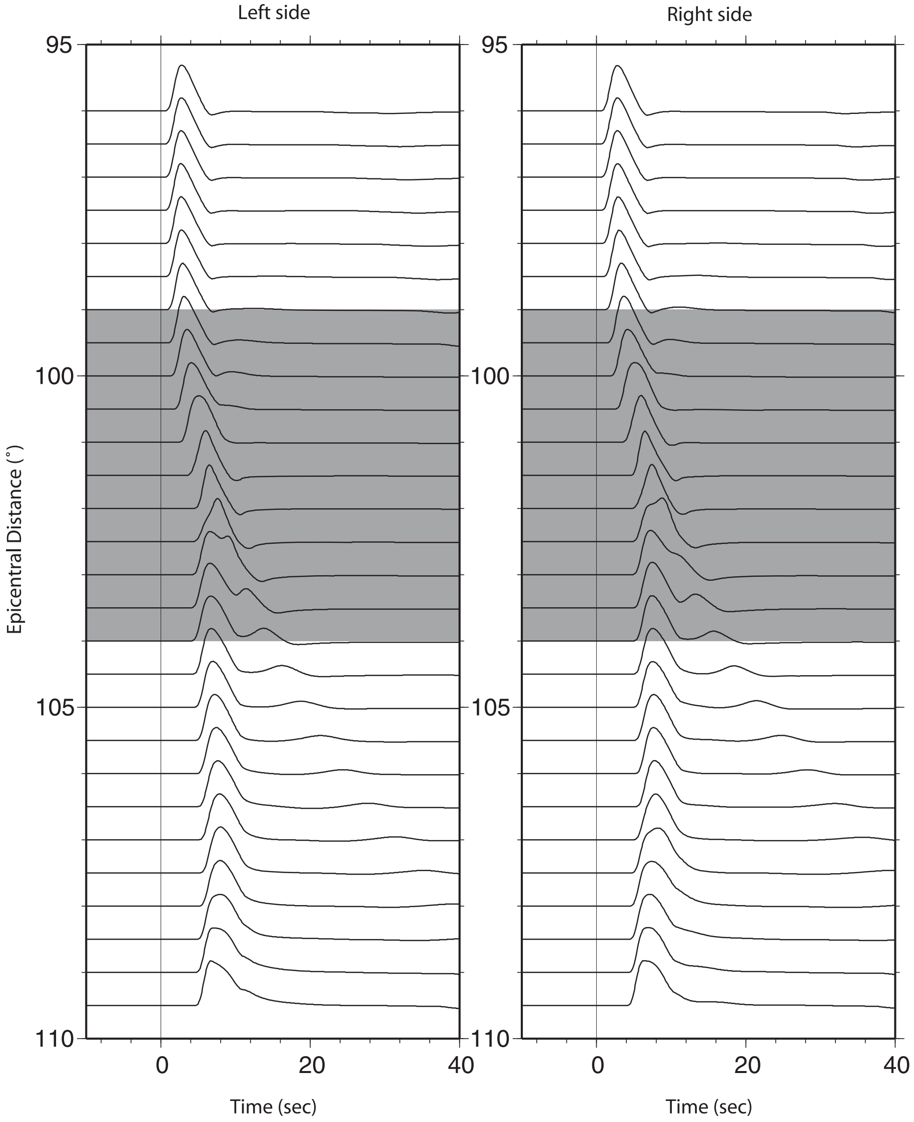

Figure 2.4: The figure presents SKS waveforms predicted for the HBMS model. The predictions with rays from both sides show a rapid delay of SKS and waveform complexity when sampling the boundary zone (shaded zone). The SKS ray paths are shown in Figure 2.3a.

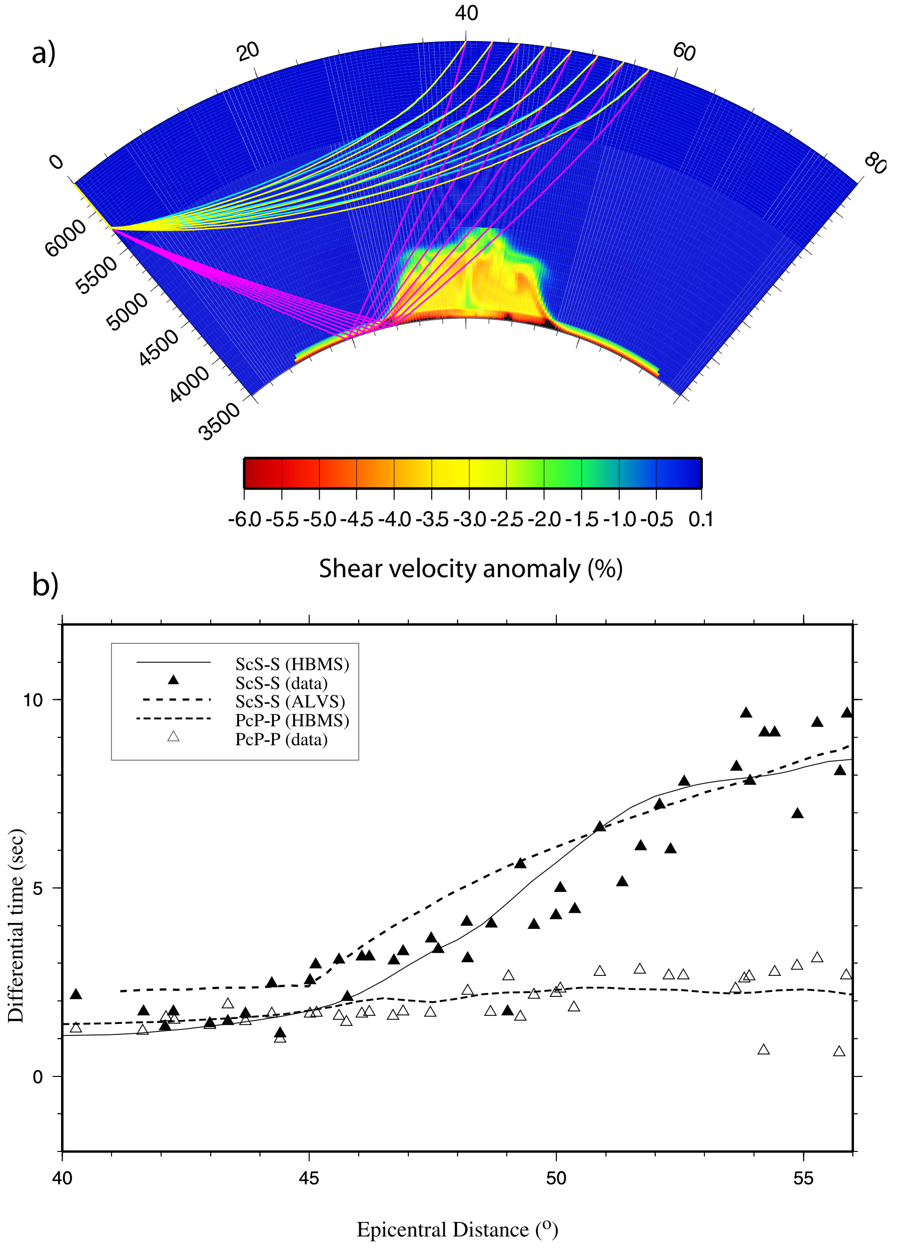

Figure 2.5: Comparison of S_CS-S and P_CP-P predictions with observations [*Helmberger and Ni*, 2005b]. a) The ray paths of S_CS (mangenta), S (cyan) and P (yellow) are shown sampling the HBMS model. b) Comparison of differential S_CS-S (solid line) and P_CP-P (dot line) predicted by the HBMS and ALVS models. The modeled P_CP-P differential time is shifted up by 1s, considering the possible base-line shift for origin time correction.

events along the great circle paths displayed in Figure 2.1a. Synthetic waveforms for the HBMS model are processed using the same procedure as used in deriving Figure 2.1b, with results displayed in Figure 2.3. We also included reversed paths or flipping the HBMS model since the detailed velocity field is not unique, i.e., changes with time, etc. The HBMS results fit as well as ALVS although a few seconds of scatter remain. The synthetics are displayed in the Figure 2.4 where complexities develop near the boundary as can be observed [*Ni et al.*, 2002], but these features remain difficult to quantify.

Long-period P-wave diffraction (P_d) that passes through the African anomaly is less delayed than S_d from conventional tomography. This is most easily measured by comparing synthetic seismograms (PREM) against data [*Ni and Helmberger*, 2003a; b]. To avoid source location uncertainties, we compare Pd and Sd from the same event, Figure 2. 3c. The geometry is presented in [*Ni and Helmberger*, 2003b], where the phases cross the boundary nearly at right angles to the structure. The observations display considerable scatter since the array is broad and the ray paths apparently encounter 3D variation, i.e. samples from the right side are about 1.5s smaller than those from the left. In short, the dynamic model captures some of this level of observed variation indicative of a convecting region.

There are many advantages in sampling an unknown structure with paths following the same great circle as described earlier (Figure 2.1a). Here we display S_CS-S and P_CP-P for a Sandwich Island event (Figure 2.5). The P and S direct rays encounter gentle mantle structures as explored with various tomographic maps [*Ni and Helmberger*, 2003b]. Thus, the differential times remove the timing errors associated with origin time and location and provide an accurate differential measure between the P and S velocities inside the anomalous structures. Note that the SKS delays fix the position of the wall, simplifying the interpretation of the S_CS-S delays and their increase with distance. The data scatter relative to the model similar to the S_d suggesting complexity in the upper boundary.

2.5 Possible phase boundary

While Sandwich Island events produce excellent P_CP and S_CS recording on the South African Array, they also produce samples of the CMB directly below South Africa (Figure

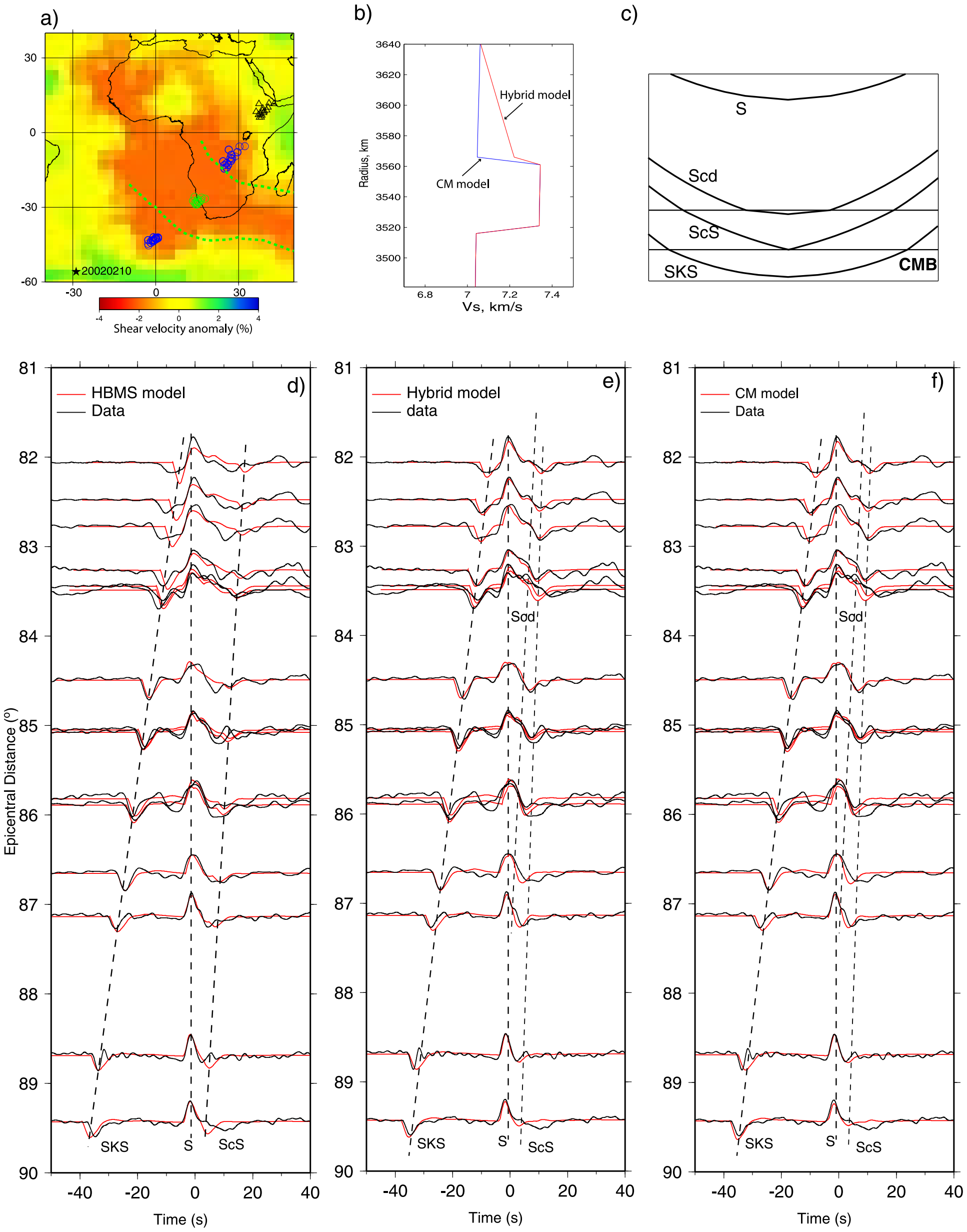

Figure 2.6: Modeling a D" triplication from the Ethiopia/Kenya array from a deep Sandwich Island event; (a) The recording geometry with green circles indicating the S_CS sampling points at the CMB. (b) We assume the ALVS inside the Green Box in Figure 2.1b is 1D and replace the velocities near the bottom with our preferred structure (b). We have included a model with a sharp 4% jump (CM) and a hybrid model. (c) displays geometric ray paths with arrival times given as lines on the data-synthetic record sections; (d) displays the comparison with observed waveforms against predictions from the HBMS model and (e) those from the Hybrid model and (f) CM model containing structure (b).

2.6) as recorded by the recently released Ethiopia/Kenya array data [*Langston et al.*, 2002]. Since this dataset is rather unique, we will display the record section and predictions from both the ALVS and HBMS models and suggested model changes involving a possible PV to PPV phase change. The geometry is shown in Figure 2.6a where SKS piercing points are denoted at the edges of the Superdome. The boundaries as discussed earlier are given as heavy dashed green lines. The S_CS bounce points are near the center of the structure where the down-welling developed in Figure 2.2d. Record sections display the waveforms containing the various seismic arrivals with SKS arriving first followed by S and ending with S_CS. The cross-over from S to SKS occurs about 2° early relative to PREM because of the delayed S, which is common for the African anomaly.

Because of some small station timing offsets, record sections relative to predicted PREM times have small misalignments, which can be avoided by aligning directly on the peak of the S pulse as displayed in the record sections Figure 2.6d)–f). Synthetic prediction for HBMS reproduces observed arrivals reasonably well, except that the differential time between S and SKS is small at smaller ranges and S_CS is late and complicated.

Both the HBMS model and Ni's model (Box I) (Figure 2.7) can not produce the large separation between S and SKS at small distances (82 ~ 84°) (Figure 2.8a, b). Adding the extra Box II in Figure 2.7, with the 2% velocity reduction, slows the arrival time of S and has no effect on the SKS phase, and produces the observed differential time between S and SKS in Figure 2.8c.

In addition, there is a small arrival between S and S_CS having the timing expected for the Scd phase. This extra arrival is produced by a small triplication near the CMB which appears between S and S_CS at ranges 80° to 90° [*Helmberger et al.*, 2005]. Because HBMS does not have such a phase boundary, we experimented with the original ALVS structure, Figure 1b. A significant feature in the HBMS model is the down-welling region near the center, which will cause a diffuse increase in seismic velocity. Then we added a linear gradient to mimic the down-welling followed by a small velocity jump (1.7%), a strategy used earlier by [*Sidorin et al.*, 1998]. We conducted a grid search to derive the Hybrid model (Figure 2.6b) and synthetics displayed in Figure 2.6e. The small pulse with a phase velocity slightly higher than S labeled Scd is associated with this sharp boundary. We also

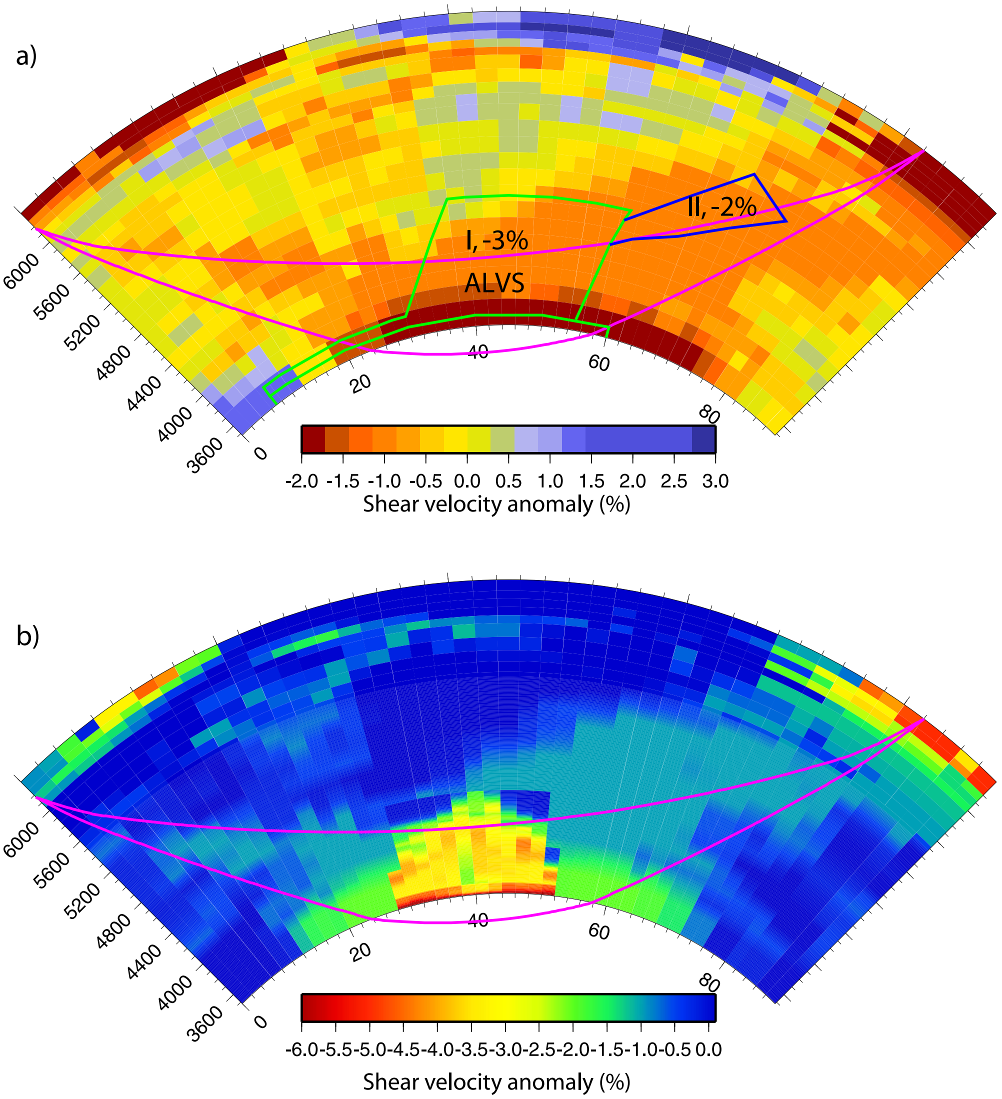

Figure 2.7: The cross sections from South Sandwich Island to the Ethiopia/Kenya array for a) Hybrid model and b) HBMS model with background Grand's tomography model. In the Hybrid model, the S velocity anomaly inside the Box I is -3% and -2% inside Box II. The second Box II was added to fix the relative SKS and S timing issue by slowing S as can be seen in the ray path sampling. This is not unique and any extra S delays along these particular paths will satisfy the data.

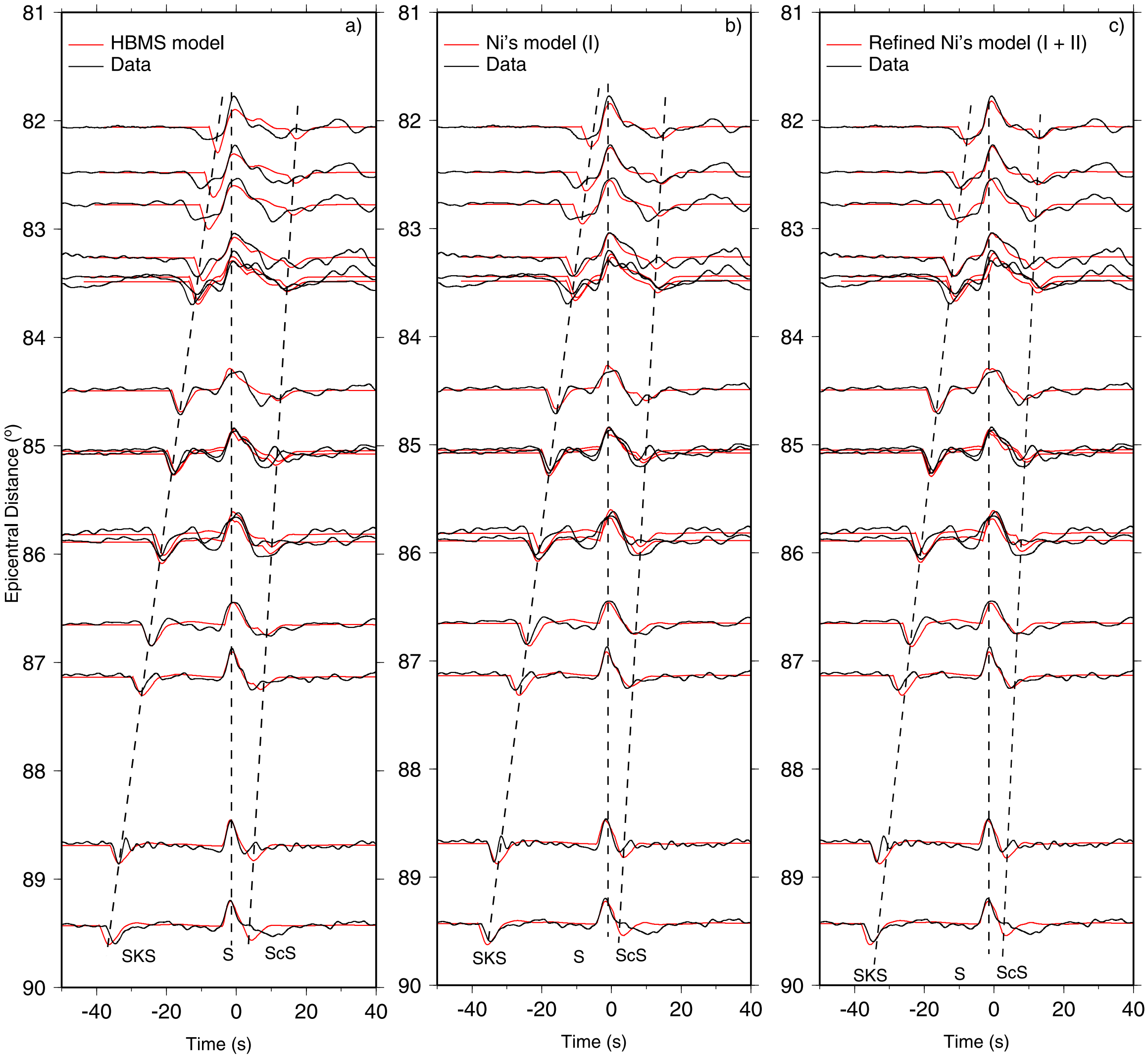

Figure 2.8: The comparison with observed waveforms against predictions from the a) HBMS model. In b), only Box I in Figure 2.6 is enhanced. Both Box I and II are enhanced in c).

test a model with an abrupt shear velocity jump across the boundary. By grid search, we derive a model (CM model) with 4% jump located 100 km above the CMB, Figure 2.6b. The synthetics for this model are shown in Figure 2.6f. Both models provide a reasonable fit to the data. The small velocity jump in the Hybrid model supports the possible PV to PPV transition across the boundary seen globally. Since the down-welling in the HBMS model raises the possibility of the occurrence of phase transition in this area, we prefer the hybrid interpretation.

The overall fattening of S at ranges 83° to 87° is caused by the high velocity gradient which is also present in the HBMS model. Unfortunately, it proves difficult to sample D" beneath the Superdomes because of the strong constraints of station geometry. Thus, we do not know if the structure presented is related to the down-welling, or perhaps PPV to PV. Note that *Tsuchiya and Tsuchiya* [2006] suggest that the PV to PPV transition for Fe-rich chemistry is likely to be accompanied by a negative V_S jump [*Tsuchiya and Tsuchiya*, 2006]. This implies that a positive V_S jump then becomes a PPV to PV transition. The position and the magnitude of the negative velocity jump beneath the boundary is not well constrained, although adjustments can be made to correct the travel time of S_CS. Because a velocity reduction is more difficult to detect than a velocity increase [*Flores and Lay*, 2005; *Sun et al.*, 2006], there is no constraint on the exact velocity structure below the boundary of the positive velocity jump in both models. However, considerable support for a positive velocity jump comes from studies near the Pacific Superdome edge [*He et al.*, 2006; *Lay et al.*, 2006], along with very strong lateral variations in S-velocity structure, Figure 2.9. Strong variation in P-velocities has also been found near this same edge [*Luo et al.*, 2001].

2.6 Edge Effects on P-waves

The P-wave velocity structures in HBMS are not anomalous on average as pointed out earlier with respect to P_d. Moreover, the phases with nearly vertical ray paths in the mantle have the best chance of detecting the abrupt lateral changes near the edges, in particular the differential branches of PKP phases. Although the V_P anomalies are small for the LLSVPs on average, the existence of sharp V_P features occurring near their edges is poorly imaged seismically because of the lack of differential phases. P_CP-P is not available for distances

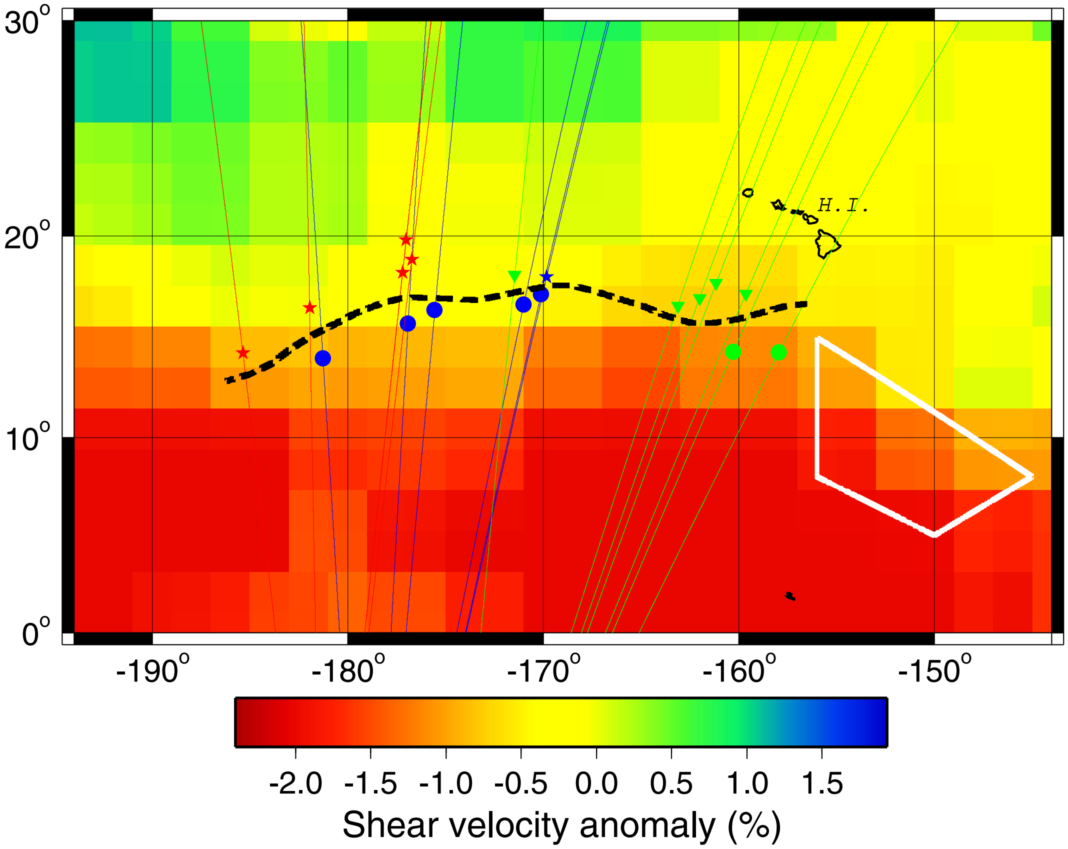

Figure 2.9: Map of the northern edge of the Pacific Superdome displaying where anomalous seismic data has been studied relative to Grand's tomographic model (after Luo et al, 2001). The piercing points of PKPab three Fiji-Tonga events, red, green, and blue, are indicated relative to a dotted line where the dotted PKP arrivals are 2s earlier than those to the north. The symbols indicted by asterisk or triangles are locations where PKPab display complexities (multi-pathed). The white trapezoid region shows rapid lateral variation of D" [*He et al.*, 2006].

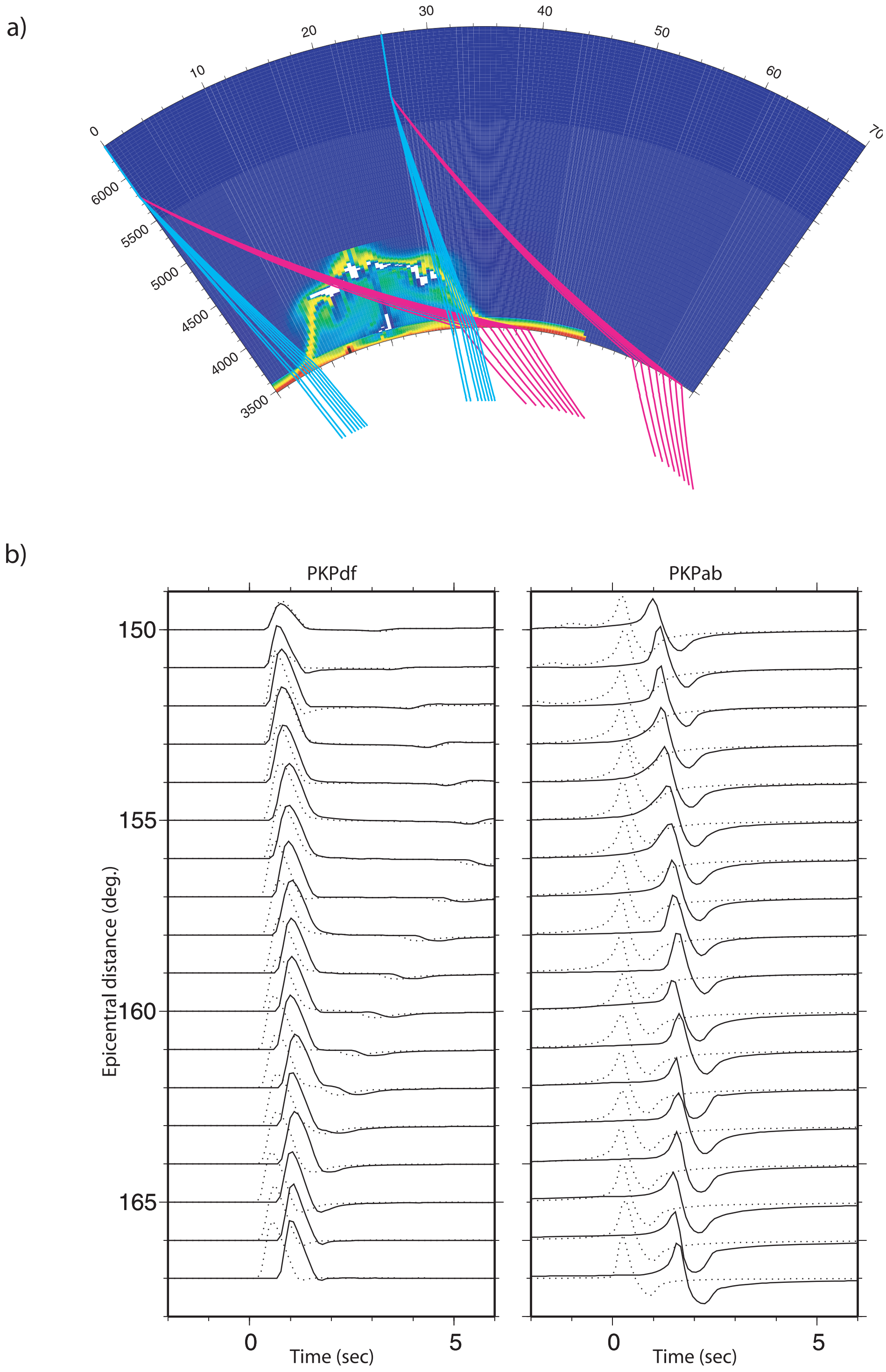

Figure 2.10: Display of ray paths for PKP, PKPdf in cyan, and PKPab in magenta, for geometrics sampling the edge structures relative to PREM along with synthetic predictions. Solid traces correspond to the edge structure with dotted traces relative to PREM. Note the nearly 2s offset caused by sampling the edge structure.

beyond 70° where the reflection coefficient (P_CP) becomes very small. Differential times, δt_k, between PKPab and PKPdf has proven useful in studying D" with some success [*Song and Helmberger*, 1993]. Since the AB and DF paths only separate in the lower mantle, see Figure 2.10, their δt_k becomes a useful measure of lateral variation. Due to the limited samples for African Superdome, we examine the PKP sample beneath Central Pacific. Some sharp jumps in δt_k have been observed with no obvious explanation (Figure 2.9). Figure 2.9 displays the CMB piercing points for the phase PKP(AB) for events beneath the Tonga-Fiji Islands as recorded in Spain [*Luo et al.*, 2001]. The dotted line in Figure 2.9 separates normal arrival times from late arrivals (2s). It appears that these jumps in δt_k can be explained by the anomalous edge structure along the HBMS. Moreover, many observations north of the dotted line in Figure 2.9 display waveform complexities which can be modeled by including ultralow velocity zone (ULVZ's) [*Luo et al.*, 2001]. The most probable cause of the ULVZ is partial melting at the base of the mantle [*Garnero et al.*, 1998]. Although the HBMS model did not include the melting process, the edges of the HBMS are substantially hotter than elsewhere, which become candidate locations for such zones.

2.7 Summary

In conclusion, we have tested a dynamic model HBMS by mapping excess T and density into V_P and V_S and comparing data against predicted synthetics. Not only did the dynamic model predict accurate results generated from the model, it suggests additional features that appear to be observable, such as plumes along the edges and a fast lens near the CMB, D". An observed record section sampling beneath the Superdome can be modeled by assuming a velocity gradient (fast lens) and a 1.7% jump in S velocity situated 90 km above the CMB. However, since the above mapping is strongly dependent on assumed perturbations of the shear modulus to changes in T and composition, we have a self-compatible model which lacks uniqueness. The next step is to add the mineral physics constraints and retest all the appropriate datasets. We will then be in position to better understand the dynamics behind some of the largest coherent structures in the mantle.

Chapter 3

Lower Mantle Tomography and Phase-change Mapping *

3.1 Abstract

A lower mantle S-wave triplication (Scd) has been recognized for many years and appears to be explained by the recently discovered Perovskite (PV) to Post-Perovskite (PPV) phase-change. Seismic observations of Scd display (1) rapid changes in strength and timing relative to S and ScS, and (2) early arrivals beneath fast lower mantle regions. While the latter feature can be explained by a Clapeyron slope (γ) of 6 MPa/K and a velocity jump of 1.5% when corrected by tomographic prediction [*Sidorin et al.*, 1999], it does not explain (1). Here, we expand on Sidorin's mapping approach by attempting a new parameterization that requires a sample of D" near the ScS bounce point where the phase height (h_{ph}) and velocity jump (β) are functions of shear velocity perturbation (δV_S). These parameters are determined by modeling dense record sections collected from USArray and PASSCAL data where Grand's tomographic model is the most detailed in D" structure beneath Central America. We also address the range of γ to generate new global models of the phase boundary and associated temperature variation. We conclude that a γ near 9 MPa/K is most

* This chapter appears as
Complexity of D" in the presence of slab-debris and phase changes, Daoyuan Sun, Teh-Ru Alex Song, and Don Helmberger, *Geophysical Research Letters* (2006), 33, L12S07, doi:10.1029/2005GL025384.

Lower mantle tomography and phase change mapping, Daoyuan Sun and Don Helmberger, *Jounral of Geophysical Research* (2008), 113, B10305, doi:10.1029/2007JB005289.

satisfactory but requires β to be non-uniform with a range from about 1.0 to 4.0% with some slow region samples requiring the largest values. Moreover, the edges of the supposed buckled slabs deliminated by both P and S-waves display very rapid changes in phase-boundary heights producing Scd multipathing. These features can explain the unstable nature of the Scd phase. The fine structure at the base of the mantle beneath these edges contains particularly strong reflections indicative of local ultralow velocity zones, which are predicted in some dynamic models.

3.2 Introduction

Large-scale structures in the lower mantle derived from numerous tomographic imaging consistently show a belt of high velocity anomalies along the circum-Pacific (Figure 3.1a). Low velocity anomalies beneath the mid-Pacific and Africa are also well established although with smaller-scale plume-like features which remain controversial [*Anderson*, 2005]. Relatively sharp features have been reported at mid-mantle depths beneath North America which appear to be slabs [*Grand et al.*, 1997], and many researchers interpret the high velocity ring (Figure 3.1a) as slab debris, e.g., review by Garnero, [2004] and van der Hilst, [2004]. The deep earthquakes occurring in the down-going slabs produce simple isolated body wave phases (P and S) which can be used to study the smaller-scale features. In particular, secondary arrivals can be seen between S and ScS forming a small triplication, roughly 75° to 85° (Figure 3.2). These arrivals can be commonly observed on recording stations (continental paths) sampling the fast Pacific Ring as first pointed out by *Lay and Helmberger* [1983]. The position of the triplication relative to S and ScS appears to vary regionally with the earliest occurring beneath eastern Asia [*Wysession et al.*, 1998]. This depth-dependence of Scd triplications was used to attempt a phase-change interpretation by [*Sidorin et al.*, 1998] in terms of a positive Clapeyron slope. He imposed a velocity jump defined by

$$V'(h,\theta,\phi) = V(h,\theta,\phi)\left\{1 + \frac{1}{2}\beta\left[1 + tanh\left(\frac{1}{w_{ph}} r_{ph}\right)\right]\right\} \tag{3.1}$$

where *V(h)* is the original tomographic velocity at the elevation h above the CMB, *V'* is the new velocity, β is the amplitude of the velocity jump, θ is the latitude, and ϕ is the longitude. The width of the phase transition is w_{ph} which was assumed to be 5 km in Sidorin's efforts based on upper mantle studies. This sharpness produces a clear Scd in synthetics as displayed in Figure 3.2c and d, while a broad transition produces a gradual long-period onset (Figure 3.2b). A simple break in the velocity gradient (Figure 3.2a) produces only a long-period diffraction not easily seen at typical periods used in these studies. The r_{ph} in Equation (3.1) is defined by

$$r_{ph}(h,\theta,\phi) = h_{ph} - h(\theta,\phi) - \frac{\gamma}{\rho(h,\theta,\phi)g(h)}\Delta T(h,\theta,\phi) \qquad (3.2)$$

where g is the gravitational acceleration in the mantle. ρ is the density, which is assumed to be same at different locations with the same depth of h here. ΔT is the non-adiabatic temperature perturbation.

$$\Delta T(h,\theta,\phi) = -2\frac{\Delta V(h,\theta,\phi)}{\alpha(h)V_{PREM}(h)(\Gamma - 1)} \qquad (3.3)$$

ΔV is the velocity perturbation in tomographic model. $\alpha(h)$ is the depth- dependent coefficient of thermal expansion. Γ characterizes the temperature dependence of the shear modulus in the mantle. We concentrated on changes in β and h assuming $\Gamma = 6$. The phase elevation above CMB for the reference 1D model is defined by h_{ph} where the velocity jump occurs. Thus, only three parameters were needed to perform the mapping (Figure 3.1b), namely, β, h_{ph}, and γ. *Sidorin et al* [1999] calibrated this model to the Scd triplication data by matching the differential times (Scd – S) for various regions around the circum-Pacific. A 2D synthetic for each source-station pair was used to determine the h_{ph} and γ for each region following a least-square modeling procedure. The velocity jump β = 1.5% was assumed as the smallest possible jump to explain Scd in fast regions and thus help to explain the few values reported beneath warm regions [*Wysession et al.*, 1998]. To preserve the ScS-S differential times used in deriving Grand's model, Sidorin et al [1999] inserted a low velocity zone just above the CMB as part of the mapping procedure.

Two major advances have occurred since this interpretation of the Scd phase data; one in mineral physics and the other in the advance of broadband seismic arrays. The obvious

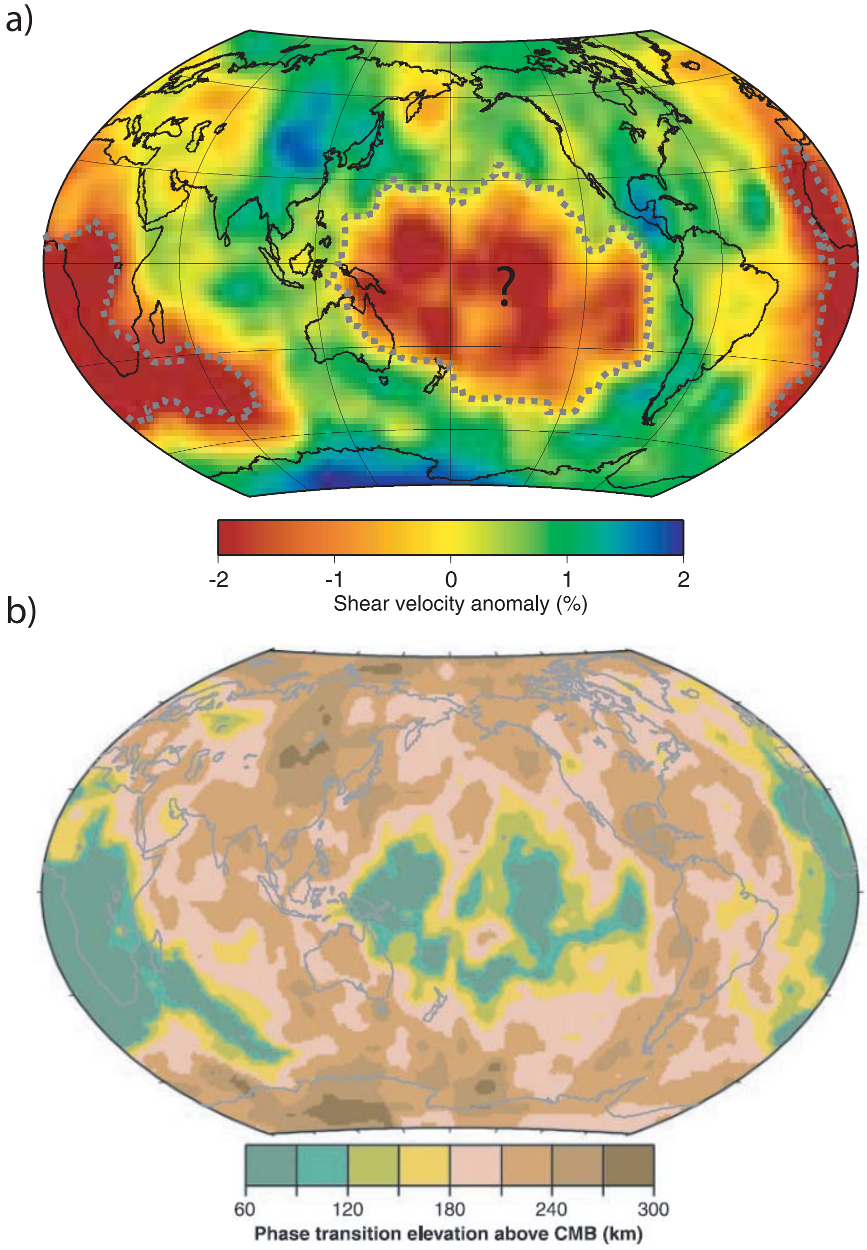

Figure 3.1: Display of tomographic results from *Grand* [2002] along with possible mapping into thickness of a proposed post-perovskite layer at the CMB. a) contains the bottom 240 km layer variation in shear wave velocity. b) displays a map of a possible phase boundary discontinuity constructed from a) assuming that temperature can be deduced from these shear velocity variations (δVs) and uniform global chemistry with $\gamma =$ 6 MPa/K [*Sidorin et al.*, 1999].

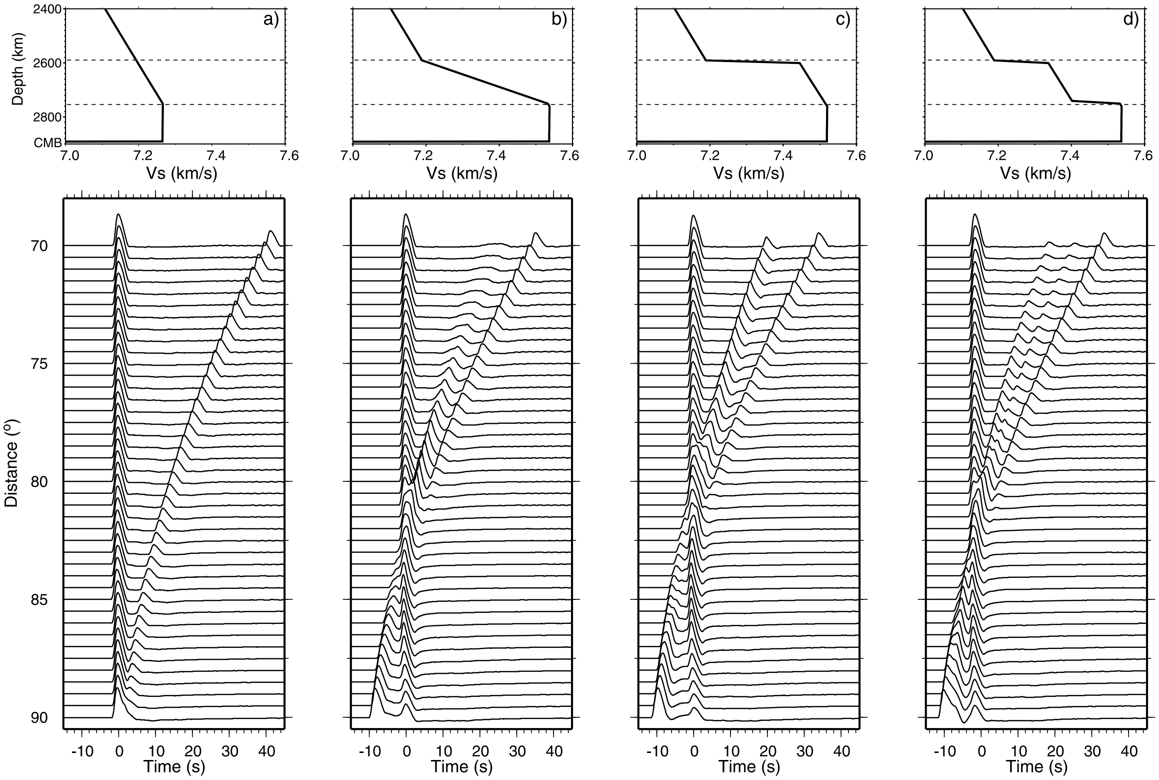

Figure 3.2: The synthetics for possible 1D models of D". a) is the PREM model and the synthetics do not have the Scd phase. b) includes a linear velocity gradient and produces the extra Scd phase between S and ScS. c) has a sharp velocity jump plus a gradient, and d) has two sharp velocity jumps in the model, simulating a complex transition zone.

major breakthrough was the direct experimental evidence for a post-perovskite phase transition under conditions close to those at the D" region [*Murakami et al.*, 2004]. Highlights of this discovery have been given by several authors [*Duffy*, 2004; *Garnero*, 2004]. Numerous studies, both theoretical and experimental, indicates that a phase transition with a positive γ should occur near D" with a velocity jump between 1.5 to 3% but perhaps over a 150 km zone depending on chemistry, e.g., review by Hirose [2006]. Although the details about this phase boundary (velocity jump, phase transition thickness, etc) are extremely important in interpreting Scd data as evident in Figure 3.2, they remain largely unknown.

The second issue of modern arrays and their impact on D" is rapidly becoming apparent as discussed in Lay and Garnero [2007]. While Sidorin et al. [1999] averaged over regions treating variations as noise to obtain smoothly varying structure, recent studies by Hutko et al. [2006], Sun et al. [2006] and Kito et al. [2007] suggest rapid jumps in the phase boundary height occurring laterally over short-scale lengths of 50 km to 100 km. Are such features caused by buckled slabs since they occur near the edges of sharp structures or are they caused by phase boundary shifts induced by chemical changes or perhaps a combination? The greatly improved station coverage has also allowed better sampling and resolution of P-velocity structure. Since the predicted phase-change properties for P-waves are nearly negligible, such data becomes useful in defining slab-debris in D". In particular, the recent study of differential PKP phases ($PKP_{ab} - PKP_{df}$) strongly supports the detailed tomographic images beneath Central America [*Sun et al.*, 2007b]. Accurate differential times come from measuring the waveform correlation between PKP_{df} and PKP_{ab}, which is sensitive to the bottom 500 km of the mantle. PKP_{ab} paths from deep South America earthquakes cross the Core-Mantle-Boundary (CMB) beneath Central America, as indicated by the circles and crosses in Figure 3.3a. These differential times can be predicted amazingly well from the P model (Figure 3.3a) scaled from Grand's shear velocity tomographic model. Note the slow-to-fast structure beneath the Cocos Plate with a transition zone less than 300 km wide occurring just off the coast line. There is also a sharp drop in cross correlation coefficient between PKP_{df} and PKP_{ab} by over 30% along this same boundary indicative of ultralow velocity zones with small sharp features [*Luo et al.*, 2001].

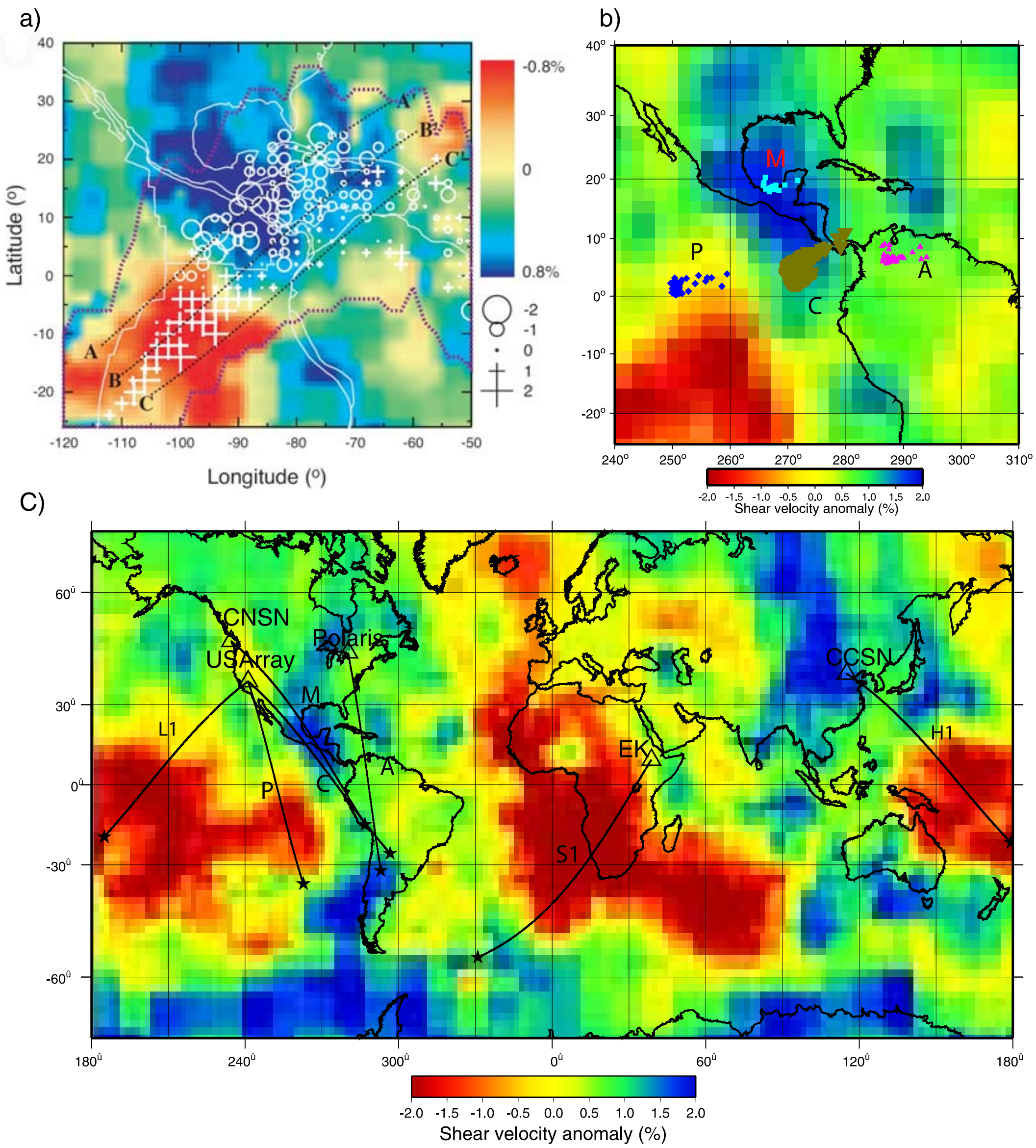

Figure 3.3: a) Observations of (PKPab-PKPdf) residuals sampling beneath Central America along with proposed D" P-wave model in the background [*Sun et al.*, 2007b]. b) contains a detailed map of Grand's tomographic image of Central America. The four subregions, P, A, C, and M are studied in detail where ScS bounce points are indicated in diamonds, triangles, inverted triangles, and squares, respectively. c) Display of a map of events (stars) along with path geometry to various arrays (open triangles) superimposed on the tomographic results [*Grand*, 2002]. L1 [*Lay et al.*, 2006], H1 [*He et al.*, 2006], and S1 [*Sun et al.*, 2007b] paths were used to quantify the D" structure beneath the slow velocity regions.

Combining the S and P wave results yields $R = dlnV_s/dlnV_p$ of about 1.9 which is too low to be produced by temperature alone [*Karato and Karki*, 2001]. The P and S velocity properties for the Superdomes proposed earlier by Masters et al. [2000] now appears to be well accepted, further confirming the case for changing chemistry.

While Figure 3.1b predicts weak Scd synthetics when the phase-boundary is near the CMB [*Sidorin et al.*, 1998], recent studies identify Scd clearly beneath warm regions as displayed along the lines in Figure 3.3c [*He et al.*, 2006; *Lay et al.*, 2006; *Sun et al.*, 2007a]. The latter study presents Scd data sampling beneath the middle of the South African Superdome which is modeled with a velocity jump of 4% occurring 80km above the CMB. In short, Sidorin's model based on relative travel times needs to be re-examined in terms of waveform modeling of record sections containing Scd detections at several ranges to establish a true triplication with both amplitude and timing information. This is particularly difficult since shallow upper mantle structure and mid-mantle slabs can alter pulse waveforms [*Song and Helmberger,* 2007]. It appears that stacking high density observations or detailed waveform modeling can help resolve these issues and provide a clearer picture of the PV to PPV phase boundary and possible change from PPV back to PV near the CMB [*Hernlund et al.,* 2005].

Here we update Sidorin's effort by developing a new phase boundary mapping tool. To achieve this, we will investigate data sampling beneath Central America, a region well studied, as discussed above.

3.3 Detailed Waveform Modeling for a Sample beneath Central America

We used shear wave records of the broadband array CDROM for two deep earthquakes in Northern Argentina on April 23, 2000 (Figure 3.4). The two events are roughly the same location. Horizontal component seismograms are deconvolved by instrument responses and bandpass filtered (0.01−1 Hz) before the rotation to SH component of displacement. The SH velocity seismograms are filtered with a bandpass filter (0.02–0.2 Hz). Data from the smaller of the two events is presented in Figure 3.5 along with synthetics generated for the

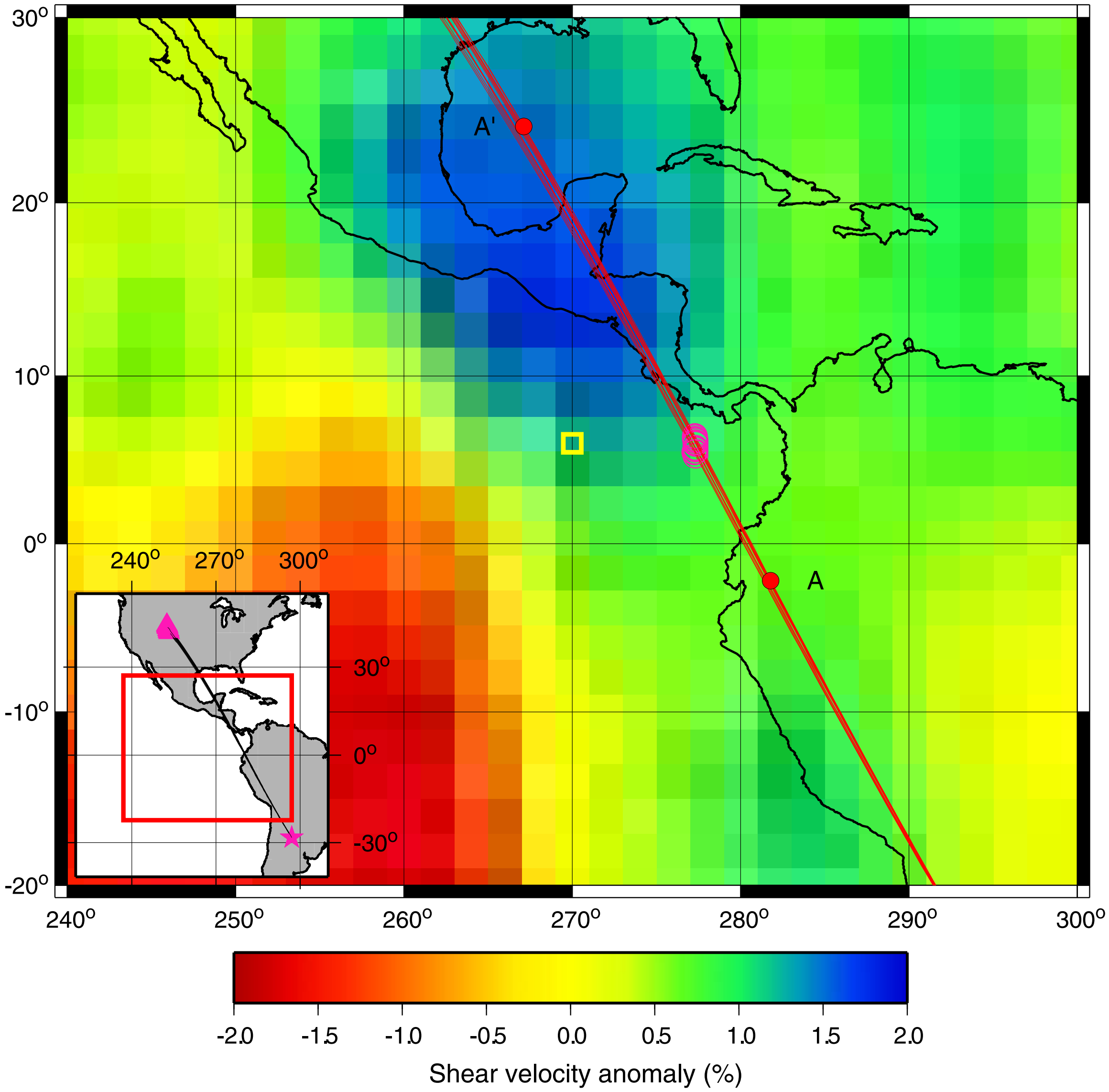

Figure 3.4: Geometry of the event and stations together with Grand's shear wave velocity anomaly in the lowermost 240 km of the mantle [*Grand*, 2002]. The event (star), receivers (triangles), and ray paths are shown in the inset. The pink open circles indicate the ScS bounce points beneath the western Cocos Plate for the ray paths (red lines). The yellow rectangle indicates the position where a large jump in D" discontinuity was detected by *Hutko et al*. [2005]. The D" region along corridor A'A is addressed.

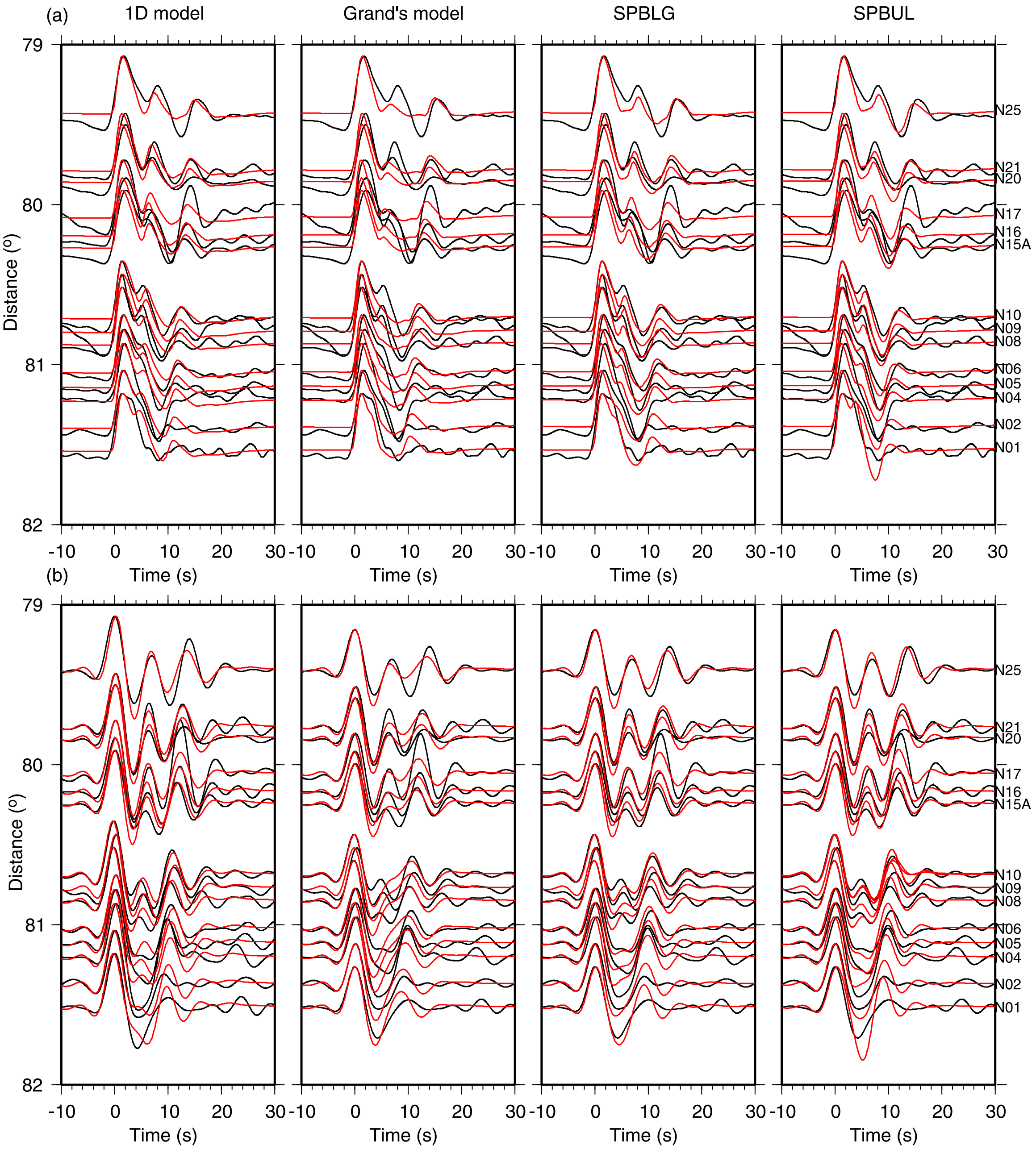

Figure 3.5: Comparison of synthetics (red) of (a) displacement and (b) velocity with data (black) for various models, starting from the left: 1D model, Grand’s tomographic model, SPBLG and SPBUL model. The synthetics have been aligned on the S-wave observations.

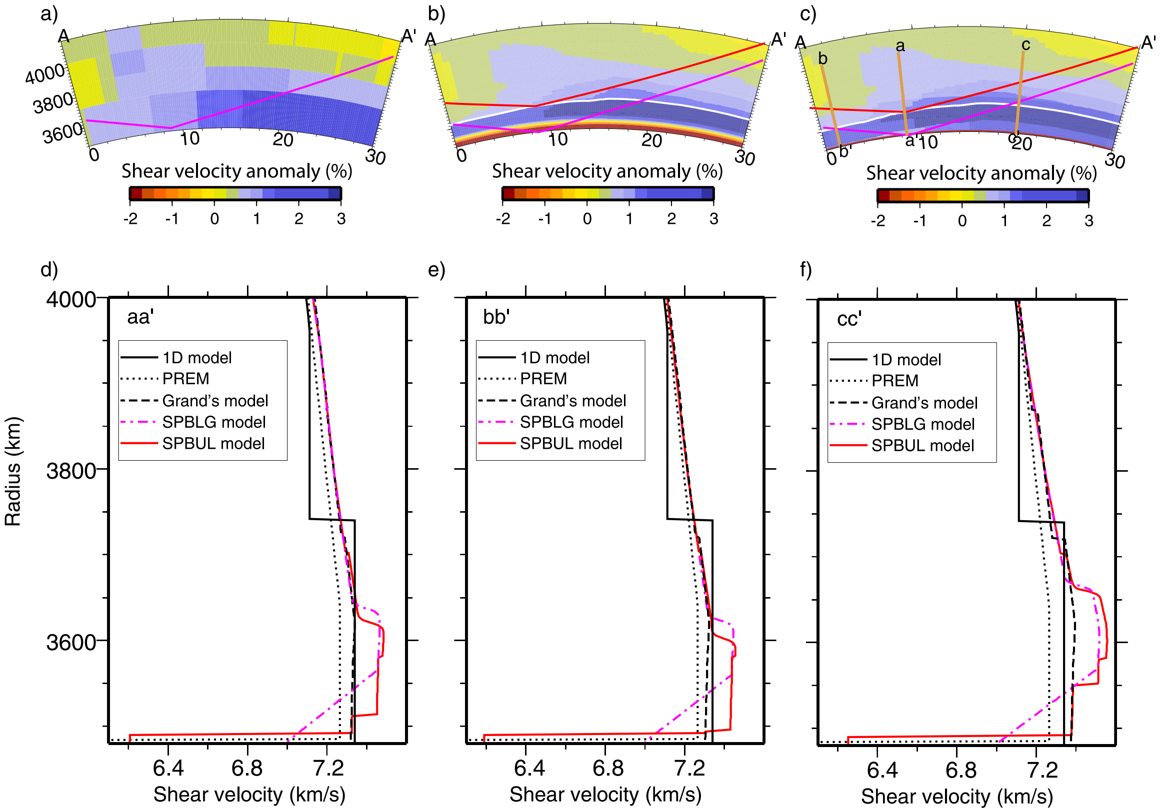

Figure 3.6: The shear wave velocity anomaly of 2D cross-section A'A in Figure 3.4 for different models. The models are a) Grand's tomographic model [*Grand*, 2002], b) SPBLG and c) SPBUL model. The reference 1D model is modified Grand's 1D model, which smoothes the ~1% Vs jump at the depth of ~250 km above the CMB at the origin model, essentially treating this velocity jump in the same manner as tomographic model. SPBLG model is constructed by adding a discontinuity and a compensating negative gradient at the base of mantle. The phase transition is characterized by $h_{ph} = 105$ km, $\gamma_{ph} = 6$ MPa/K. The SPBUL model contains an additional phase boundary, and modified velocities. The phase change boundary is shown by the white line. Grand's tomographic model is on a 2°×2° grid. The vertical resolution is around 200 km. Both SPBLN and SPBUL have 0.5°×0.5°×2 km resolution by interpolating the Grand's model above the phase change boundary. The velocity structures are much smoother in the later models than that in Grand's model. The bottom panels show the vertical profiles for the cross-section aa', bb', and cc'. Dotted lines indicate the PREM velocities. The dashed lines show the shear velocity with added tomographic velocity perturbations on PREM values. Red lines give the model by adding a discontinuity on an altered Grand's model and a LVZ above the CMB. SPBUL model also introduces a small negative jump (-1.7%) in the middle of D" to represent PPV changing back to PV in the thermal boundary layer.

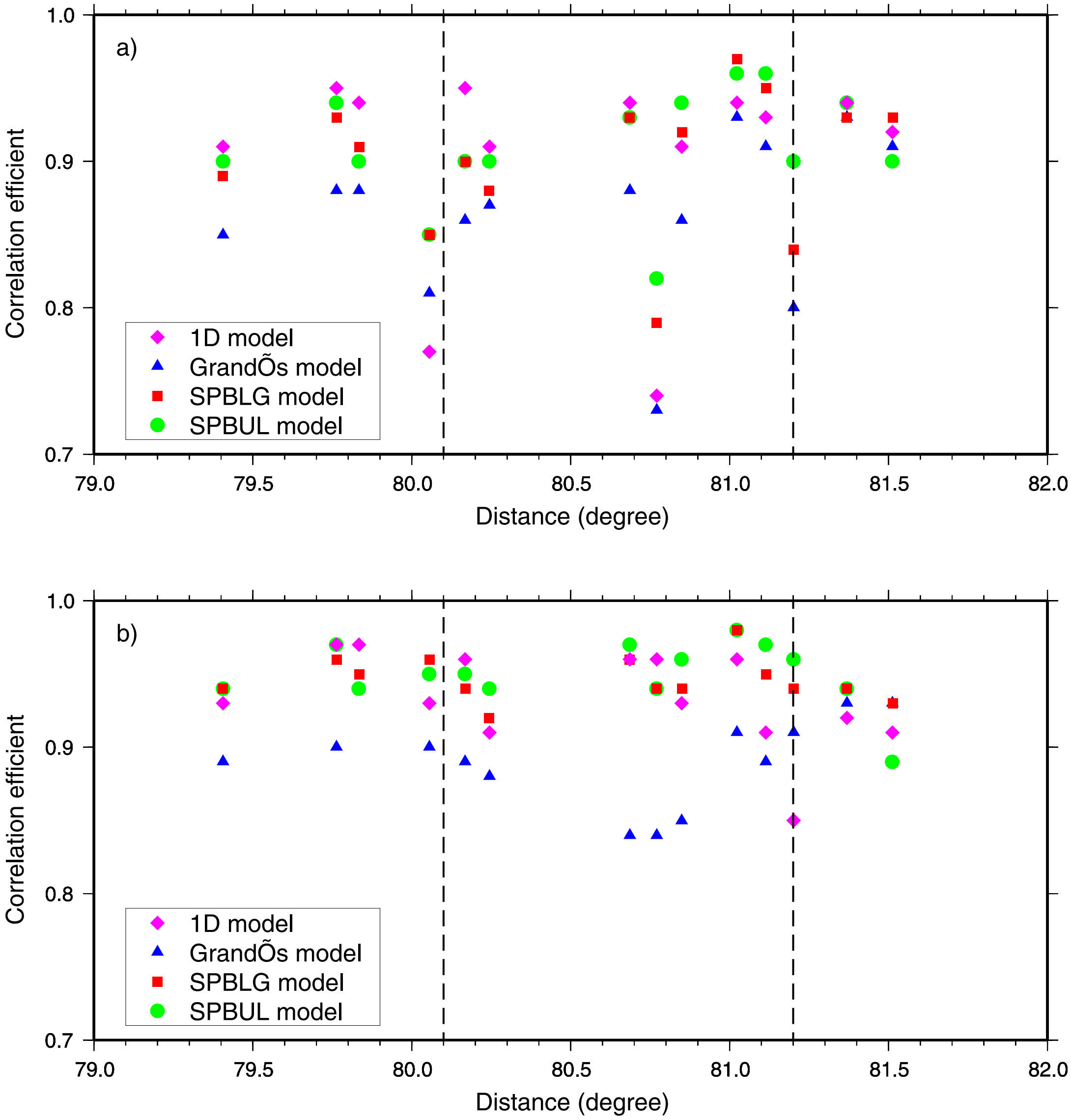

Figure 3.5: The results of cross-correlation between data and synthetics on both a) displacement and b) velocity. Purple diamonds show the 1D and blue triangles show the Grand's tomographic model results. Red squares are the results of Sidorin's type models. The dotted lines indicate where a possible ULVZ could exist. These synthetics are sampling the D" structure along the line of circles displayed in Figure 3.4.

three models. The records show strong and clear S_{cd} arrivals between S and ScS (Figure 3.5) at the epicentral distance (Δ) of 79° to 82°. Synthetics for 2D models were generated with the semi-analytic code WKM which is discussed in chapter 2. An advantage of this hybrid method is that it can be applied to existing tomographic models directly. In the 1D model, we fix the discontinuity at the depth of 264 km above the CMB and characterize the search as in Lay et al. [2004]. The velocity above the discontinuity is constant up to certain depth H and a velocity jump is specified across the discontinuity. The velocity jump and H are chosen by modeling the data. The preferred 1D model determined by grid-search in Figure 3.6 is similar to the model SLHA [*Lay and Helmberger*, 1983]. While one can obtain a good fit at the mid-distance, the timing is significantly off at the ends, the model is too early at the top traces and too late at the bottom. One can obviously fit any one record by adjusting the two parameters but we prefer a model that is more related to the tomography. However, the tomographic model can not predict Scd as displayed in Figure 3.5 without a discontinuity. Thus, it is necessary to impose a velocity discontinuity in the tomographic model for fitting the data as discussed above. In Figure 3.5, we found β = 1.7%, and h_{ph} = 105 km as the best fit following a grid search, model SPBLG. The h_{ph} is smaller than the previous suggested value h_{ph} = 200 km and β is also slightly larger than 1.5% in the former study [*Sidorin et al.*, 1999], which is caused by using an updated tomography model as applied locally. Deeply penetrating slabs may also contribute to the difference in h_{ph} by changing the chemistry. The velocity cross sections after the different mapping are displayed in Figure 3.6.

The high velocity structure on the upward path of S_{cd} decreases the separation between S_{cd}-S which mimics raising the discontinuity. The combined effects of both features produces a good fit to the data. However, these features tend to also shorten the separation of (ScS-S) which requires still greater velocity reductions approaching the CMB to maintain Grand's ScS travel times.

Model SPBUL fits the data somewhat better than SPBLG at ranges 80.1 to about 81.2 which can be seen in the correlations presented in Figure 3.7. This slight improvement is caused by enhancing and shifting the structure just about the discontinuity. With the mapping method here, model SPBUL captures the distinctive features of Scd of station

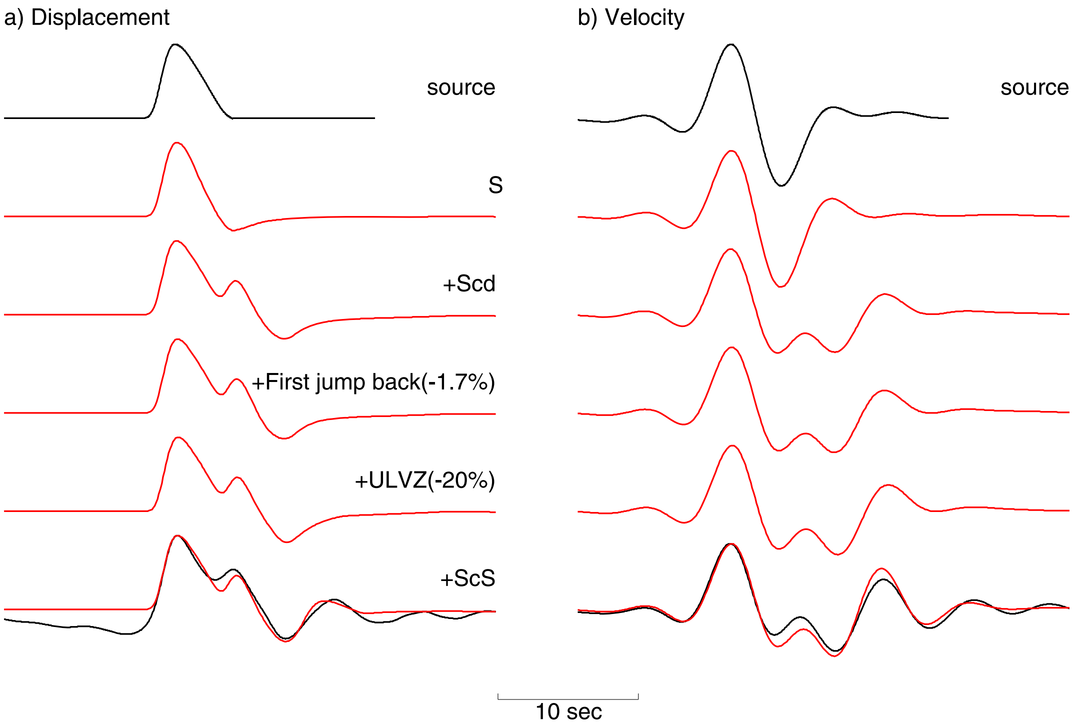

Figure 3.6: Construction of synthetics (Δ=80°) shows the sensitivity to various aspects of SPBUL velocity structure. The results for displacement are given on left with velocity on the right.

N02 and N04. But the strength of the ScS synthetic pulse at the two most distant stations (N01 and N02) is too strong, suggesting that the ultralow velocity zone must disappear or be a local feature beneath the southern stations only. But the velocity structure below the fastest structure is not well resolved with this dataset as shown in Figure 3.8. These synthetics were generated in parts where the model features have their field contributions isolated. Note the dominance of S_{cd} with its relative phase shift producing a sizable down swing in displacement. The S_{cd} is phase-shifted since it is part of a triplication and the presence of this negative pulse made it difficult to isolate the latter arrivals caused by double crossing and ULVZ. Thus, it will be quite difficult to detect a PPV to PV boundary in the presence of a complex S_{cd}, at least at this range of distances as suggested by Flores and Lay [2005].

While the range 79° to 81° is particularly effective for identifying S_{cd}, it is too restrictive to resolve deeper structure beneath the boundary except to delay ScS. Since both the S_{cd} and an ULVZ could enhance the strong negative pulse near 81°, we are faced with considerable uncertainty. However, either interpretation requires extreme lateral variation which a folded-slab could produce especially if it changes the local chemistry, i.e., thickens the phase-boundary transition zone [*Akber-Knutson et al.*, 2005]. There is also the issue of predicted instabilities in the thermal boundary layer at the edge of slab structure from dynamic modeling [*Tan et al.*, 2002]. Perhaps, the 2-dimensional array data from USArray will help resolve some of these issues.

A phase-induced boundary at reduced lower mantle temperatures induced by slab debris remains viable but probably requires other complications as suggested by Garnero and Lay [2003] to explain rapid changes in Scd strengths.

3.4 Calibration of Tomographic Models

In this section, we will follow the basic procedure suggested by Sidorin et al. [1999] except we will allow regional variation of γ, h_{ph} and β. Note that Sidorin et al. [1999] found solutions along a rectangular corridor of h_{ph}: γ space running from $2 < \gamma < 12$ MPa/K and $250 < h_{ph} < 150$ km. The best fitting least-squares solution is near $h_{ph} = 200$ km and $\gamma = 6$ MPa/K for a uniform global model but γ as high as 12 MPa/K were accepted. Here, we assume that the velocity perturbation of δV_S in the D" layer is indicative of local dynamics and constitutive state-properties. Thus, each sample of Scd in Figure 3.3b (denoted by P, A, M, C) is assumed to have unique properties in terms of their δV_S averaged over a 2°×2° grid, and all other samples with the same δV_S will affect the phase boundary the same. To establish that functionality, we determine the best synthetic waveform fits to observe record sections to set $h_{ph}(\delta V_S)$ for a number of γ. By matching both arrival times and amplitudes, we were forced to vary β or $\beta(\delta V_S)$. The results are presented in Figure 3.9 and will be followed by zone-by-zone comparisons of data with synthetics. To investigate the effects of different Clapeyron slopes on our phase boundary mapping, we tried 4 values of Clapeyron slope (γ = 3, 6, 9, 12 MPa/K). For each γ, we repeat the calibration process to find the $h_{ph}(\delta Vs)$, which matches the local triplication data in each zone. The h_{ph} becomes small when increasing γ for zone M and C. Both Zone M and C have relatively large positive velocity anomaly ($\delta Vs > 0$) and negative non-adiabatic temperature perturbation ($\Delta T < 0$). With negative ΔT in Equation (3.2), the h_{ph} will decrease by increasing γ to make constant (h), which is required to fit the waveform data. If ΔT is a small perturbation, the contribution from ΔT in Equation (3.2) is close to 0 and the change of h_{ph} is subtle for zone P and A. The same velocity jump $\beta(\delta Vs)$ are used for different γ to fit the amplitudes of the data.

In each zone, β and h_{ph} are allowed to vary such that the predicted synthetic best matches the observed waveforms. We allow β to vary from 1.0 to 4.5% and h_{ph} from 50 to 300 km. Each combination is tested applying a grid-search where the tomographic map (Figure 3.1a) is used as a reference model. The preferred combinations are given in Figure 3.9 where h_{ph} ranges from 100 to 240 km and β from 3.5 to 1.7% for all four different γ. The variable (δV_s) is defined relative to the tomographic model. The 1D velocity-depth plot for the average ScS in each sample is given in the lower panel of Figure 3.9 indicating the relatively large variation as a function of δV_S. The large low velocity zone approaching the CMB is mostly an artifact forced by fitting the ScS-S predictions from Grand's model. However, adding a PPV to PV reduces this feature but is difficult to distinguish at these ranges [*Flores and Lay*, 2005; *Sun et al.*, 2006]. Thus, we concentrate on the upper PV to PPV phase transition.

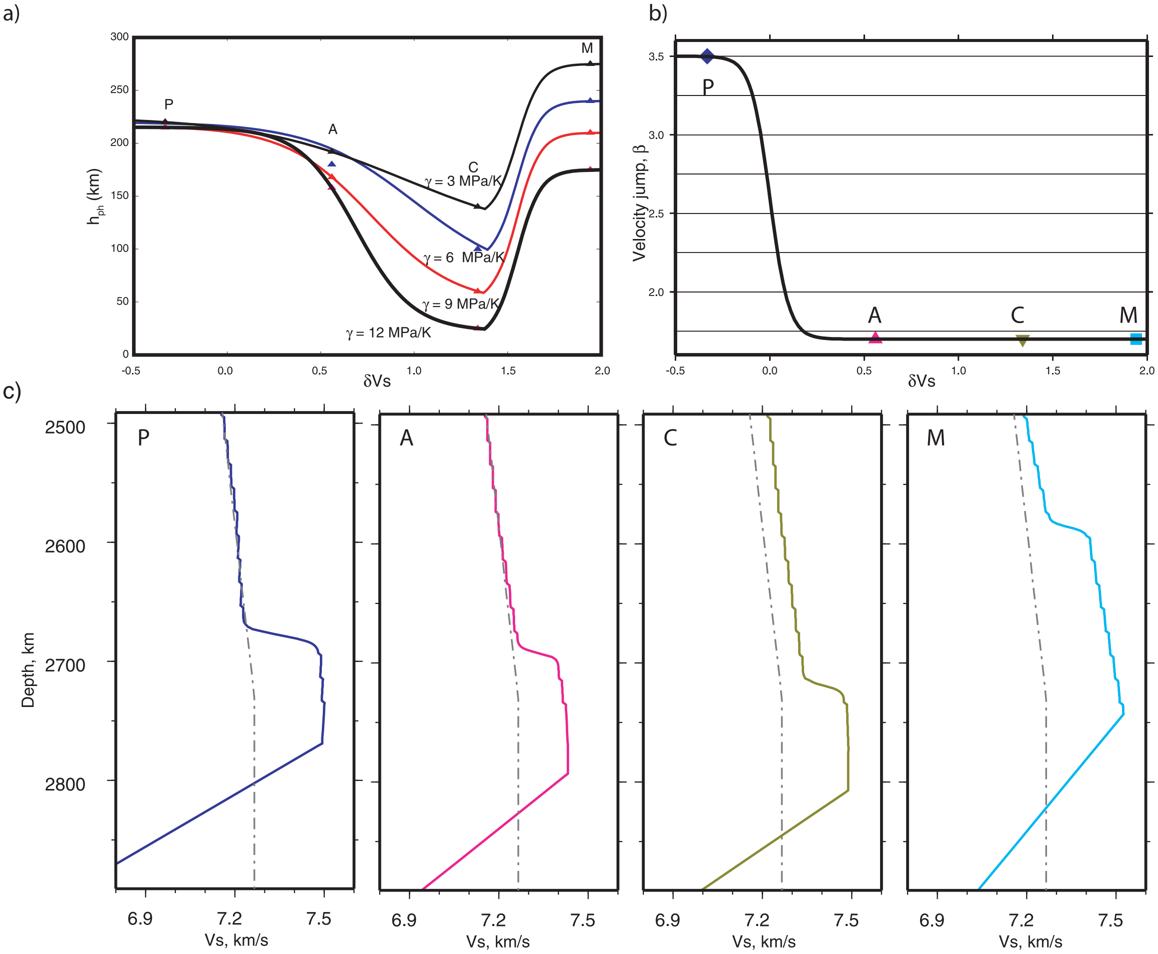

Figure 3.7: Results from various subregions with $h(\delta Vs)$ in (a) for several γ and $\beta(\delta Vs)$ in (b) which is the same for all γ. Velocity profiles for the midpoint of each subregion is given in (c) along with PREM as a reference. The γ is equal to 6 MPa/K in the mapping. Note that the ray paths for Scd are traveling horizontally at this point and are strongly influenced by neighboring structure as can be seen in Figure 3.3.

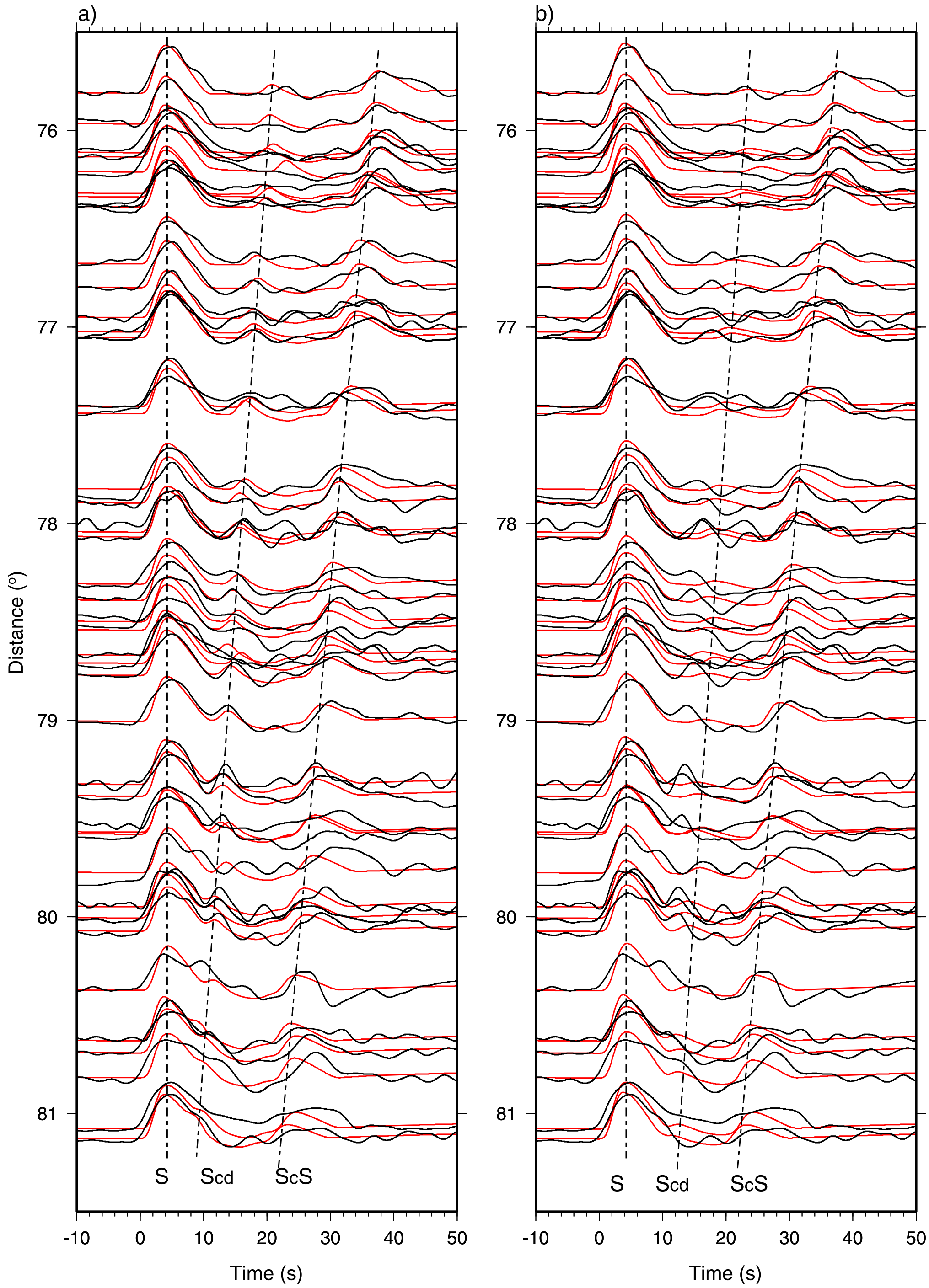

Figure 3.8: Display of synthetics (red traces) matching the recorded waveforms from area P (black traces), which were recorded by the USArray of a shallow transform event (20050710). The model in a) has h_{ph} = 220 km and β= 3.5%. b) model has h_{ph} = 200 km and β= 1.5%. γ in both models are 6 MPa/K. Dotted lines are added to indicate the three arrivals: S, Scd, and ScS.

3.4.1 Zone P

As discussed earlier, there are very few samples of Scd beneath the Central Pacific because of the limitation imposed by the use of deep events and station-source geometry. However, it appears that USArray and other large arrays will allow sufficient data to identify Scd even from shallow events, Figure 3.10. This is a shallow transform event occurring on the Western Chile Rise (Figure 3.3c). We have plotted the data (SH-component only) over the triplication distances expected. Since shallow strike-slip events generally produce two pulses of the same sign within a few seconds (S + sS), they merge together to produce one simple pulse which is labeled S in the figure and idealized to the first synthetic pulse. There is some variation of the observed S-pulse across the array which could be caused by shallow receiver structure [*Song and Helmberger*, 2007] or generated in the source region. However, both Scd and ScS appear to be recognizable. The tomographic model predicts the separation of (ScS-S) very well which can be expected from the detailed samplings of transform fault events by *Grand* [1994]. These 2D synthetics were generated with the WKM routine [*Ni et al.*, 2000] along 2D sections through the 3D model. Note there are some variations along the record section caused by small changes in azimuth along the various paths. The reference height and velocity jump for this match is h_{ph} = 220 km, β = 3.5%, where δVs = -0.5% and assumed γ = 6 MPa/K. Synthetics generated by other γ-models (Figure 3.9a) produce nearly the same results. Figure 3.10b contains predictions from the original Sidorin et al. [1999] mapping but with an updated tomographic map [*Personal communication with S. Grand*], and where β = 1.7%. Obviously, the Scd is very small and late in these predicted synthetics.

Because Scd is small relative to S and ScS in the data, it proves difficult to identify and measure accurately. At distances 76° to 78°, it is generally isolated but weak. At distance from 79° to 81°, it is generally stronger but can be contaminated by complex S. Even though our preferred model has about the correct timing on average, there are obvious rapid fluctuations in Scd observations both in strength and timing, i.e., near 76.2° and 78.6°. The synthetics show some of this scatter which appears to be associated with small changes in azimuth (Figure 3.3) as embedded in the tomography model. Allowing w_{ph} to vary could also affect such changes as indicated in Figure 3.11. Generally, Scd becomes smaller with

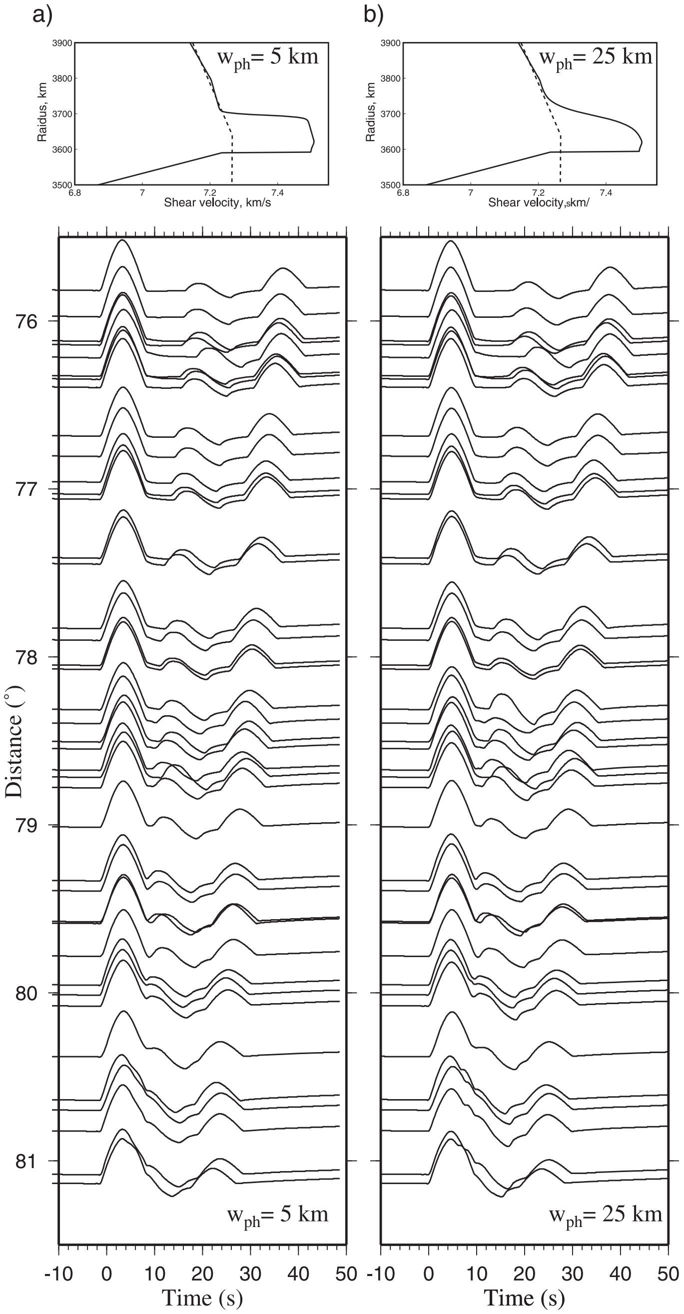

Figure 3.9: Comparison of a sensitivity test involving changes in w_{ph} from a) 5 km to b) 25 km. The synthetics are calculated for zone P with h_{ph} = 220 km and β= 3.5%. The top panel shows the 1D vertical profiles (solid lines) in the middle of zone P for different w_{ph} along with PREM model (dash lines).

increasing w_{ph} at these periods but variation in the tomography again causes fluctuations. Also, note that with w_{ph} = 25 km, the effective transition occurs over 100 km (Figure 3.11b) because of the functional form in Equation (3.1). This comparison of synthetics indicates that the $\mathrm{w_{ph}}$ parameter proves difficult to determine at this distance range. Thus for our purposes, we fix w_{ph} = 5 km. Much stronger effects are observed in the “C” samples as discussed later. The large β jump was required to generate a significant Scd pulse because the lower mantle velocity gradient is so low, Figure 3.9c, compared to fast regions [*Sidorin et al.*, 1998].

The phase ScS is usually less well defined at this range, where ray paths begin to sample the complexity of D". In the previous paragraph of detailed modeling, we try to model whole records by measuring a misfit coefficient based on cross-correlations (CC) both in displacement and velocity. Generally, simply overlying the observations with synthetics provides a very effective means of judging the goodness of fit. Here, we used this CC measure of fit but removed ScS by cutting the data and synthetics by 5s before ScS. A plot of misfit errors for a grid-search over β and h_{ph} is displayed in Figure 3.12 where we have included predictions from the *Sidorin et al.* [1999] model. By examining the record sections, one can easily pick out the better model. Although we have conducted such misfit calculations for all the data, we will simply display the best-fitting synthetics in the following analysis assuming γ = 6 MPa/K.

3.4.2 Zone A

The paths from these observations (Figure 3.13) sample a region nearest to PREM in that both S and P data (Figure 3.3) are relatively normal. The h_{ph} is 180 km as displayed in Figure 3.9a when γ = 6 MPa/K. However, there is considerable variation in ScS–S times at ranges 77° to 78°. This feature is modeled quite well by Grand’s tomographic model where the mid-mantle slab plays a strong role. We have plotted the comparison between data and synthetics in two ways, one aligned on data S arrival (Figure 3.13a) and one aligned on predictions from the IASP91 reference model (Figure 3.13b), which displays obvious variation in S travel times. Note that now ScS plots more on a line

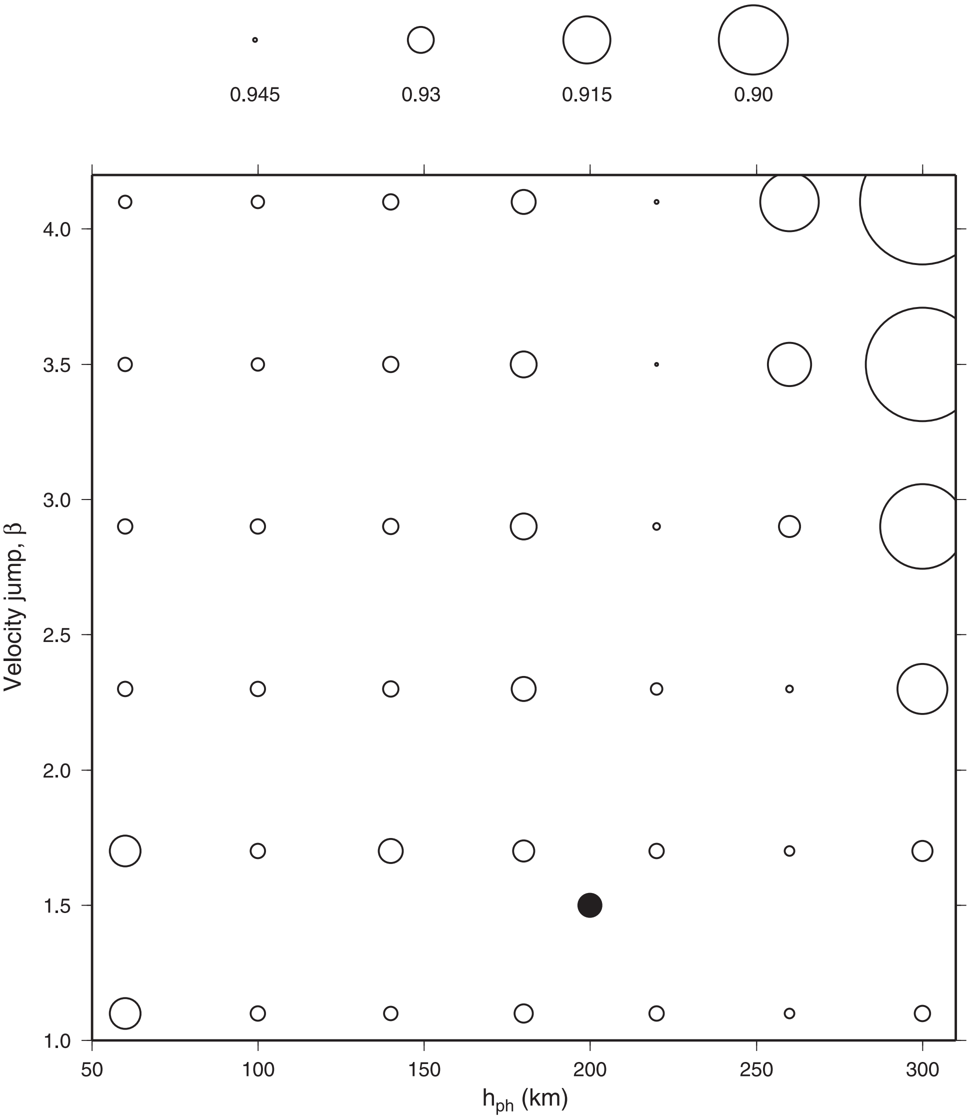

Figure 3.10: Display of misfit errors in modeling the data for area P with γ = 6 MPa/K.where the preferred parameter search yields β = 3.5% with h_{ph} = 220 km. The black dot is the solution predicted by Figure 1b using the mapping proposed by *Sidorin et al.* [1999]. The circles denote the error measure defined by (1 - CC), where CC is the cross-correlation coefficient over the S and Scd wavetrain. The smaller circle means the larger value of CC.

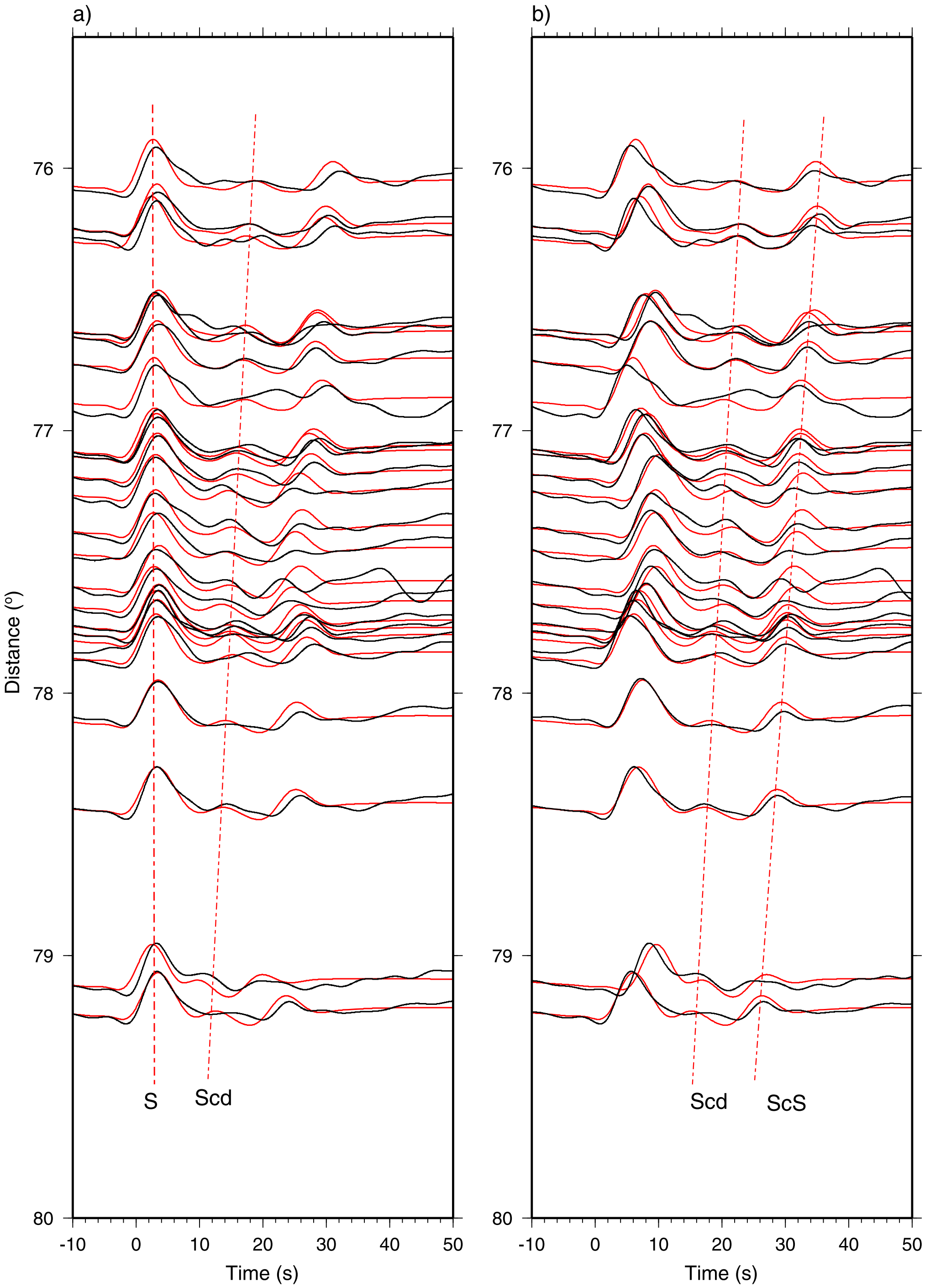

Figure 3.11: Display of best-fitting synthetics (red traces) for record sections sampling area A recorded by the POLARIS array of a deep South American event (20060917). The model has h_{ph} = 180 km and β= 1.7%. The displacement profiles are aligned on the arrival of S in a) and the predicted arrival of S for the IASP91 model in b). Note the remarkable predictions of S arrival times from the tomographic model.

as well as Scd. Features such as the strong variations in S are becoming more recognized with the advance of more arrays and makes the Scd mapping even more challenging.

3.4.3 Zone M

This sample (Figure 3.14) was obtained mostly from the Canadian National Seismic Network, Figure 3.3c. It contains the fastest D" velocity regions comparable to those found beneath Central Asia [*Wysession et al.*, 1998]. The tomographic results do not predict the sScS-sS differential times as well as other samples, suggesting that the D" structure needs to be faster. However, the Scd phase is quite clear and easily modeled yielding an $h_{ph} = 240$ km. The direct S phase was weak (nodal) which is why we have displayed the sS profile of data. The depth effect helps to separate (sScd – sS) and aids in identifying and characterizing the strength of Scd. We have calculated synthetics with parameters from the zone “C” (Figure 3.9) to emphasize the difference in Scd sampling. Although not displayed, predictions from the Sidorin et al. [1999] model do quite well for this section since he assumed a similar $\beta = 1.5\%$. Thus, our new model will predict results quite similar to his in fast regions.

3.4.4 Zone C

This sample is in a region where many detailed studies have been conducted, where rapid changes have been reported indicating some strong and some very weak Scd observations [*Garnero and Lay*, 2003]. Migration of the array data suggests complex features with interbedded layers of velocities [*Thomas et al.*, 2004]. Some of this variation can be seen in our sample C as recorded by USArray but reasonably modeled with $h_{ph} =$ 100 km as displayed in Figure 3.15a,b for ranges less than about 78.5°. We have included two sensitivity displays indicating the effects of changing $\beta = 3.5\%$ (Figure 3.15c) and of changing the h_{ph} to that used in zone P (220 km) (Figure 3.15d). These two results do not fit the data as well and indicate relatively delayed Scd relative to S which is distinctly different than that predicted by the Sidorin’s model, as discussed in the next section. Beyond about 78°, the Scd ray paths sample the edge of the fast blue zone as displayed in Figure 3.3b and

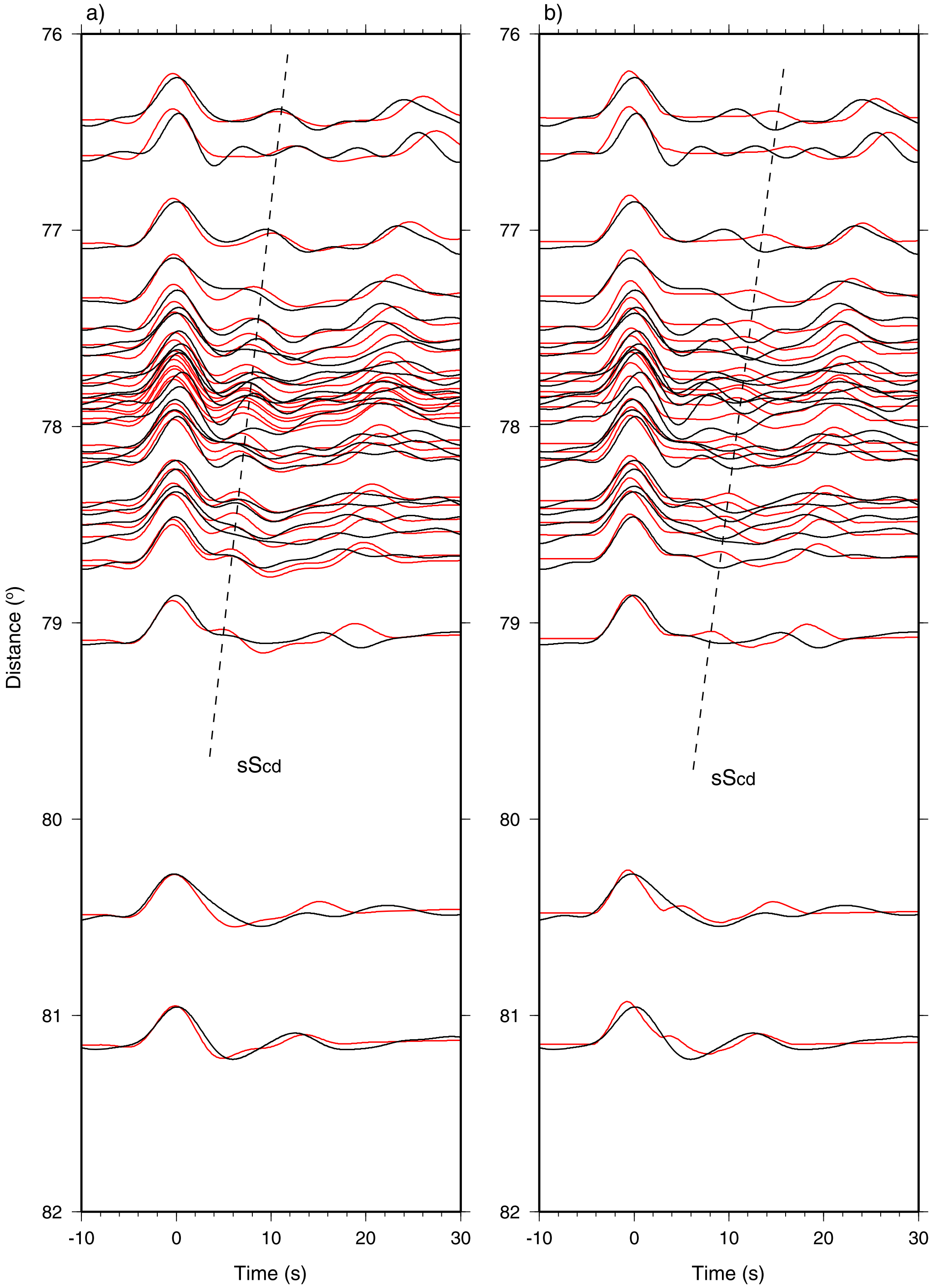

Figure 3.12: Comparison of synthetics (red traces) with observations (black traces) from the Western Canadian stations of a Southern American event (20050726). For model a), h_{ph} = 240 km and β = 1.7%. The synthetics in b) are produced by a model with h_{ph} = 100 km and β = 1.7% to indicates sensitivity relative to the model for zone C.

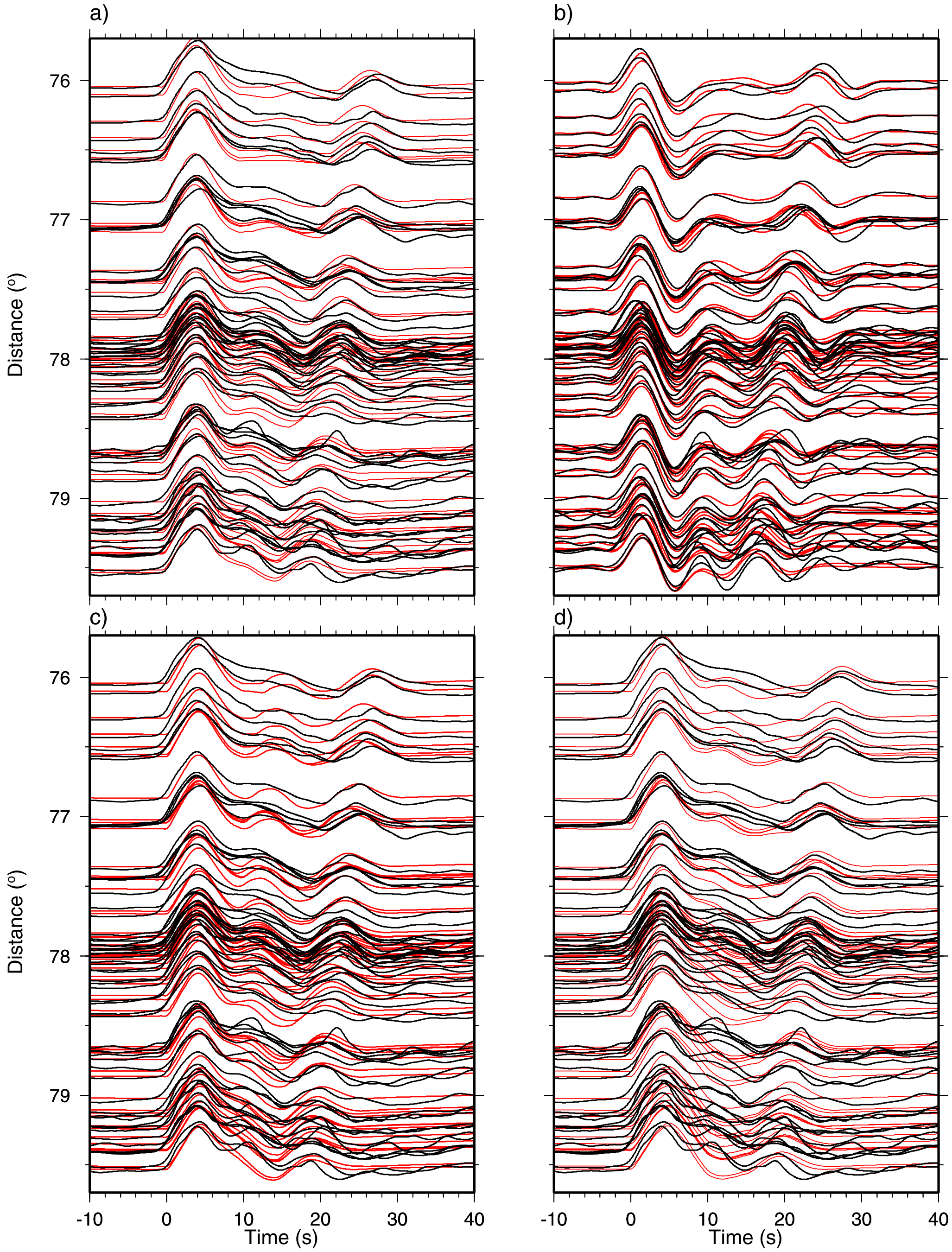

Figure 3.13: Comparison of synthetics (red traces) and observations (black traces) sampling subregion C of a deep South American event (20061113). a) shows the displacement profiles for a model with h_{ph} = 100 km and β = 1.7%. The velocity profiles for the same model are shown in b). c) displays results from a model defined by h_{ph} = 100 km and β =3.5%, whereas d) assumes a model with h_{ph} = 220 km and β = 1.7%. Note that fits in b) are relatively good at distances less than 78.5 °.

greatly complicate the waveforms. Some of this complexity is addressed in Sun et al. [2006] and Helmberger et al. [2005], where both WKM and finite-difference modeling was discussed. This laterally varying D" region sampling the same area is also discussed in Thorne et al. [2007] where some 2D structures suggest double Scd arrivals. We will address some of these issues in the next section by including these very late Scd arrivals which are sampling the edge of the fast blue zone.

3.5 Mapping, Predicting, and Refining

In this section, we will apply the parameters determined in the previous section in generating a new hybrid model. The model is still based on Grand's tomographic images and the relationship given in Equation (3.2). However, uniform h_{ph} is now replaced by $h_{ph}(\delta V_s)$, which is a function of the local shear velocity perturbation. We assume that the bottom 240 km of Grand's model or D" can be used to estimate regional differences. Grand's present model is presented in 2°×2° grids and contains a small velocity jump at 240 km above the CMB in the reference 1D model. This feature is smoothed-out and a large number of layers and elements applied as in Sidorin et al. [1999]. We then average the velocity perturbations in a circular cylinder over the depth of 240 km with a radius of 2° to establish δVs. This δVs is then used to fix h_{ph} assuming the curve in Figure 3.9a. The map of the phase height in Figure 3.16a is constructed in this manner assuming $\gamma = 6$ MPa/K. Note that even though the slowest and fastest regions have about the same h_{ph} their actual phase-height is strongly modified by the tomographic model (roughly 50 km to 300 km) because of the temperature effect implied by the tomographic model. The 3D velocity model is then generated by adding the variation in β in Equation (3.1) as modified to agree regionally with Figure 3.9b. Cross-sections along a radial cut (AA') and along constant azimuth (BB') are displayed in Figure 3.16b and c. The yellow halo-like structure in Figure 3.16a appearing around the raised plateau is caused by point C in Figure 3.9a and predicts the strong drop in elevation at the edges of the original supposed buckled-slab. Ray paths along two azimuths, one sampling the edge along the yellow trough (CC', Figure 3.16d) and one sampling the fast blue zone essentially along section DD' (Figure 3.16e) have been included in 2D tomographic images. Obviously, we expect to see considerable complexity

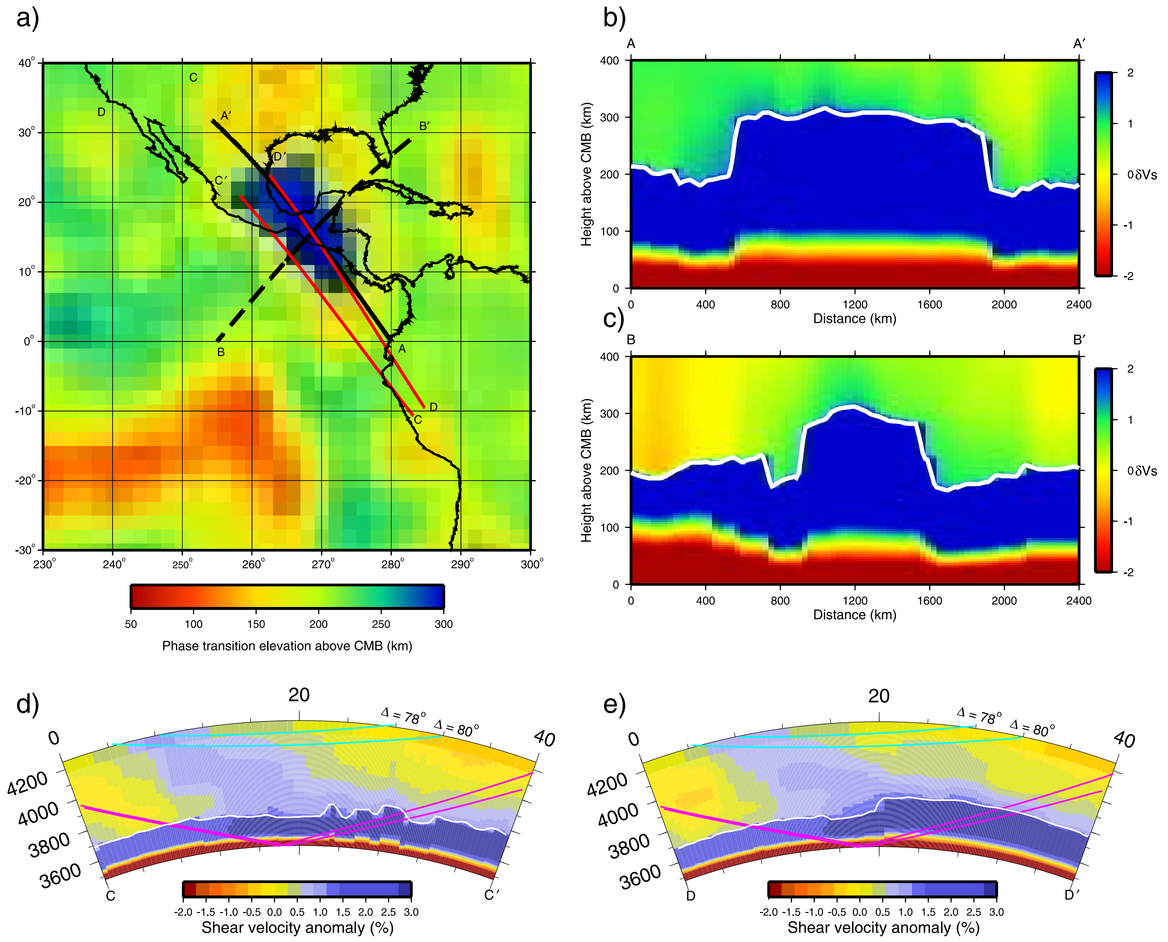

Figure 3.14: Detailed display of phase boundary topography; a) displays the phase boundary variation beneath Central America. Velocity cross sections along profiles AA′ and BB′ sampling the raised structure are given in b) and c). The phase boundary is indicated as white lines. d) and e) show the cross-section along path CC′ and DD′ from an event in South America. Ray paths are included for S (blue) and ScS (red).

bracketed between these two azimuths, especially along CC'. We have included some example ray paths displaying the structure sampled by USArray in Figure 3.16d and e. The sampling of the phase boundary (Scd) becomes very complex.

Figure 3.17 displays some of these features where the ScS bounce points are indicated for two “fan shots” with one crossing the blue structure (red arc) and one just south of the structure in black. We generated 2D synthetics (Figure 3.17b) at a constant distance of 79.5° for event A assuming two depths (150 km and 600 km). These synthetics are aligned on PREM prediction. Note that Scd is particularly late at azimuths less than 280° and shifts rapidly forward near 290° and again between 315° and 330°. The Scd timing changes by over 12 s and its amplitude changes by about a factor of 3 along with significant wave shape distortions caused by in-plane multi-pathing. Near 320°, the Scd phase shifts quite close to S for the deep event which could easily be enclosed within the S-phase, thus making it disappear abruptly.

These synthetics become even more complicated when we include azimuthal multi-pathing as displayed in Figure 3.17c. To emphasize the variable nature of the 3D synthetics, we have plotted each trace aligned relative to PREM prediction. Thus, paths with azimuth greater than about 335° sample the fast velocities beneath the Midwest and eastern seaboard producing earlier arrivals than PREM prediction while those to the west are about 6 s late. This difference in travel times is caused by the rapid change in upper mantle structure when crossing the Rocky Mountain Front and is well known [*Helmberger et al.*, 1985].

The 3D synthetics (Figure 3.17c) were generated from neighboring 2D sections sampling the Fresnel zone by applying diffraction operators [*Helmberger and Ni*, 2005a]. Rapid travel time changes near the fastest geometric ray can cause the pulses to spread out (multipath), i.e., near 275° or spike-up as at 340°. These features are essentially controlled by the travel-time curvature as a function of azimuth. It can affect all phases but appears to be particularly strong for Scd. This feature could be the reason for the apparent unstable nature of Scd detection [*Garnero and Lay*, 2003]. Both the 2D and 3D synthetics show a jump near 320° for ranges near 81°. This feature is more subdued in the 79° fan-section since the fast structure is slightly removed from the boundary (black arc in Figure 3.17a).

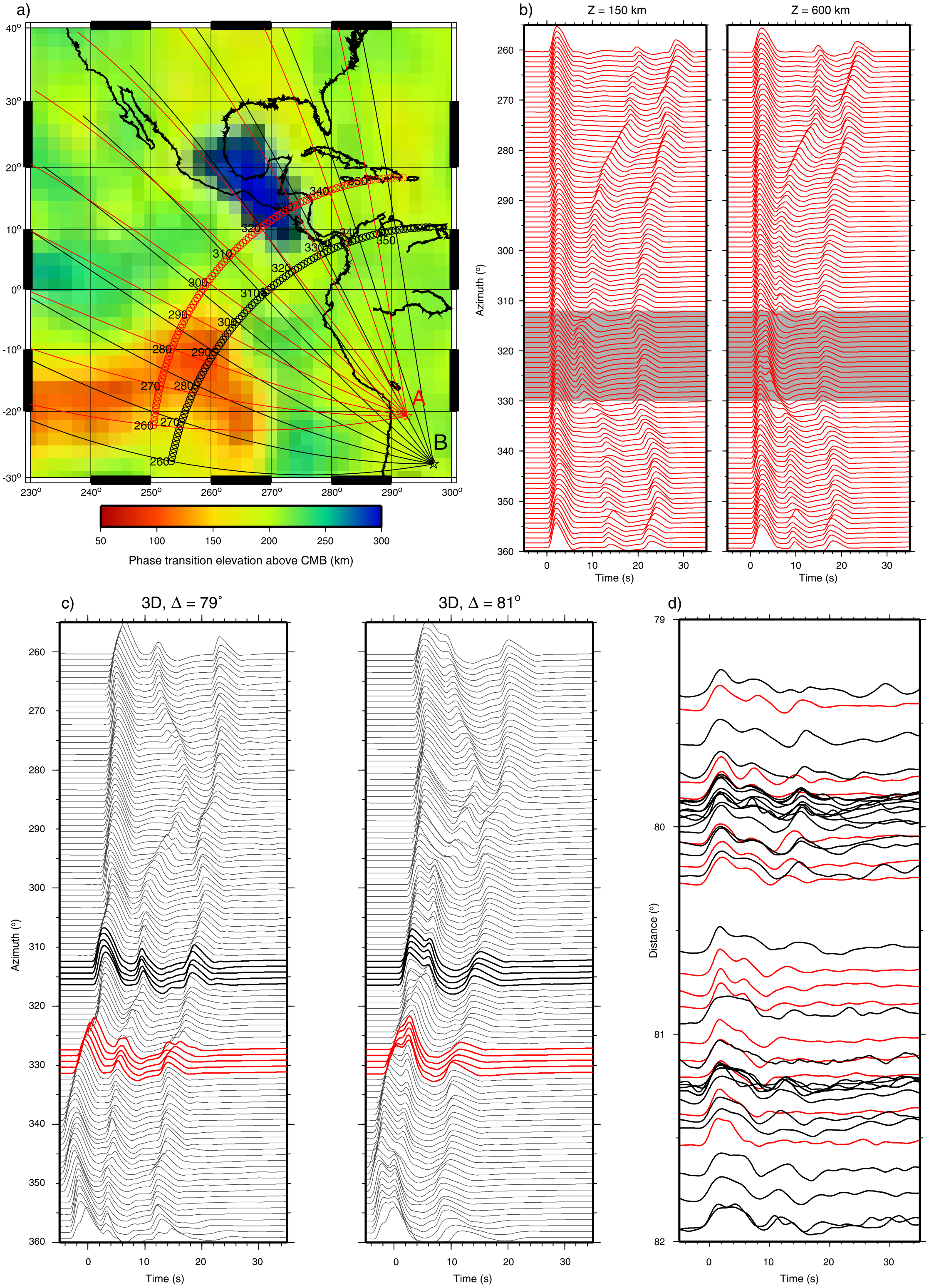
a)
A
B
Phase transition elevation above CMB (km)
50
100
150
200
250
300
b)
Z = 150 km
Z = 600 km
Azimuth (°)
Time (s)
c)
3D, Δ = 79°
3D, Δ = 81°
Azimuth (°)
Time (s)
d)
Distance (°)
79
80
81
82
Time (s)

Some of the predicted changes can be tested against existing data with some success, as displayed in Figure 3.17d. The data contains paths to California (in black) and to Colorado (in red). Note that Scd is stronger and delayed in the California stations at ranges greater than 80.5° and nearly the same at shorter distance. The synthetics in Figure 3.17c display a similar pattern as outlined in red and black zones. However, the differences predicted by the model are not severe enough, which requires some added refinement by lowering the trough along the fast region or adding a ULVZ at the CMB. This zone at the edge of the blue structure will be well-sampled by USArray as it develops and the details of this interesting structure can be improved. A sample is displayed in Figure 3.18a. Note the abrupt change in character in the gray zones where the ray paths encounter the sharp jump in phase-height. Beyond this range, the Scd becomes difficult to identify and the ScS phase becomes complicated. The ScS phase should become asymptotic to S in travel time at the larger ranges assuming a PREM model; however, ScS becomes weak and delayed for many samples. The synthetic predictions are given in Figure 3.18b and display a similar disruption but shifted slightly to shorter distances. Shifts of this magnitude are common when attempting to model differential phases assuming enhanced tomographic images [*Helmberger and Ni*, 2005b].

Figure 3.15: Simulations of seismic sections sampling the complex geometry of the phase boundary variation. a) displays the phase boundary variation beneath Central America. The red circles are ScS bounce points on the CMB for a “fan shot” for an event A in South America (red star) at distance of 79.5º. The black circles indicate ScS bounce points for a “fan” shot for event B at a distance of 79º assuming a source depth of 600 km. b) displays 2D synthetics generated for event A at two different depths, 150 km and 600 km. The shaded zone indicates the sampling of the region of high phase boundary elevation (blue zone in (a)). Records are aligned on the S-phase. c) shows the 3D synthetics for event B at distance 79° and 81°, which align on IASP91 travel time predictions. The dark black traces correspond to azimuths towards California (TriNet) and red traces relative to Colorado Stations (CDROM). d) Record sections for an event (20000423) with the same location of event B in a). The black traces are recorded by TRInet which are at smaller azimuth and relate to the dark black traces in c). The red traces were recorded by CDROM array at large azimuth and relate to the red traces in c).

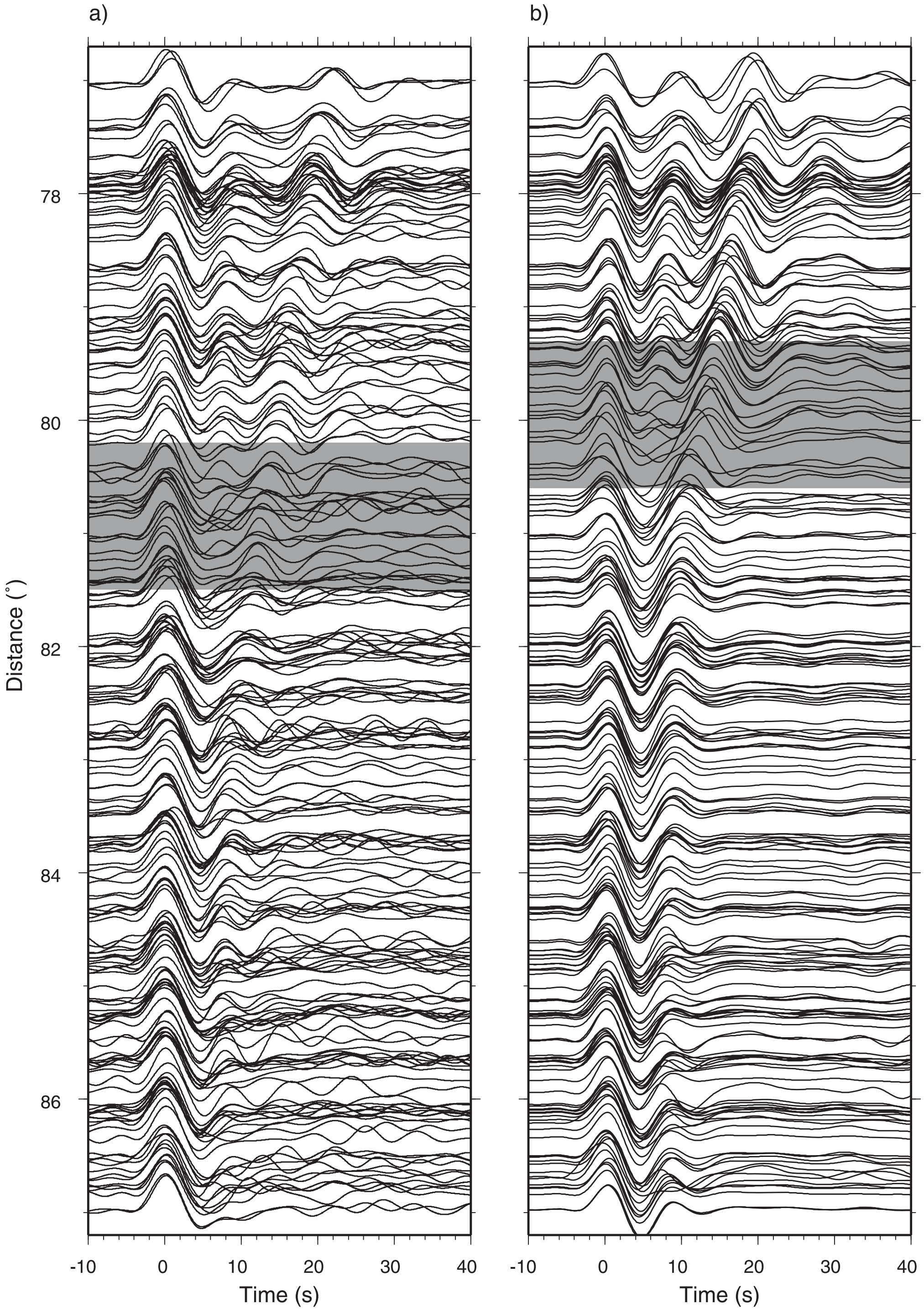

Figure 3.16: Comparison between a) data and b) synthetics in velocity for event 20061113. The regions with rapid variation of Scd are marked with shaded area.

We present (ScS-S) predictions from our model in Figure 3.19a where we have included a large number of data samples measured from the recent USArray data. The white symbols are differential times from the (ScS-S) waveforms presented earlier in Figure 3.18a. The differential values are small and slightly negative at ranges 75° to about 84° and positive thereafter. Some large delays occur beyond 85°. Note that these values occur for bounce points slightly under the elevated phase boundary as displayed in Figure 3.19b. These large delays can be explained by adding a ULVZ layer (20 km thick with a shear velocity drop of 30%). However, most of the delays fall along the model predictions. The other symbols are from events along the same corridor but tend to be negative indicating that ScS is early, probably caused by the high velocity PPV layer.

Several researchers have reported on ULVZs near about N7.5°W90°, i.e., Revenaugh and Meyer [1997], and more recently Sun et al. [2007a]. The latter study uses the cross-correlation of PKPab to PKPdf to detect rapid changes in velocity with scale lengths similar to those in Figure 3.19b. Low values of cross-correlations have been modeled by Luo et al. [2001] with small pockets of ULVZs. It appears that another line of ULVZs exists along the eastern boundary of the elevated phase-boundary although we await USArray for a detailed ScS-S sample of this edge. Lastly, note that the large offset in Scd travel times reported by Hutko et al. [2006] occurs along the southwest corner of our structure in good agreement with their observation.

3.6 A Global Prediction of the New Mapping

We have generated a strategy for mapping the tomography model to phase boundary. Because the mapping is based on limited samples beneath Central America, we want to understand whether this mapping is accepted for global phase boundary. How well this model predicts synthetics is presently being addressed but we expect it to work best when sampling away from the edges of the slab debris of the lowermost mantle. An example is given in Figure 3.20. This particular Hindu-Kush event is at a depth of 240 km and provides the extra set of observations (sS) which has the advantage of separating receiver effects from the target phase [*Lay*, 1986]. The new mapping produces the S_{cd} phase that can be identified in many of the traces. Note the observed ScS phase (Figure 3.20c),

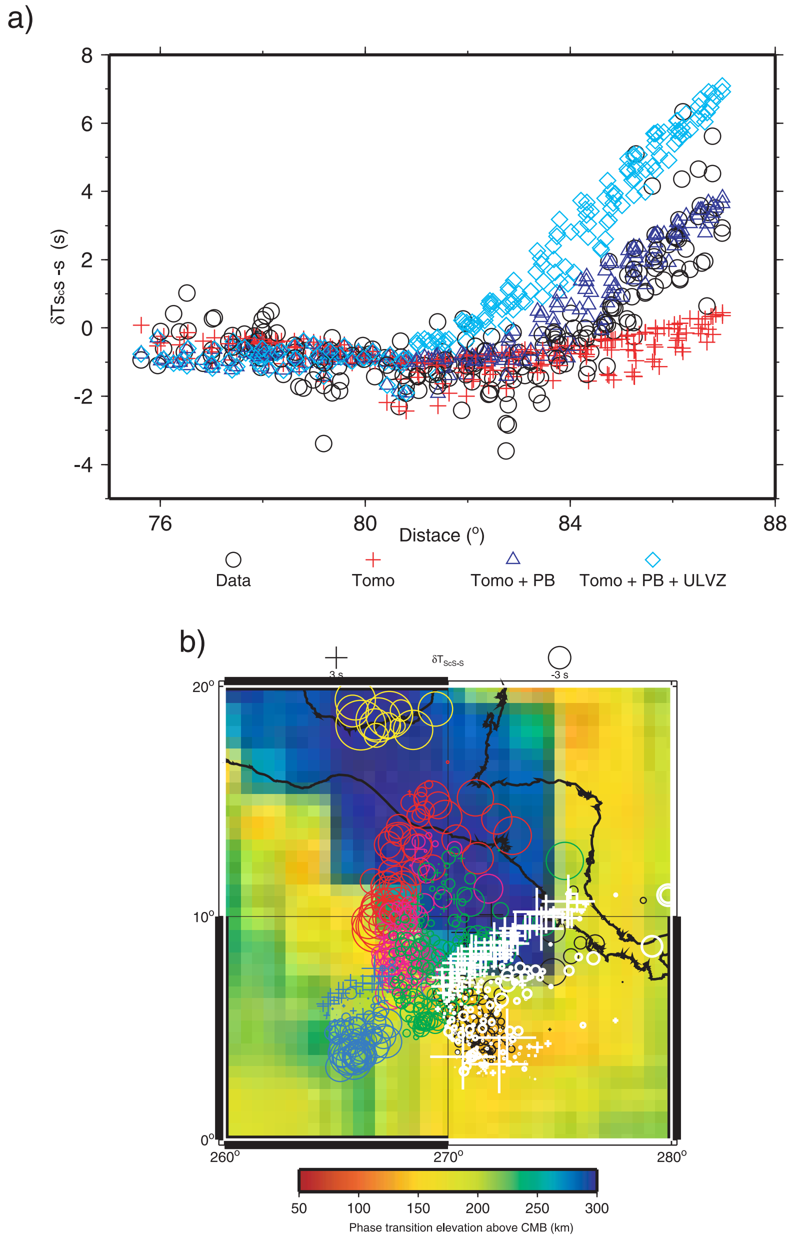

Figure 3.17: a) shows the data (event 20061113 in Figure 3.18) and the predictions for the differential ScS-S residuals. The models are Tomo (Grand's tomography model), Tomo+PB (phase mapping model), Tomo+PB+ULVZ (phase mapping model adding a ULVZ layer with 20 km height and -30% shear velocity reduction at the base of the mantle). b) The observed residuals of the differential ScS-S travel times with respect to PREM are plotted at the bounce points of the ScS on the CMB. Positive and negative residuals are indicated by the crosses and circles. Different colors relate to different events beneath South America. The bounce points of event 20061113 are marked by white symbols.

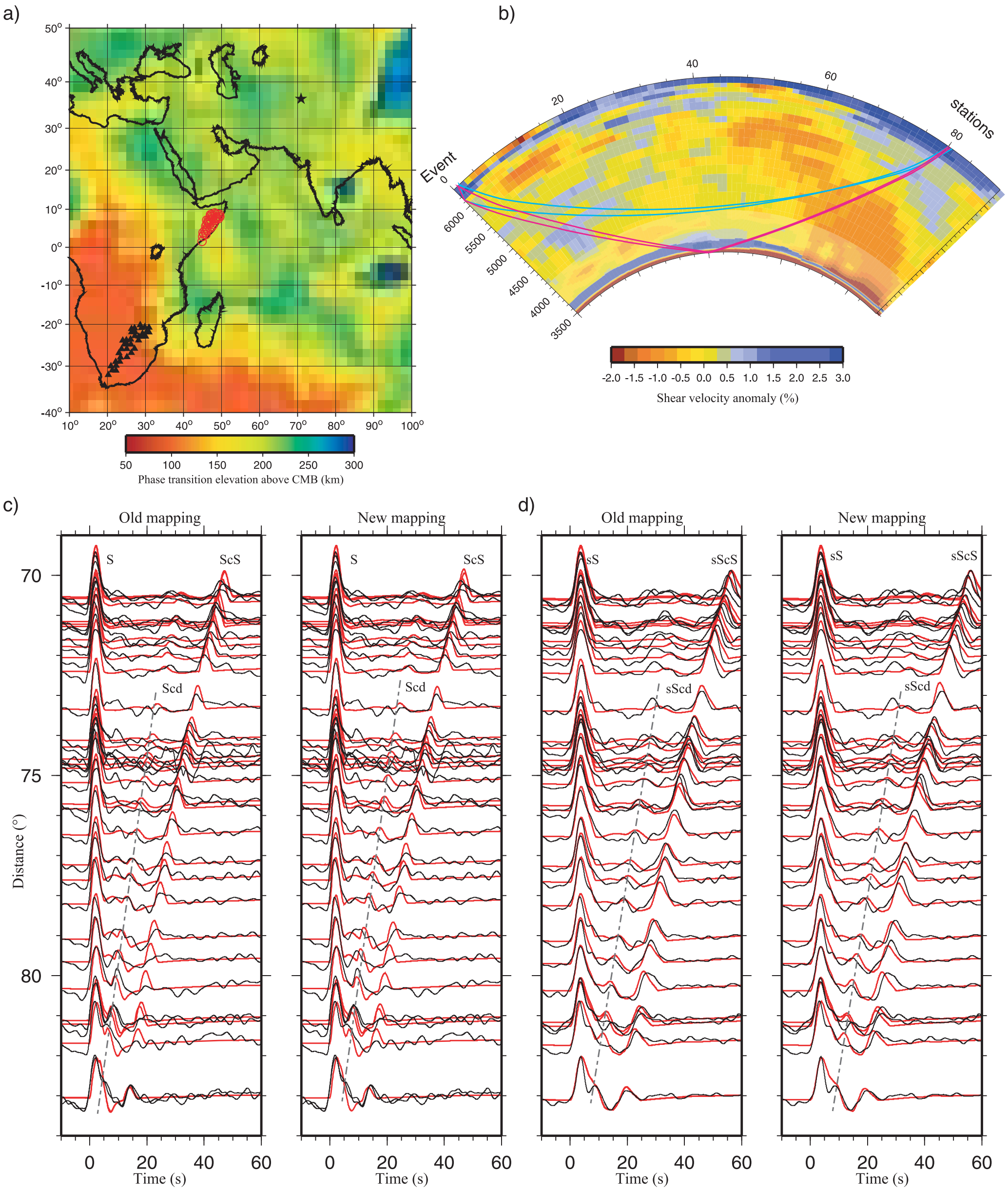

Figure 3.18: Display of S_{cd} sampling at a location where it has not been previously detected. a) Location of source (Hindu-Kush, Feb. 20, 1998; star), stations (Kaapvaal Array, triangles), and ScS bounce points (circles) at the CMB, plotted on the tomographic background [*Grand*, 2002] b) Ray paths of S and ScS (black) and sS and sScS (gray) with the shear velocity along the 2D cross-section from Grand's latest tomography model. c) and d) show comparisons of observations (heavy traces) and synthetics (light traces) for old mapping method (with adjusted h_{ph} = 160 km) from Sidorin's model [Sidorin et al., 1999] and new mapping introduced in this chapter.

tends to match the synthetics quite well at the smaller ranges but becomes delayed at the larger ranges. This feature is explained by the modeling of the Superdome [*Sun et al.*, 2007b] where ScS travels longer in the Superdome than does S.

3.7 Discussion and Conclusion

In this Chapter, we have revisited the earlier phase-transition mapping generated by Sidorin et al. [1999], Figure 3.1b. Their paper used the relative timing between Scd and S to determine γ = 6 MPa/K, β = 1.5% (velocity jump) and global phase boundary reference height h_{ph} = 200 km. This model predicts relatively uniform and strong Scd beneath fast regions but very small signals in other regions [*Kendall and Shearer*, 1994; *Russell et al.*, 1998]. We have solved this mapping difficulty by using waveform information and matching synthetics against observations for four well-sampled regions. The most significant difference between our results and the earlier model is the added strength of Scd in slow regions and the sharp gradients (Halo-like structures) around the fastest zones. A comparison of the two models for profile BB′ in Figure 3.16 is given in Figure 3.21 along with recent results from Wang et al. [2006] and van der Hilst et al. [2007] using a new inverse scattering method. These profiles essentially cross the structure along the same section with the fastest shear wave anomaly beneath the middle portion. In Figure 3.21, note that the left end of L1 ends at the same position where the new model steps down and there is a short span of weak signals in the upper images before stepping back-up. Their images also show an enhancement in low velocities just above the CMB beneath the elevated jump.

While the sharp contours in the phase boundary are becoming clearer in the S-velocities, the P-velocities appear to vary smoothly across this region, Figure 3.3a. This feature can be explained by the lack of any significant Pcd observed for this region [*Ding and Helmberger*, 1997], and the predictions from mineral physics [*Hirose*, 2006]. In short, the phase-boundary structure appears to be a shear-velocity feature where the high velocity slab material produces smooth high velocities in both P and S but no sharp feature without the phase-change. While the smaller-scale ULVZ-type features are interesting, we still lack a detailed description of where they are and their relationship with our model. However,

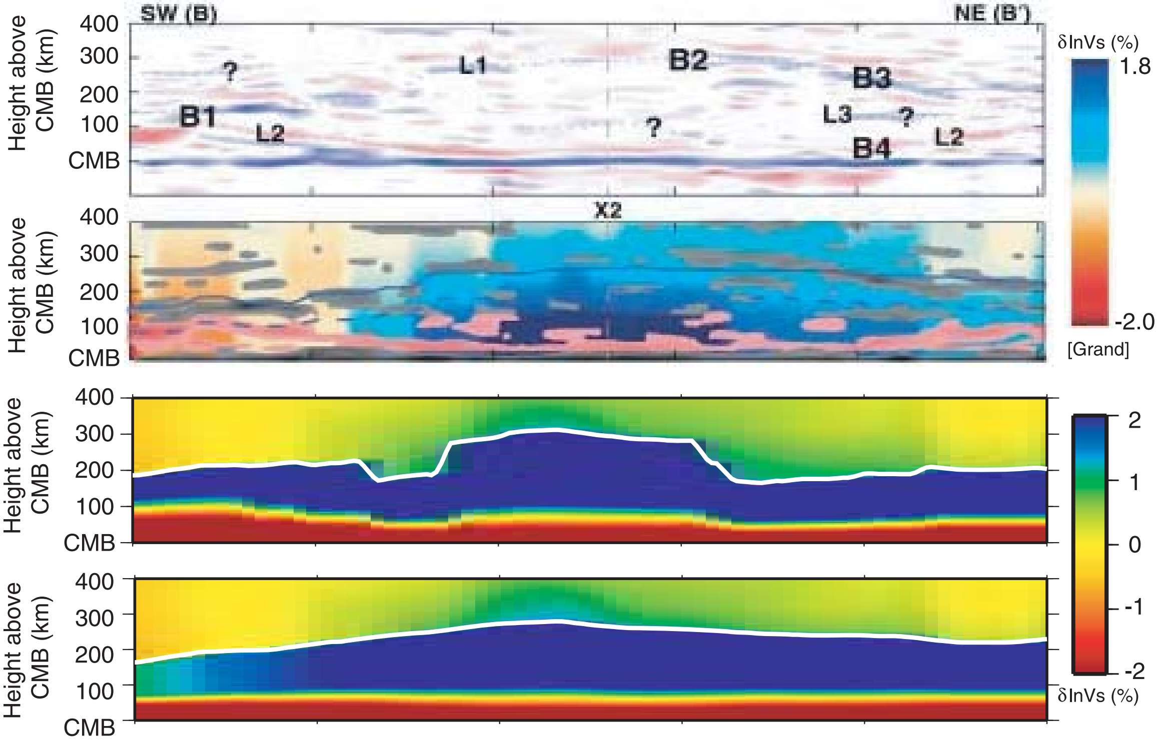

Figure 3.19: A comparison of results from different methods of phase boundary imaging for profile BB′ in Figure 3.16. The upper two panels display reflectors from inverse scattering techniques with positive reflections in blue (dark gray) and negative in pink [after *van der Hilst et al.*, 2007]. The lower of these two shows enhancement of the reflectors along with a solid blue line indicating phase transition location from the original Sidorin's model [*Sidorin et al.*, 1999] superimposed on Grand's tomography profile [*Grand*, 2002]. The bottom two models are our new phase boundary model and Sidorin's model. The phase boundary is indicated by white lines.

small-scale features of this description are predicted by some dynamic models [*Tan et al.*, 2002]. They also predict small-scale plumes along these boundaries which could help explain the sharpness of the mapped structure (Figure 3.21). Up-welling could cancel the cooling influence of slabs and, perhaps, the phase-change sharpness as well. This transition from fast-to-normal velocities is probably not that well imaged by tomography and awaits high-resolution studies.

Recently, broadband array measurements have demonstrated relatively strong Scd in regions other than the Pacific Ring of high-velocities. A particularly interesting feature of the V_s structure in the high bulk modulus metastable model is the down-welling region near the center (Figure 2.2d) that looks similar to global slab modeling. It appears that this feature should help produce a S_{cd} triplication which can, in fact, be seen in some data displayed in Chapter 2. There is also strong evidence for a S_{cd} phase near the western edge of the Pacific Superdome [*He et al.*, 2006], with a thickness of 100 to 150 km. Some evidence for a somewhat thicker zone along the eastern edge has been reported by Russell et al. [1998; 1999]. Lay et al. [2006] find a lens of PPV near the eastern margin of the mid-Pacific Superdome with a 2 to 3% jump in velocity by applying a double array stacking procedure. Note that this jump is in general agreement with our prediction in Figure 3.22.

Lastly, one could speculate on the role of temperature gradient, δT, in controlling the phase transition. Note that we have assumed a sharp phase transition (w_{ph} = 5 km) in the above analysis. Perhaps the phase transition has a more uniform onset globally but variable sharpness where the bulk of the transformation from PV to PPV takes place, as mentioned earlier in Figure 3.2 and Figure 3.11. Ohta et al. [2008] demonstrated the post-perovskite phase transition in both pyrolitic and MORB materials occurs within a 5GPa pressure range, which correspond to a lower mantle depth range of 90 km. The seismic synthetics for models with different transition thicknesses (Figure 3.11) indicate that seismic data are not particularly sensitive to the sharpness of the phase transition at the distance ranges of 75°~85°.

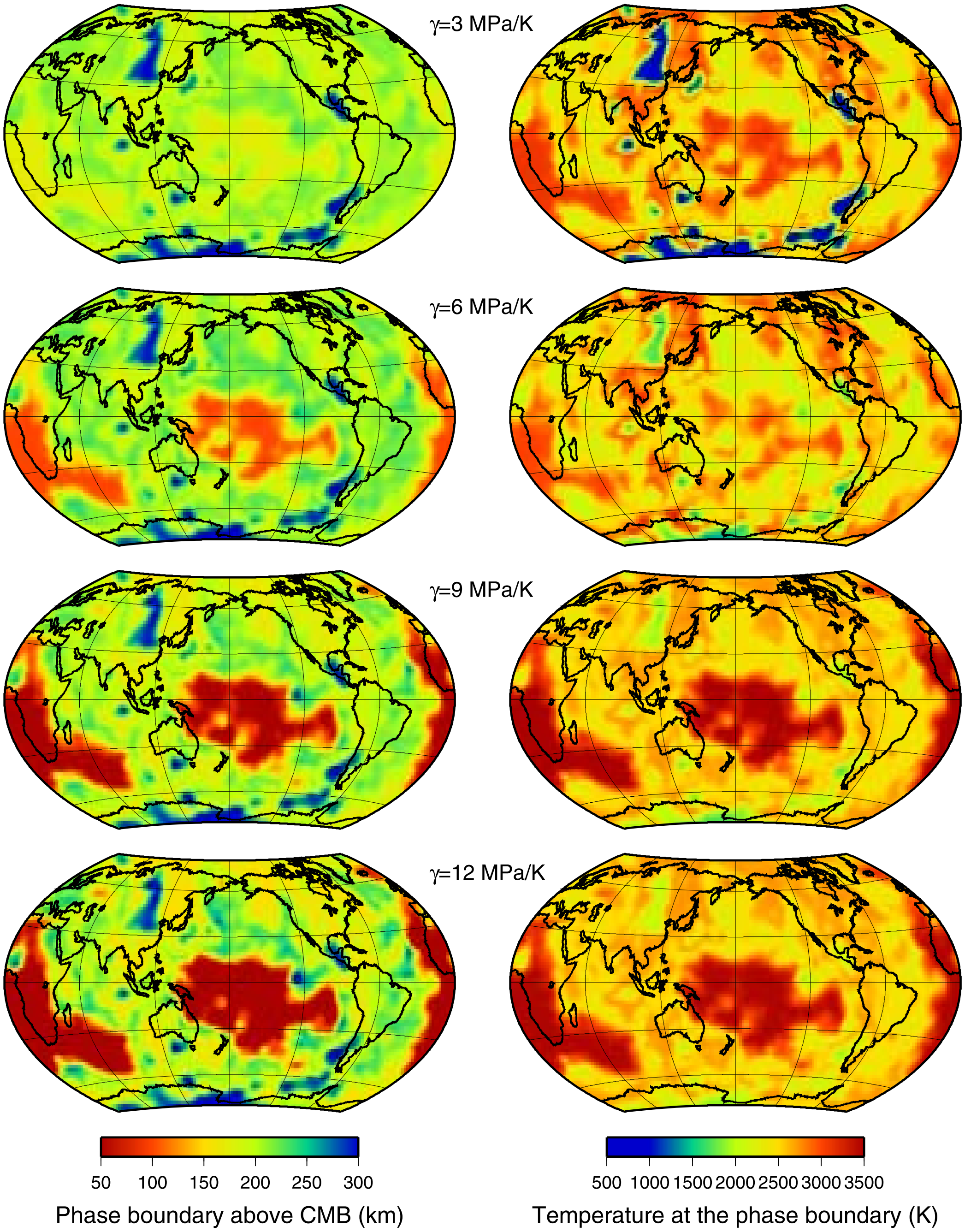

Figure 3.20: The global prediction of a) phase boundary height above CMB for various γ's and b) temperature at the phase boundary for these γ.

Another difference between the new model and Sidorin's old model is the shear velocity jump for slow velocity regions. The 3.5% velocity jump across the phase boundary is much higher than Sidorin's velocity jump (1.5%) and theoretical calculation for perovskite to post-perovskite transition (-1% - 1.5%) [*Ohta et al.*, 2008]. If a high degree preferred orientation of post-perovskite is needed to explain this high shear velocity jump, a strong anisotropy is expected in the lower mantle in this region [*Hirose*, 2006].

Significant seismic anisotropy has been observed in several regions of the lowermost mantle [*Garnero and Lay*, 1997; *Lay et al.*, 1998; *Matzel et al.*, 1996; *Thomas et al.*, 2007]. Beneath the D" discontinuity, the detected horizontally polarized S wave velocity (V_{SH}) is faster by 1–3% than the vertically polarized S wave velocity (V_{SV}). Sun et al. [2007] report the existence of the D" discontinuity beneath the center of African Superdome (slow velocity region) from the SV component. The different anisotropy behaviors between the fast and slow velocity region could be related to the dynamic flow pattern in each region. At the edge of the fast velocity region, the flow pattern could be greatly affected by the buckled slab, which will produce complicated Scd behavior in such regions.

With the function of $h_{ph}(\delta Vs)$ and $\beta(\delta Vs)$ defined as in Figure 3.9, we can generate global phase boundary maps (Figure 3.22) for various γ assuming Grand's tomographic model. Small γ produce smooth variations of the phase boundary. When γ = 3 MPa/K, the heights of the phase boundary above CMB (h) beneath Africa and Central Pacific (slow velocity region) are larger than 150 km. The phase boundary height beneath Central America and Eurasian (high velocity region) is about 300 km. For increased γ, the difference of h between the slow velocity and high velocity region becomes larger. The height of phase boundary is ~50 km beneath Africa for γ = 9 MPa/K. Sun et al. [2007] obtained evidence for a possible phase change at about 80 km above the CMB beneath South Africa which is in rough agreement. Although it is difficult to sample the D" region beneath the slow regions because of source-receiver locations, these few observations suggest that $\gamma > 6$ MPa/K.

Based on the above analysis, we can estimate the global mantle temperature at the phase boundary. We assume a reference point with the pressure (P) of 124 GPa and the temperature (T) of 2500 K [*van der Hilst et al.*, 2007]. All the phase boundary lines with different γ intersect at this reference point. The temperature for given height of the phase boundary can then be estimated by assuming

$$T = 2500 + \frac{P - 124}{\gamma}. \tag{2.4}$$

The global temperature distribution at the phase boundary is shown in Figure 3.22. When γ = 3 MPa/K, the temperature at the high velocity region is less then 600 K. The high velocity region is believed to be related to an old subducted slab, which has much higher temperature than 600 K [*Tan et al.*, 2002]. Therefore, γ larger than 6 MPa/K is required for producing reasonable temperature for the slab-debris in the lowermost mantle based on present PV-PPV experiment results. A large γ (γ ≈ 9 MPa/K) agrees with the results on reconciling the core temperature and post-perovskite double crossing [*Hernlund and Labrosse*, 2007] and recently experimental result with the MgO standard [*Hirose*, 2006].

The chemical heterogeneity in the lower mantle has been well accepted. Unavoidably, the change of chemistry will add more complexity to the phase boundary [*Ohta et al.*, 2008]. Moreover, the local dynamics will play an important role on the phase change. For example, the edge of a subducted slab just above the CMB could trap significant heat [*Tan et al.*, 2002], which will move the phase boundary toward the CMB (Zone C). To address these questions will require further efforts in geodynamics, mineral physics, and more detailed seismological studies.

Chapter 4

Direct Measures of Lateral Velocity Variation in the Deep Earth*

4.1 Abstract

Current tomographic models of the Earth display perturbations to a radial stratified reference model. However, structures in the deep mantle that are chemically dense with low Rayleigh numbers can develop enormous relief, perhaps with boundaries closer to vertical than radial. Such features are hard to detect with present tomographic modeling technique because the timing anomalies are based on long period filtered waveforms with complexity removed. Here, we develop a new tool for processing array data based on a decomposition referred to as a multi-path detector which can be used to distinguish between horizontal structure (in-plane multi-pathing) vs. vertical (out-of-plane multi-pathing) directly from processing array waveforms. A lateral gradient coefficient based on this detector provides a direct constraint on the sharpness of the boundaries and material properties. We demonstrate the usefulness of this approach by processing samples of both P and S data from the Kaapvaal array in Southern Africa which are compared with synthetic predictions from a metastable dynamic model containing sharp edges. Both data and simulations produce timing gradients larger than 2 s/deg in azimuthal changes for S-waves, whereas only minor effects are obtained for P-waves. These results further validate

---

*This chapter appear as Direct Measures of Lateral Velocity Variation in the Deep Earth, Daoyuan Sun, Don Helmberger, Sidao Ni, and Dan Bower, *Jounral of Geophysical Research* (2009), 114, B05303, doi:10.1029/2008JB005873.

the case for distinct chemistry inside the African Low Shear Velocity Province. We also present evidence of a narrow plume-like feature emitting from the top of the large African low-velocity structure in the lower mantle. The plume's diameter is less than 150 km and is consistent with an iso-chemical, low-viscosity plume conduit.

4.2 Introduction

The upper mantle and crust display strong stratification apparently caused by mineral density differentiation. Record sections of upper mantle triplications indicate discontinuities in seismic velocity jumps at depths near 410 and 660 km depth in both P and S velocity [*Grand and Helmberger*, 1984; *Shearer*, 1993]. These features have been studied globally [*Shearer*, 1993], and are well accepted supporting a radial stratified mantle. However, [*Masters et al.*, 2000] argue for less uniformity in P and S velocity compatibility in the lower mantle, leading [*Anderson*, 2002] to speculate on chemically based structure. He concludes that such a layer would have high conductivity and viscosity but very low thermal expansivity (small thermal buoyancy). Thus, in contrast to conditions in the upper mantle, dynamically generated features in the lower mantle are predicted to be sluggish, long-lived, and perhaps develop enormous relief [*Davaille*, 1999; *Gonnermann et al.*, 2002; *Gurnis et al.*, 1998; *Hansen and Yuen*, 1989; *Kellogg et al.*, 1999; *Tackley*, 2000; *Tan and Gurnis*, 2005; 2007].

We can test for these types of predictions by searching for sharp velocity gradients which may be oriented more vertically than horizontally. One method to achieve this is to examine how wavefronts arrive at broadband two-dimensional arrays such as the Kaapvaal array in South Africa as displayed in Figure 4.1. The various traces contain the diffracted SH phases sampling produced by two deep earthquakes, one in the Western Pacific (A) and one beneath South America (B). The record sections in Figure 4.1 are plotted with respect to the travel time predictions from PREM [*Dziewonski and Anderson*, 1981]. That is, each record is shifted in time for a distance correction such that it should be perfectly aligned along the reference line at position zero if the Earth is adequately modeled by PREM. An example of a record section for event A plotted as a function of distance is given in Figure 4.1b, and in azimuth in Figure 4.1c, a so-called "fan-shot". The latter presentation is a

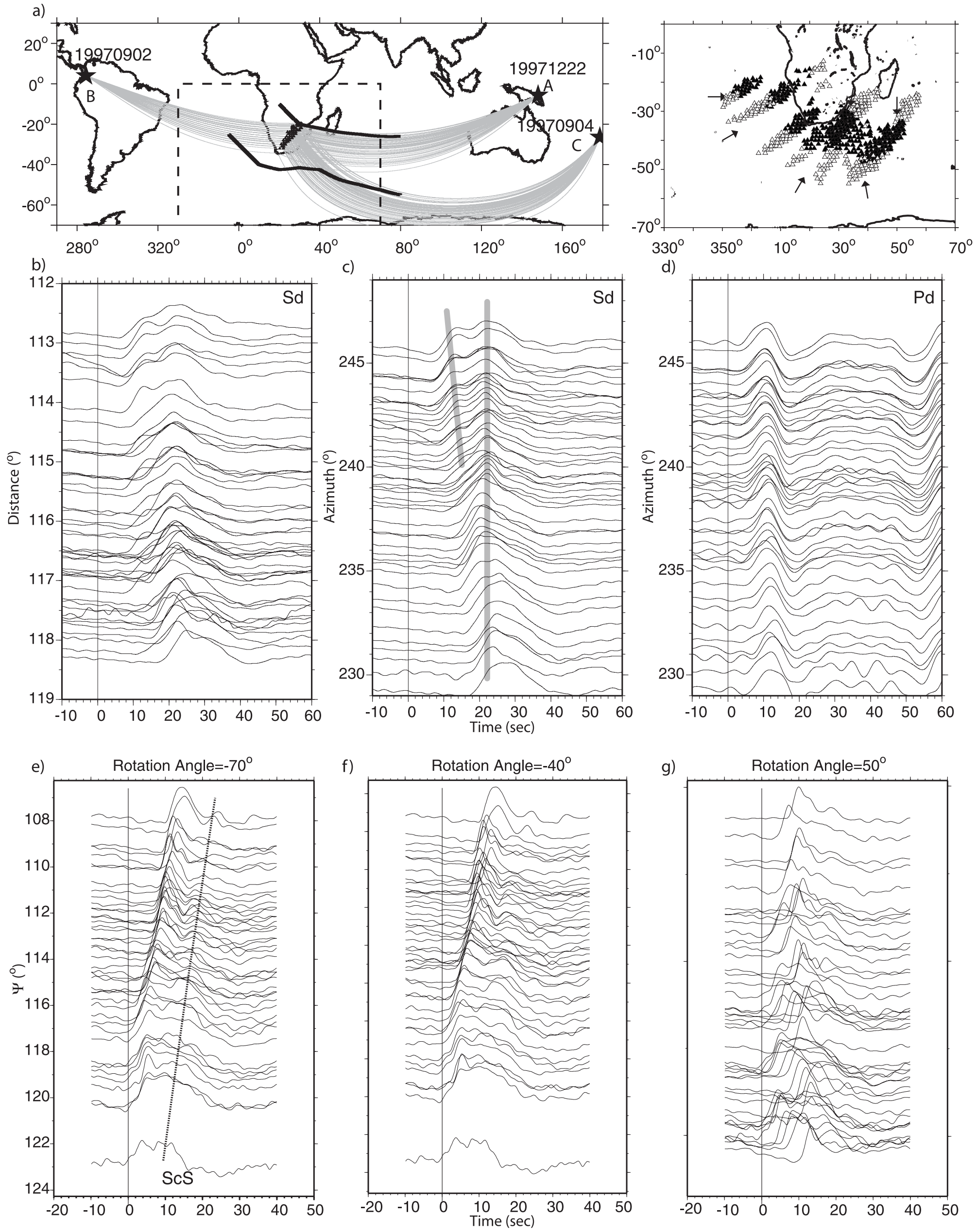

Figure 4.1: Display of event paths and observations from the Kaapvaal Array. (a) Locations of three deep earthquakes and their great circle paths to the array (left) and a blow-up of a pattern of SKS-SKKS delays (exit points at the CMB) associated with the boundary of the African Superdome (right). Delays of more than 5 s are shown in closed triangles. Open triangles indicate no delay. The solid black line in a) indicates the approximate position of the African Superdome. S_d data from event A is displayed in (b), plotted with distance (record section) with azimuth in (c) (fan-shot) and P_d data in (d). The e), f), and g) display the waveform data from event B plotted as a function of ψ, a combination of distance and azimuth as addressed in the text.

common oil exploration tool to detect salt domes. The plot of event A in azimuth (Figure 4.1c) shows more order, with uniform behavior from trace-to-trace in timing and shape. Thus, we suggest that the structure is varying more in azimuth than in distance and that the structure is oriented more vertically than radially. We have included a set of heavy lines in the azimuthal plots for event A (Figure 4.1c) to indicate pulses associated with distinct paths. The first heavy line in Figure 4.1c corresponds to relatively fast paths that avoid the slow structure by taking a northerly route. The second heavy line denotes delayed signals following slow paths sampling inside the structure. Such complexity or multi-pathing is expected for rapidly varying structures and can be modeled accordingly [*Ni et al.*, 2005].

While the S-waves display strong azimuthal patterns, the P-waves remain PREM-like as displayed in Figure 4.1d. The events examined in this study and other recent reports do not show many recognizable P-wave anomalies [*Ni and Helmberger*, 2003a; b; c; *Wen et al.*, 2001]. The uniformity of the P-waves suggests neglectable upper mantle variation beneath the stations which is in agreement with the studies by James et al. [2001]. Moreover, since we are analyzing the same event, we are avoiding the many problems concerning records assembled from multiple earthquakes, such as individual source excitations, uncertain locations and origin times, which tend to smooth tomographic images.

SKS ray paths from the southwest encounter the structure at right angles to the anomalous structure where the delay can be seen directly, varying roughly 6s over a distance of a few degrees, Figure 4.1a. Such time delays are measured by cross-correlation and delays relative to PREM projected along the ray paths to their Core-Mantle Boundary (CMB) exit points as displayed, see *Helmberger and Ni* [2005b] for details. Note the sharp jump from distinct boundaries which delineate a broad structure changing from a northwestern orientation to east-west below South Africa.

The delay gradient can also be seen directly in seismic sections as displayed in Figure 4.1e where ray paths approaching the array from the west sample the structural boundary at an angle so that the wavefront is not perpendicular to the great circle path. To estimate this angle (θ), we simply perform a grid search of distance-azimuth combinations or ψ =

Distance × Sin θ + Azimuth × Cos θ until we find the most orderly section in waveform shape and timing. The angle is measured relative to the true azimuth so that ±90° corresponds to a normal distance section and 0° to pure azimuthal plot as given in Figure 4.1c. An example of a mixture in distance and azimuth is given in Figure 4.1e-g. Note that the upper group of records for event B prefers a -70° approach while -40° fits the lower half better. This indicates the gradual changes to east-west for the southernmost portion of the array. We have included a northeast orientation (-50°) that shows the most disorder for comparison (Figure 4.1g).

The waveform data recorded by the array from the various sources have been processed to estimate their preferred delay gradient directions indicated by arrows with the results included in Figure 4.1a. The general pattern is quite clear with the arrows consistently pointing towards the middle of the structure. The same pattern is produced by the SKS and SKKS delays, which is based solely on relative timing [*Ni and Helmberger*, 2003b]. However, some of these SKS appear to be multi-pathed which occurs along the boundaries. Many of the observations recorded by the Kaapvaal array have been modeled following two distinct strategies, one involving pure 2D (in-plane, Figure 4.1b) [*Wang and Wen*, 2007] and the other involving azimuthal multi-pathing (out-of-plane, Figure 4.1c) modeling [*Ni et al.*, 2005]. An earlier effort by Wen [2001] produced an excellent fit to individual records where the data in Figure 4.1c (event A, 971222) is broken into sectors of azimuth and modeled with a hybrid numerical formalism. In this case, the large second arrival is actually a delayed ScS produced by a very slow basal layer (δV_s = -12%). This second arrival can also be produced by an out-of-plane arrival. Thus, the interpretations of the two approaches produce different models. These two models have distinctly different physical interpretations as well. Gently sloping walls over a very low velocity basal layer favors “stable piles” [*McNamara and Zhong*, 2004] while more vertical walls with more uniform internal structure favors the “metastable” type interpretation proposed by [*Tan and Gurnis*, 2005; 2007]. Thus, to address these important issues, we will introduce a new method of using array data such as in Figure 4.1, to address in-plane vs. out-of-plane propagational features directly. The method relies on the organization of the waveform complexity with the relative timing between arrivals as a function of position. We introduce the approach with a review of a hybrid method of generating 3D synthetics, which suggests that out-of-plane arrivals can be simulated by using diffraction operators. Each observation is then approximated by four arrivals which sample the extended Fresnel zone. The array of observations is then replaced by a footprint of timing shifts between interfering arrivals. To interpret these maps, we present a set of training exercises on synthetics to develop a Multi-path Defector (MPD) scheme which uses the gradient in differential arrivals to determine in-plane vs. out-of-plane patterns. Then we apply MPD on two real data profiles to demonstrate the sharp edges of the African Superdome.

4.3 Methodology

Dense arrays, as discussed above, are displaying obvious waveform complexities, which makes travel time picking difficult. The usual solution adopted in tomography is to low-pass filter until the waveforms are similar enough to cross-correlate [*Masters et al.*, 2000] or pick the first arrival. Here, we will introduce a new approach that uses more of the waveform complexity to infer the presence of sharp boundaries. We will begin with a numerical simulation of a simple block model with sharp walls followed by a brief review of a recent technique developed to treat 3D structure. To illustrate azimuthal multi-pathing, we generate synthetics for a uniform Low Velocity Structure (LVS) embedded in PREM displayed in Figure 4.2 using the 3D spectral-element method (SEM) [*Komatitsch and Tromp.*, 2000a; b]. The synthetics were generated on a fine grid showing the effects of paths crossing the sharp wall with two record sections displayed, one as a function of azimuth (Figure 4.2b) and a normal function of distance record section (Figure 4.2c). For azimuths near 270°, two arrivals of nearly the same amplitude are apparent with one lagged by about 10s corresponding to the slow path inside the LVS. A similar pattern can be seen along the other wall near 245°. The first arrival times produce a simple pattern (Figure 4.2a on right) indicating the delayed patch of arrivals with a transition zone given along the edge which we want to explore in terms of developing a new tomographic approach. In particular, we address a method of characterizing the waveform distortion such as displayed in Figure 4.2 in a relatively simple manner in preparation for constructing a seismic model using ray paths as presented in [*Zhu and Helmberger*, 1998].

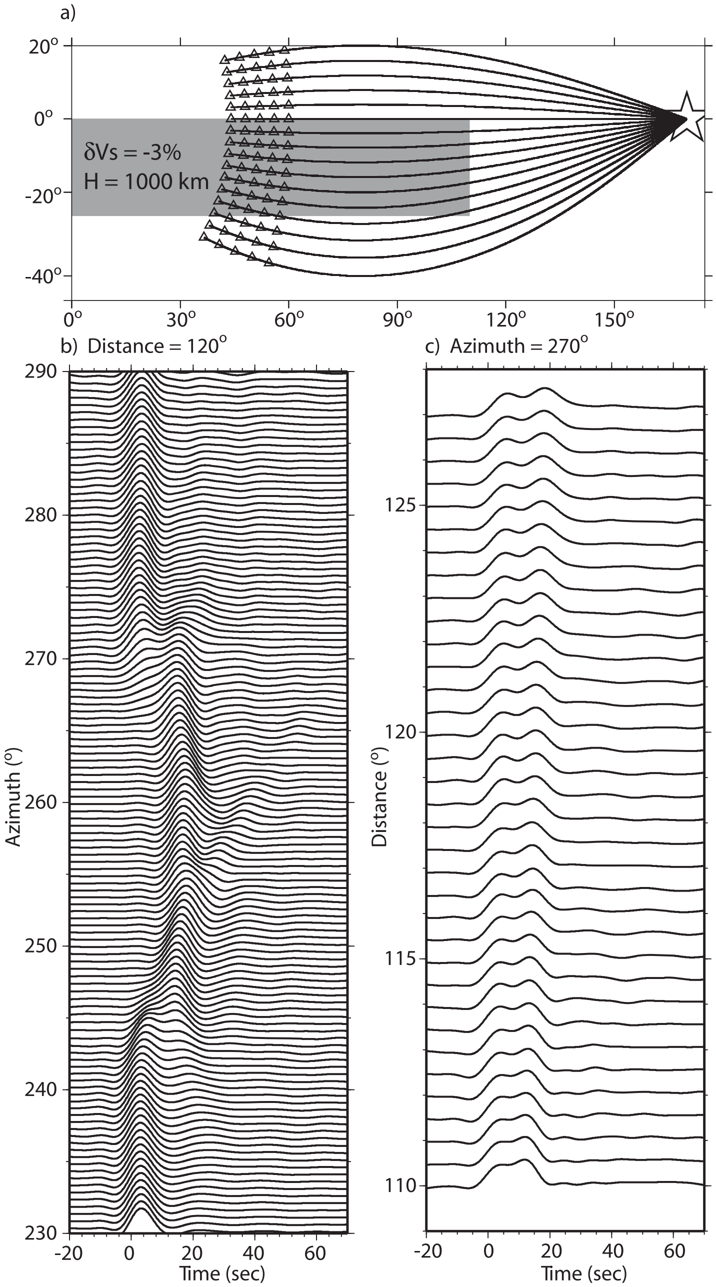

Figure 4.2: Synthetic seismograms generated by SEM for the model given in (a) along with source-station geometry. (b) Fan-shot at a constant distance of 112°. A record section in distance appropriate for an azimuth of 270° is presented in (c).

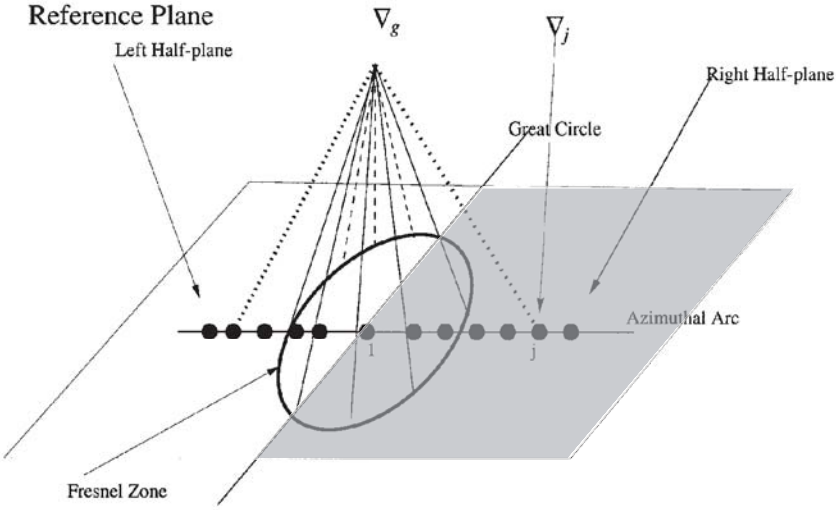

Figure 4.3: Construction of a reference plane directly above an edge is displayed where the great-circle is along the edge. The Fresnel zone is indicated as a circle with half above the slow zone (right-shaded) and half normal (left). We have included a line of samples along an azimuthal arc where a 2D summation over the plane is replaced with a line integration.

One useful approach in treating such problems is to introduce a reference plane and use Huygen's principle. Suppose we place such a plane above the box and examine the arrivals along the edge where a great circle path is located, Figure 4.3. A solution can then be generated by summing over paths connecting every point on a 3D grid to the source and receiver [*Scott and Helmberger*, 1985]. An exact solution can be generated in this way as demonstrated in Helmberger and Ni [2005]. Fortunately, we can reduce this 3D summation to an integration along a line as indicated in Figure 4.3 and still further to the summation of just four responses by applying a sequence of approximations. Thus, we start with a brief review of generating approximate synthetics for testing against those displayed in Figure 4.2.

4.3.1 Brief review of approximate methods.

A well known technique for generating 1D synthetics was introduced by Chapman [1976], called the WKBJ method. The displacement wave-field can be written as

$$V(r,z,t) = \frac{d}{dt}\left[\dot{D}(t) * \frac{1}{\sqrt{t}} * G^2(r,z,t)\right] \tag{4.1}$$

where $\dot{D}(t)$ is the far-field time history of a simple shear-dislocation. G^2 is a 1D or 2D Green's function where the model has no azimuthal dependence

$$G^2(r,z,t) = \sqrt{\frac{2}{r}}\frac{1}{\pi}\Psi(r,z,t) \tag{4.2}$$

and r is the radial distance along an earth-flattened model, with z the vertical coordinate and ψ (r, z, t) the line source solution [*Chapman*, 2004]. The operator $\left(1/\sqrt{t}\right)$ and the $\left(1/\sqrt{r}\right)$ essentially correct for the distance dependence in 2D propagation and extra amplitude decay associated with 3D spreading. The function ψ (r, z, t) relates the ray parameter $\left(p_i\right)$ to the travel times $\left(t_i\right)$ for a family of paths arriving near the receiver. The WKBJ amplitudes can be approximated by

$$\Psi(r,z,t) \approx \sum\left(\frac{\delta p_i}{\delta t_i}\right) \tag{4.3}$$

where (δ) measures the differences between neighboring paths. For smooth velocity structures, δt_i approaches zero at the first arrival (t_o), and

$$\Psi(r,z,t) \approx \frac{H(t-t_0)}{\sqrt{t-t_0}} \ . \tag{4.4}$$

As discussed in box 9.8 of Aki and Richards [2002] Equation (4.1) becomes

$$V \approx \frac{d}{dt}\left[\dot{D}(t) * \frac{1}{\sqrt{t}} * \frac{H(t-t_0)}{\sqrt{t-t_0}}\right] \cong D(t-t_o), \tag{4.5}$$

where $\dot{D}$ is the source time function.

Note that the $\left(1/\sqrt{t}\right)$ operator was obtained by assuming axial-symmetry. Thus, in situations such as Figure 4.3, the arrivals from left to right vary in azimuth but remain weighted by their distance from the geometric great circle path (Δ_g). Thus, geometry plays an essential role and the sampling in azimuth becomes similar to (δp_i) in the radial distance with points nearest Δ_g contributing relative to a square-root singularity, as indicated in Figure 4.4. We can simplify this convolution operator by assuming ψ (r, z, t) is slowly varying relative to $1/\sqrt{t-t_o}$ near $t = t_o$ and compute ψ at four locations controlled by the Fresnel zone. We define its radius to be

$$\Delta_f = \sqrt{\delta_\alpha^2 t_e T} \tag{4.6}$$

where t_e is the differential travel time to the feature causing the complexity, δ_α the average velocity and T the source duration. We then compute ψ (r, z, t) at Δ_l and Δ_d defined by

$$\Delta_l = \sqrt{\delta_\alpha^2 t_e T/4} \text{ and } \Delta_d = \left(\sqrt{2}+1\right)\Delta_l \tag{4.7}$$

corresponding to the lit and diffraction zone. Next, we assume the seismic model is smoothly varying above the reference plane and compute ψ at the surface. Adding Δs will produce a broad band response as in adding ray paths in WKBJ theory, see [*Helmberger and Ni*, 2005a] for details. Thus, to approximate non-great-circle path contributions, we generate

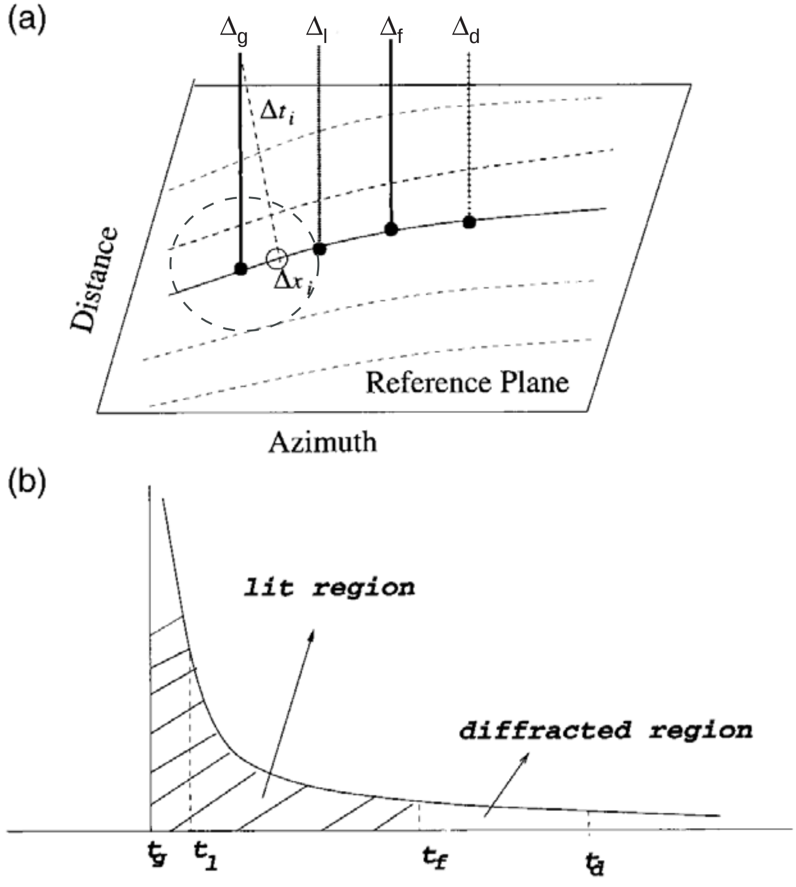

Figure 4.4: Presentation of a simplified Kirchhoff secondary source summation procedure. (a) Reference surface positioned above a 3D target structure where we replace a grid summation with an approximate solution. Four locations are indicated corresponding to projections to the surface; Δ_g the geometric path, Δ_l a sample of the lit region, Δ_f the Fresnel zone limit, and Δ_d a sample of the diffracted contribution. The dotted lines represent paths of constant distance. (b) The $\left(1/\sqrt{t}\right)$ convolution operator with t_l indicating the half area position under the curve approximation which ends at t_f, similarly t_d from t_f to ∞.

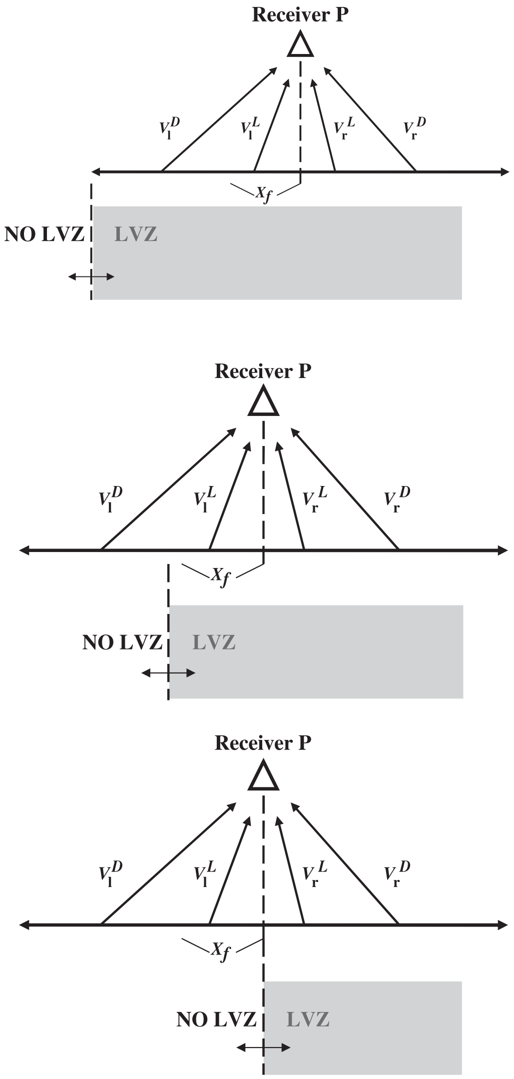

Figure 4.5**:** Cartoon displaying the sampling of LVZ (shaded) vs. normal (white) at right angles to the great-circle path with four contributions, two lit $V_r^L \textit{ and } V_l^L$ and two diffracted $V_r^D \textit{ and } V_l^D$. Note that the long-period diffractions can be early as in the middle panel or late as the receiver moves to the right.

$$V(r,z,t) = O_L * G_R^2(\Delta_l) + O_D * G_R^2(\Delta_d) + O_L * G_L^2(\Delta_l) + O_D * G_L^2(\Delta_d) \qquad (4.8)$$

assuming that the right side and left side have distinct responses at Δ_e and Δ_d on each side. The operators are weighted by their distance away from Δ_f with t_f the extra time taken to travel to the Fresnel edge, or

$$O_L = \frac{d}{dt}\left[\left(\frac{H(t)}{\sqrt{t}} - \frac{H(t-t_f)}{\sqrt{t}}\right) * \dot{D}(t)\right]$$

and

$$O_D = \frac{d}{dt}\left[\frac{H(t-t_f)}{\sqrt{t}} * \dot{D}(t)\right] . \qquad (4.9)$$

Figure 4.5 displays a diagram indicating the simulation relative to the boundary and Figure 4.6 presents the synthetics generated from the application of expression (8). All four responses sample the box at azimuths 250° to 265°. At 268°, one sample, Δ_d on the left, encounters the faster velocity and arrives early. Note its longer period nature. Directly above the edge, two early and two late arrivals interfere. Note that these synthetics compare well with those given in Figure 4.2 for wall crossings. In this zone, the relative timing differential between the right and left is the most obvious and can be used to generate the new tool, namely, the Multi-Path Detector (MPD). If we focus on short-periods, we can greatly simplify the procedure and treat only the left and right aspects of the field.

$$V(t) = O * G_R^2(\Delta_l) + O * G_L^2(\Delta_l) \qquad (4.10)$$

where

$$O(t) = \frac{d}{dt}\left[\frac{1}{\sqrt{t}} * \dot{D}(t)\right] \qquad (4.11)$$

which becomes the point source solution. A common practice in modeling a triplication is to pick a simple pulse from a forward branch and assume it is $\dot{D}$(t), or empirical source history [*Gilbert and Helmberg*, 1972]. Thus, we assume that any observation is constructed

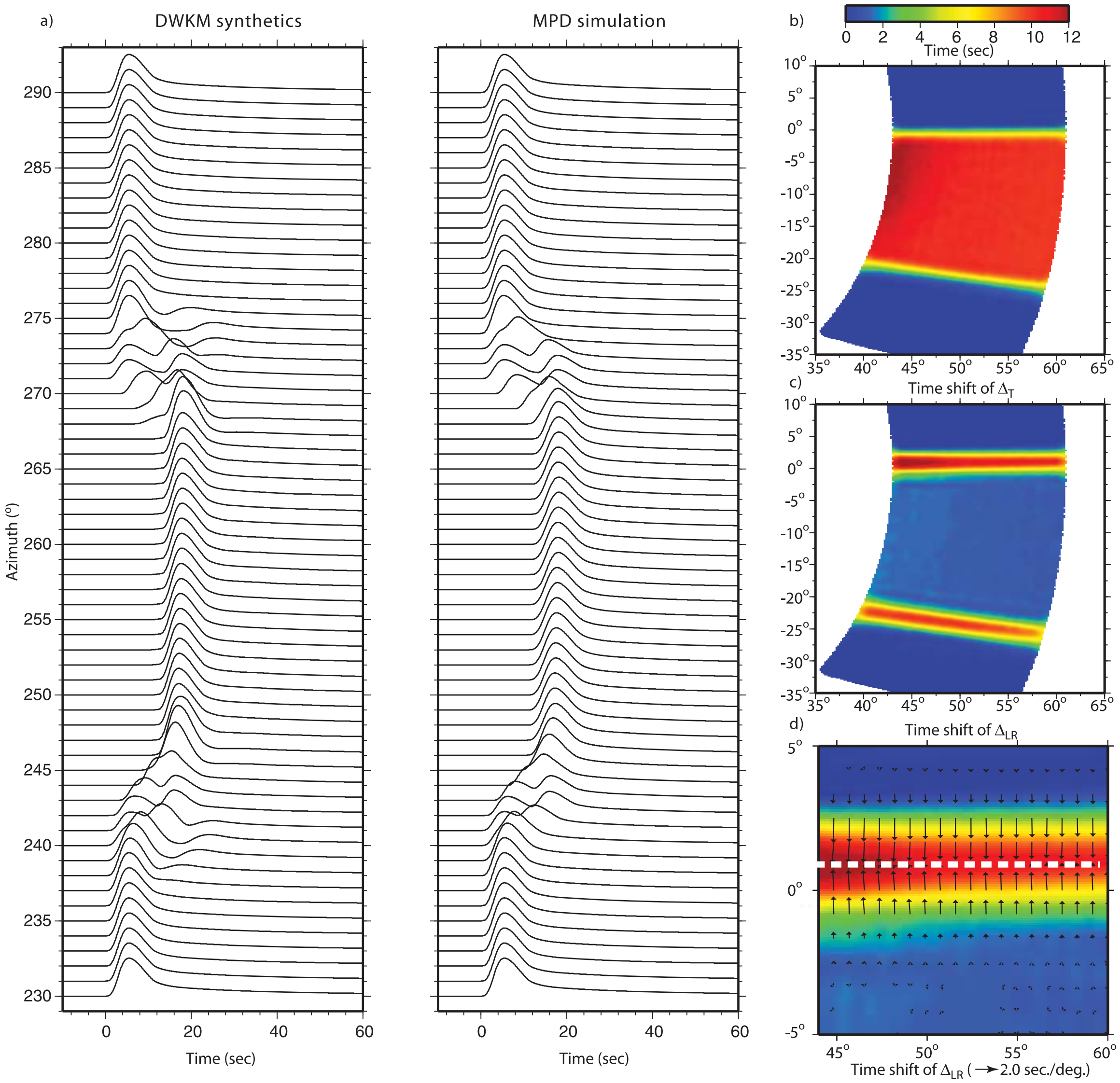

Figure 4.6: Synthetic training exercise with the problem setup displayed in Figure 4.2a used in the SEM simulation. A comparison of 3D synthetics (DWKM) and MPD results are displayed in a), and large array time delays given in b), c), and d). The results are color-coded. The edge structures are highlighted with dash white lines in d).

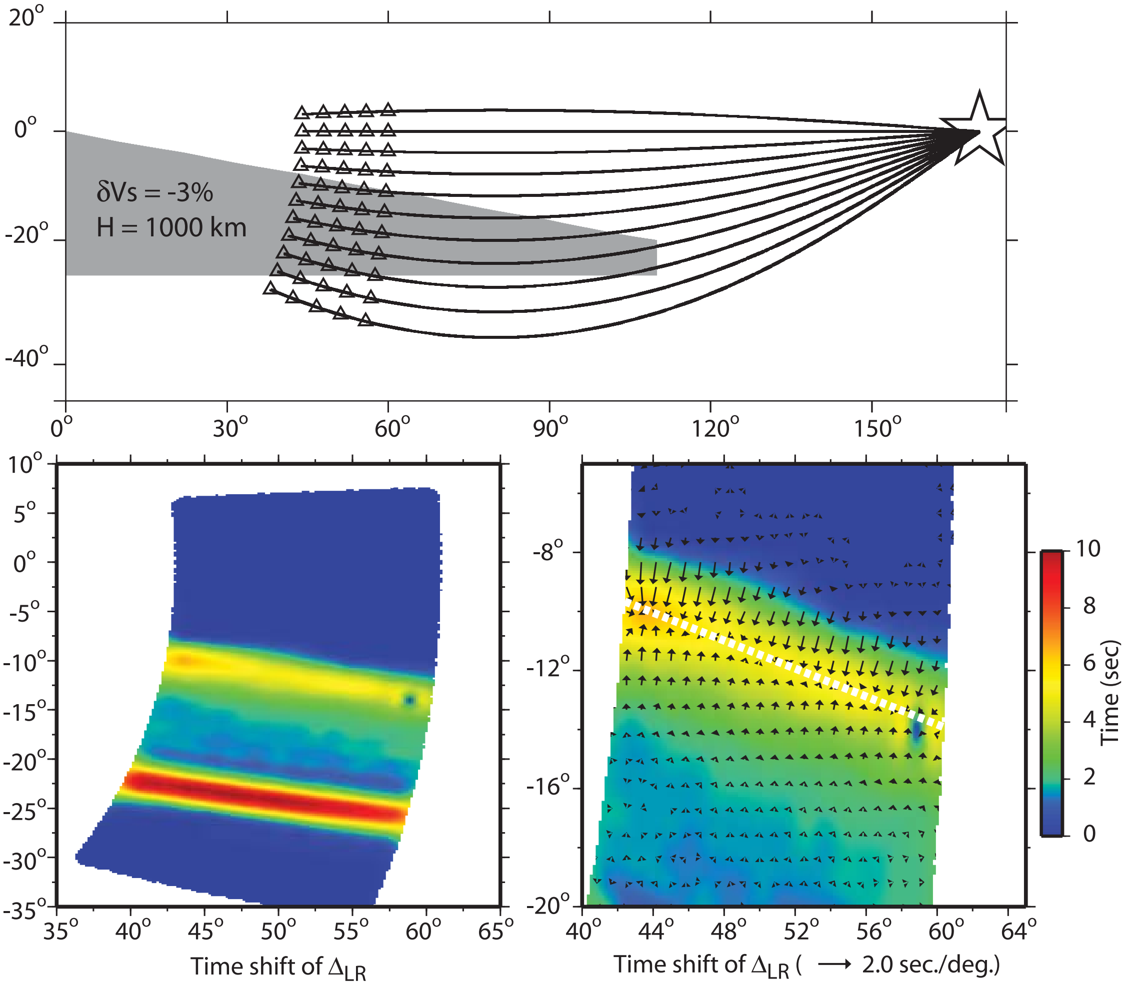

Figure 4.7: Synthetic training exercise for more complex structures containing a “tapered ended” large low velocity

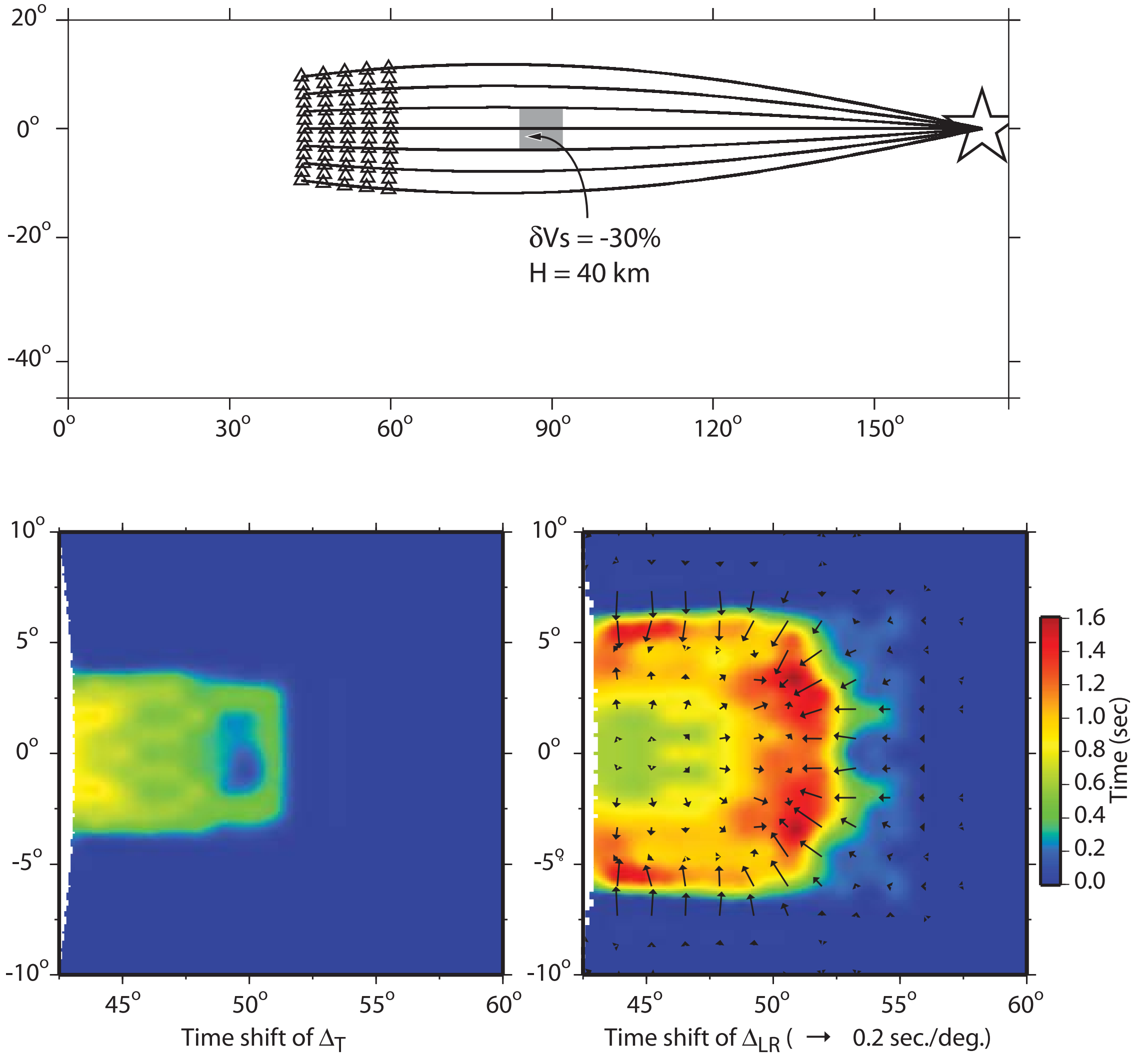

Figure 4.8: Synthetic training exercise for more complex structures containing a ULVZ sample at the bottom

from $O(t)$ (Equation 4.9) but split by some δt, which is obvious in Figure 4.6. We can then determine the timing shift and reference beginning time by direct grid search of each seismogram. This approach generated the simulations in Figure 4.6. Note that we lose the diffracted tails but still pick-up the edges very well. We recover two timing delays. One associated with the shift between the left and the right branches (Δ_{LR}), and the other between the entire simulation relative to the reference model or total delay (Δ_T). The differential times generated from a 2D array can then be used to construct the spatial gradient of these delays as displayed on the right in Figure 4.6. These correspond to the two wall cross-over which are slightly different caused by the geometry. The arrows perpendicular with the radial direction suggests the waveform distortions are caused by out-of-plane multi-pathing. Note that the vectors change sign at the maximum in shift denoted by a heavy dotted white line which indicates the edge of the structure is parallel with the radial direction. For the structure in Figure 4.7 which incorporates a tapered end, the "zero gradient" line crosses the radial direction at an angle (Figure 4.7). The analyses, again, retrieves the angle between the edge of the structure and the radial direction. Synthetics from an idealized ultra velocity zone (ULVZ) structure are given in Figure 4.8. Note that the arrows become parallel with the radial direction indicating that this structure will cause mostly radial direction multi-pathing (in-plane). Thus, the footprints generated with the MPD analysis of array data can be used directly to determine if the edges of a structure are in-plane or out-of-plane. These examples are highly idealized and the issue of applicability to more complex structures needs to be addressed. For such a demonstration, we chose a dynamic model for the African Plume since it produces synthetics with features similar to the observations in Figure 4.1.

4.3.2 Metastable Structures

If the intrinsic density $\Delta\rho_{ch}$ is depth-dependent and changes with depth faster than the thermal density ($\Delta\rho_{th}$), it is possible to generate metastable structures as displayed in Figure 2.2 and Figure 4.9a. The V_p and V_s images are predictions from a material with a larger bulk modulus (6%) than the ambient mantle and higher zero pressure density (2.25%) (Chapter 2) [*Tan and Gurnis*, 2005]. The layer forms a single dynamic structure with a

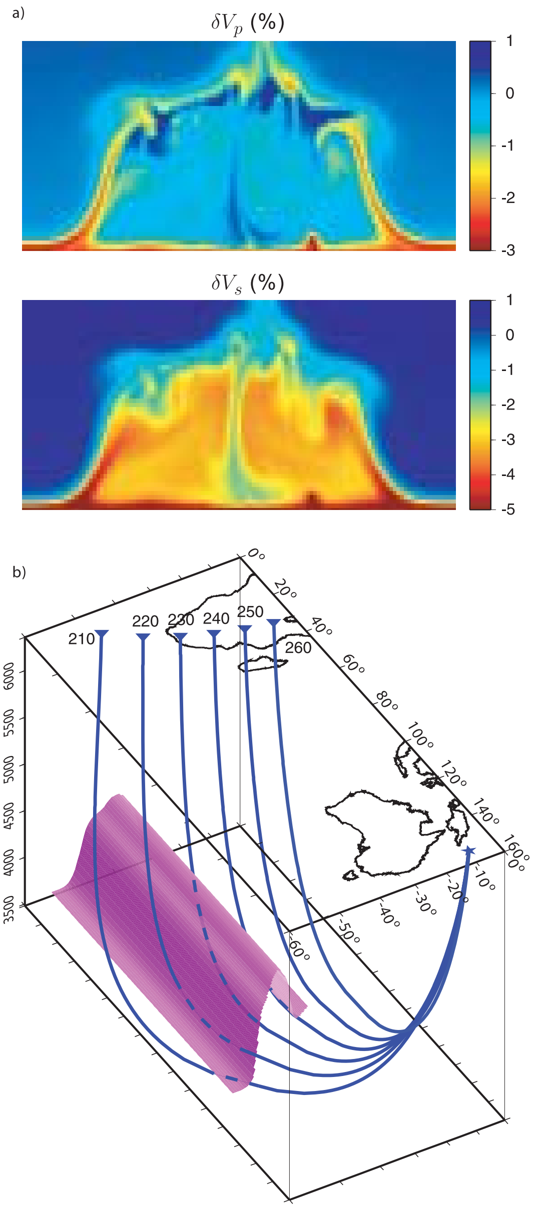

Figure 4.9: (a) 2D section through a metastable thermo-chemical structure with δV_p and δV_s. The average percentage drop is 3% for V_s and less than 1% for V_p. The structure is 1000 km high and 1500 km wide. Note the plumes along the edges which are wider and shifted internally for S relative to P, see *Tan and Gurnis* [2005] and Chapter 2. (b) Ray paths traveling from a source beneath Fiji-Tonga to an imaginary array (triangles) at various azimuths but constant distance (fan-shot) encountering a 3D structure containing 2D slices of metastable Superdome model represented by the purple ridge. The ridge structure is aligned roughly with the northern edge as given in Figure 4.1. We assume the ends are truncated as displayed, and obviously represent a greatly simplified structure. Paths at 250° and 210° miss the structure and are PREM-like.

nearly neutral average density. Note the plumes along the edges and the down-welling near the middle. The parameters chosen in this particular model were an attempt to explain a simplified 2D structure beneath South Africa, proposed by Ni and Helmberger [2003 a,b,c] and Wang and Wen [2007]. Sun et al. [2007a] inserted this structure into tomographic models and validated its usefulness in explaining 2D seismic waveform data. The model in Figure 2.2 predicts more complexity at the edges than embedded in the simple block structure by Ni et al. [2005] and looks more like that proposed by Wang and Wen [2007]. However, the small scale convection inside the structure changes with time and its 3D structure is probably extremely complicated since it must be influenced by the large scale convection produced by global 3D plate history. Such structures are presently being investigated [*Bunge et al.*, 2003]. Here we produce a 3D structure by extending the 2D metastable Superdome model (Figure 2.2d and Figure 4.9a) into an elongated structure with truncated ends (Figure 4.9b). The 3D synthetics for a "fan shot" are calculated for both S_{diff} (Figure 4.10a) and P_{diff} (Figure 4.10d). The synthetics are generated with the DWKM code discussed above. Partial responses are given in Figure 4.10b and 10c. For S_{diff}, the waveforms are strongly distorted when the rays travel across the boundaries (around 222^o and 239^o). Note the simplicity of P_{diff} relative to S_{diff} as expected from the 2D velocity sections, since the velocity anomaly is relatively small in Figure 4.10a for (δV_p) relative to δV_s. The components (Figure 4.11b and Figure 4.11c) suggest that the complex waveforms are caused by the large differential times between branches sampling the various paths as in the earlier examples. The longer the period, the greater the reach, and at long enough periods the structure disappears. Obviously, the shorter periods are the most useful in defining the edges so that working at the shortest periods possible is the most diagnostic.

Figure 4.10e displays the MPD analysis for S-waves and although it neglects the longer period diffractions, it captures the essential edge structure. A more detailed description of the timing measurements is given in Figure 4.11 for both the P and S-waves. First, we measure Δ_{LR} the shift parameter (Figure 4.11a) and its spacial gradient given in Figure Figure 4.11b. The two zones of interference are especially strong in S but with some evidence in P. This is apparently caused by the reduced P-velocity along the edges of the

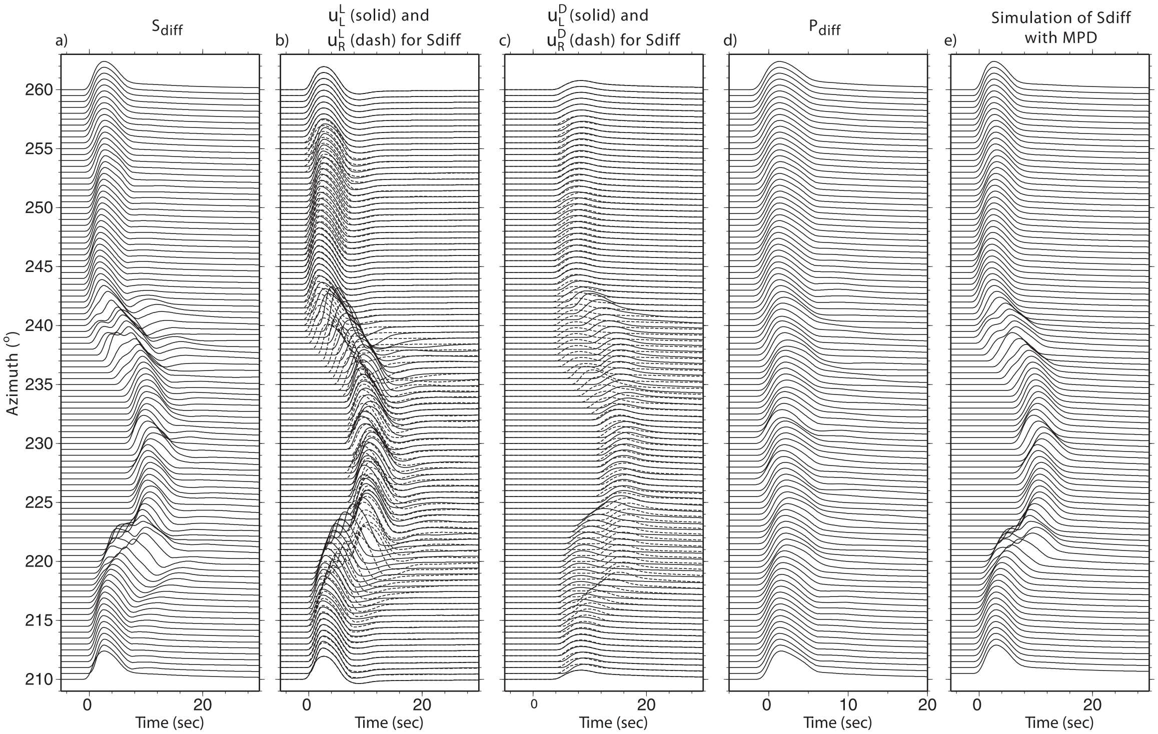

Figure 4.10: Construction of approximate 3D synthetics for S_d at constant distance (Δ = 110°) is given in (a). (b) and (c) display the "lit" and "diffracted" contributions. d) displays P_d which is much less dramatic but also sensitive to internal structure. (e) contains a simulation by simple construction with MPD discussed in the text.

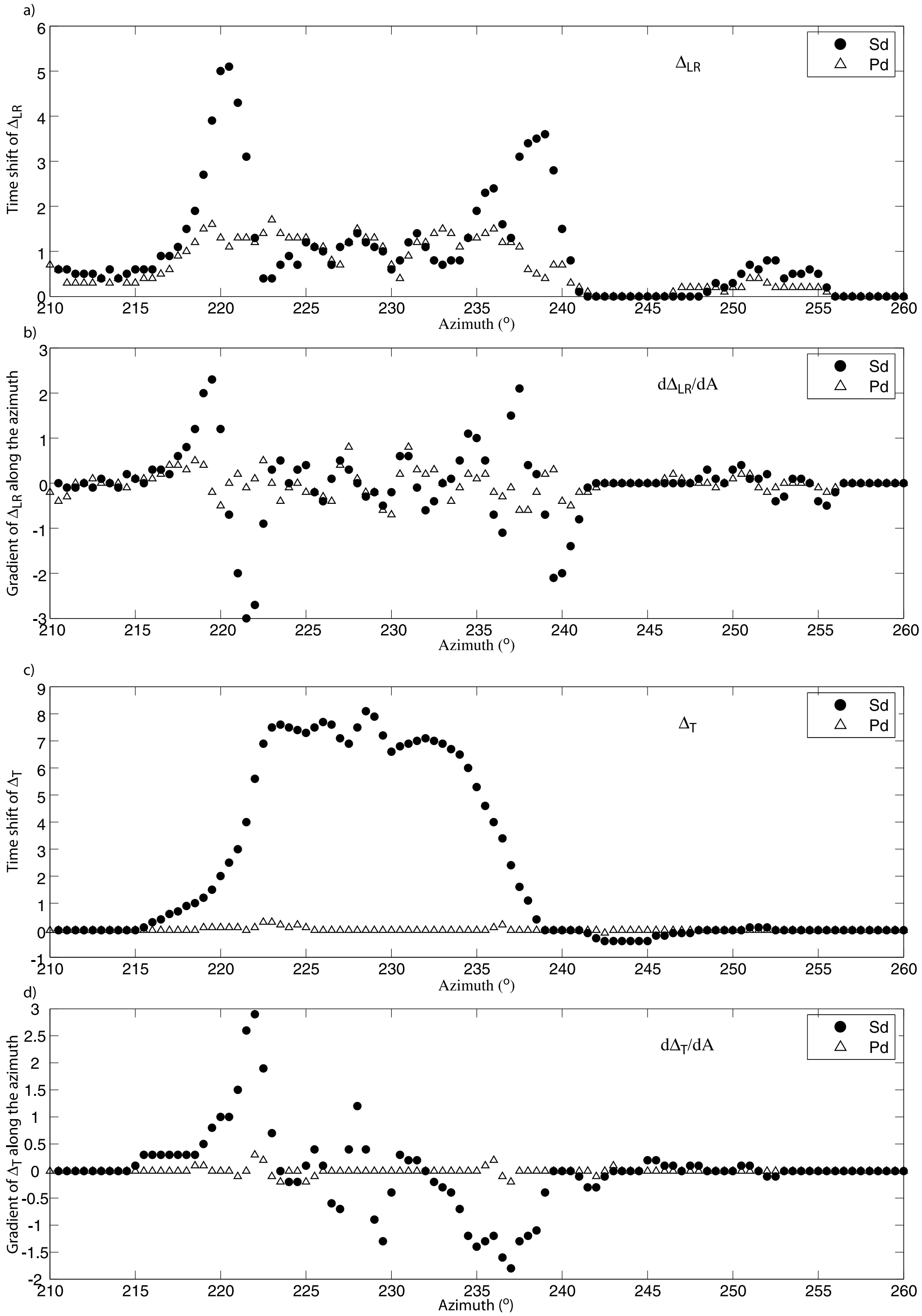

Figure 4.11: Presentation of timing delays and their azimuthal derivatives (d/dA). (a) Timing shift between the left side relative to the right (Δ_{LR}) and (b) derivative of Δ_{LR} ($d\Delta_{LR}$ /dA). The total shift of each trace relative to the reference model (PREM) and the derivative are presented in (c) and (d).

Superdome (Figure 4.10) and the fine-structure variation along the bottom. In the second step, the output of the MPD is cross-correlated with the synthetics (data) in Figure 4.10a to determine Δ_T (Figure 4.11c). There appears to be very little variation in Δ_T for P-waves, whereas the S-variation is more apparent, especially for the narrow down-welling zone. Even though these features are complicated, they are likely to be simplified compared to the real African Superdome. However, we can examine existing array data searching for diagnostic patterns as predicted above.

4.4 Application

Although there are many complex record sections sampling the edges of the African Superdome, we have chosen data from events A and B discussed earlier and that display particularly interesting features to demonstrate the usefulness of the MPD processing. The geometry is displayed in Figure 4.1 where the great circle paths are arriving at the array sampling the Superdome beneath the Indian Ocean.

4.4.1 Northern Edge (Event A)

We first determine or define an empirical source function, S(t), which is the simplest waveform or wave train in the array, as found from a cross-correlation search. Next, we generate a synthetic for a reference model (such as PREM) using this S(t) as $\dot{D}$(t) in Equation (4.11) and assume each recording can be modeled by summing S(t)/2 + S(t + Δ_{LR})/2. We define Δ_{LR} as the time separation which refers to the lag of the right half of the Fresnel Zone relative to the left, or split time as discussed above. The data and simulation is given in Figure 4.12a where the multi-pathing is recovered. Next, we correlate the simulated trace (MPD) with observations to determine Δ_T as in the numerical tests. The shifts required in this analysis are given in Figure 4.12b along with individual ray paths and their associated time delays. The top panel displays the overall travel time delays showing the slowdown of the wavefront as it samples the boundary. Note that these plots are independent of how the original data was plotted as in Figure 4.1. The multi-pathing shifts, $\Delta_{LR,}$ are given in the bottom panel of Figure 4.12b and produce a rather simple picture

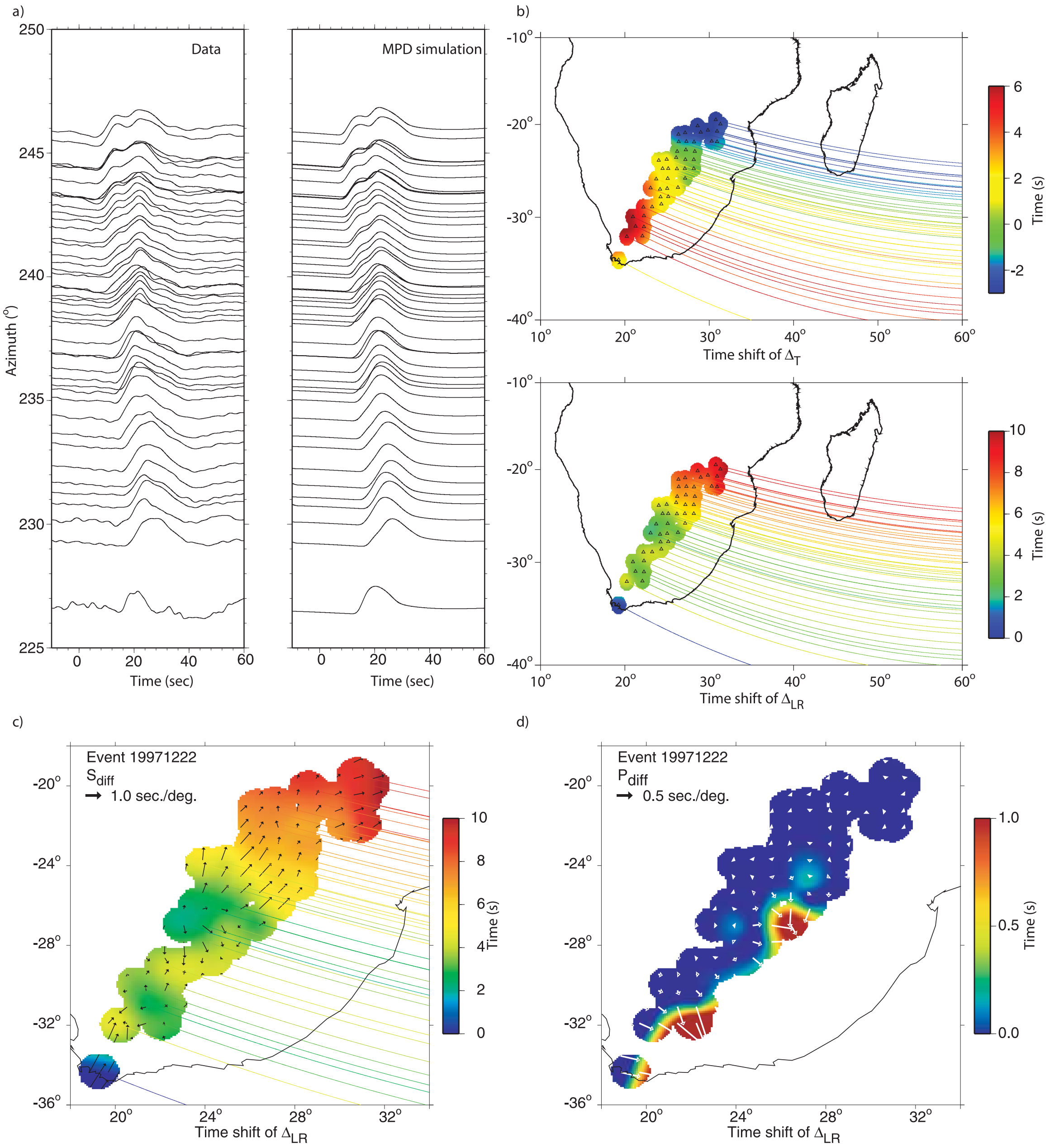

Figure 4.12: The observations for event A (19971222) in Figure 4.1 along with the MPD results are presented in (a) with their travel time shifts in (b). The blue paths are fast relative to the red paths. The differential shifts (Δ_{LR}) reach 10s offsets near the top. (c) and (d) display the detailed comparison between the P and S results.

from northeast-to-southwest.

A more complete picture is obtained by plotting the gradient, Figure 4.12c. This pattern is more complex with some patches showing strong out-of-plane effects (longest arrows) perpendicular with the radial direction and some indicating in-plane effects. It appears the wall was never actually crossed or perhaps there are two steps with one associated with the green to pink zone and another to the north. Such complexity in 2D has been addressed by Wang and Wen [2007]. However, the P-wave data shows few signs of multi-pathing as discussed earlier, with some complexity given in Figure 4.12d, which look more like small ULVZs. The southern edge displays more P-wave distortions as discussed next.

4.4.2 Southern Edge (Event C)

The waveform data are presented in three frequency bands as given in the top panel of Figure 4.13 as broadband, and low pass filtered to 5s and 10s. The upper traces and bottom traces have relatively simple waveforms, but are offset by about 15s representing the anomalous S-velocity structure. The edge is well sampled between 215° and 210°, with a small diffraction wing indicated by a dotted-line. Note that at long periods, the edge becomes less obvious as expected, however, the MPD still measures the pulse broadening as displayed in the lower panel of Figure 4.13. We have included the cross-correlation (cc) values averaged over the complete profiles which become slightly higher as the short-periods are removed, although the fits are excellent.

In the broadband waveforms (Figure 4.13a), the source duration is short enough to allow the O_D operators to be distinct near 213° in azimuths producing multiple peaks. These features are not observed when filtered to longer periods. However, the characteristics of the multi-pathing delays are generally maintained as demonstrated in Figure 4.14. Here we display the results in three columns indicating that the delays of Δ_T are nearly the same (upper row in Figure 4.14). The gradient results are presented in the bottom panel where the data showing the strongest azimuthal features remains clear at all frequencies. Note the reversal in arrows near the top of the plots. Based on the training exercises we interpret this as a wall-crossing with nearly all of the variation being in azimuth. The multi-pathing arrows flip sign uniformly along the zero-line with stations to

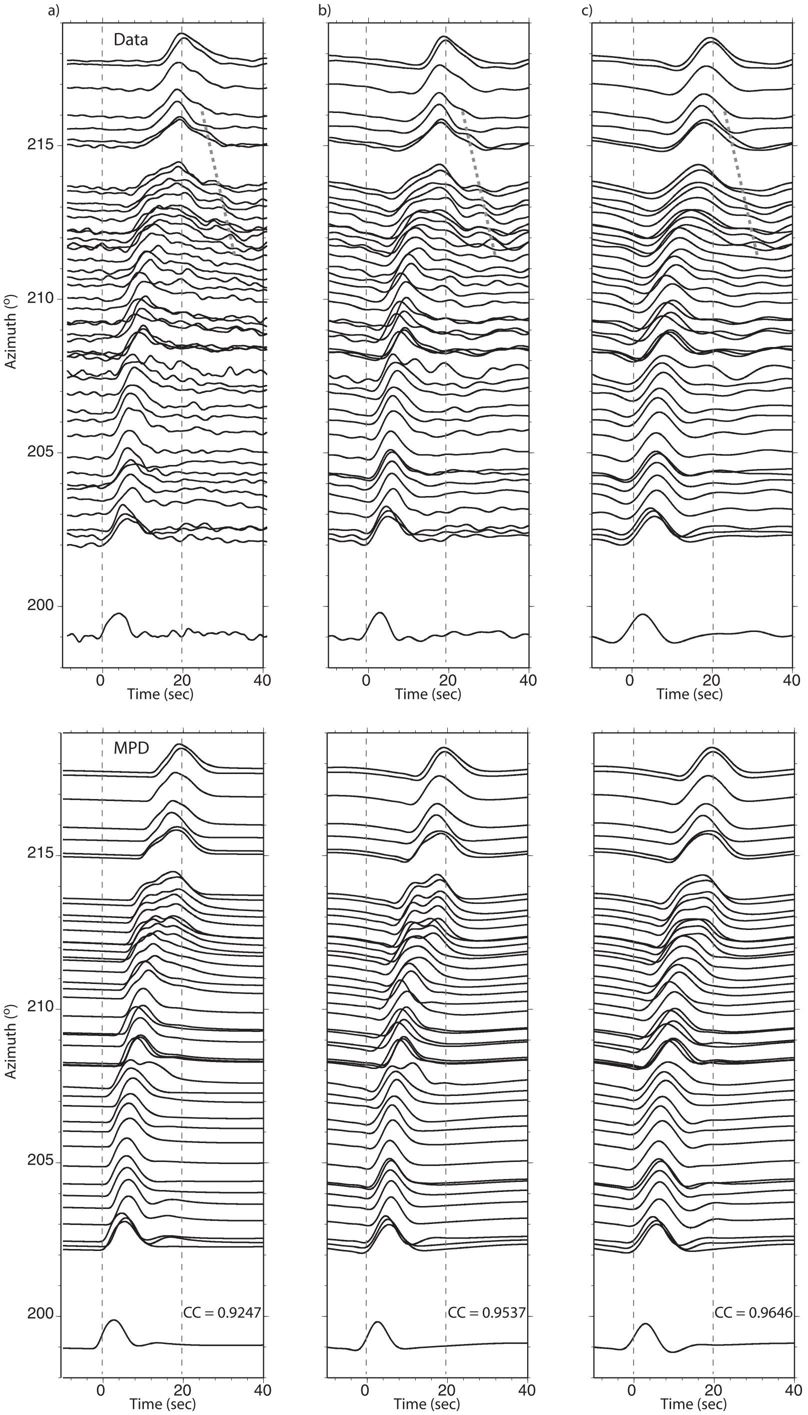

Figure 4.13: Application of the MPD analyses to event C (970904) (paths in Figure 4.1) as a function of frequency with (a) broadband (BB), filtered to (b) longer than 5s and (c) longer than 10s. The upper panels contain the data with the MPD results given in the lower panels. Note that the fits remain high even at BB periods, with cross correlation coefficient of ~ 0.93.

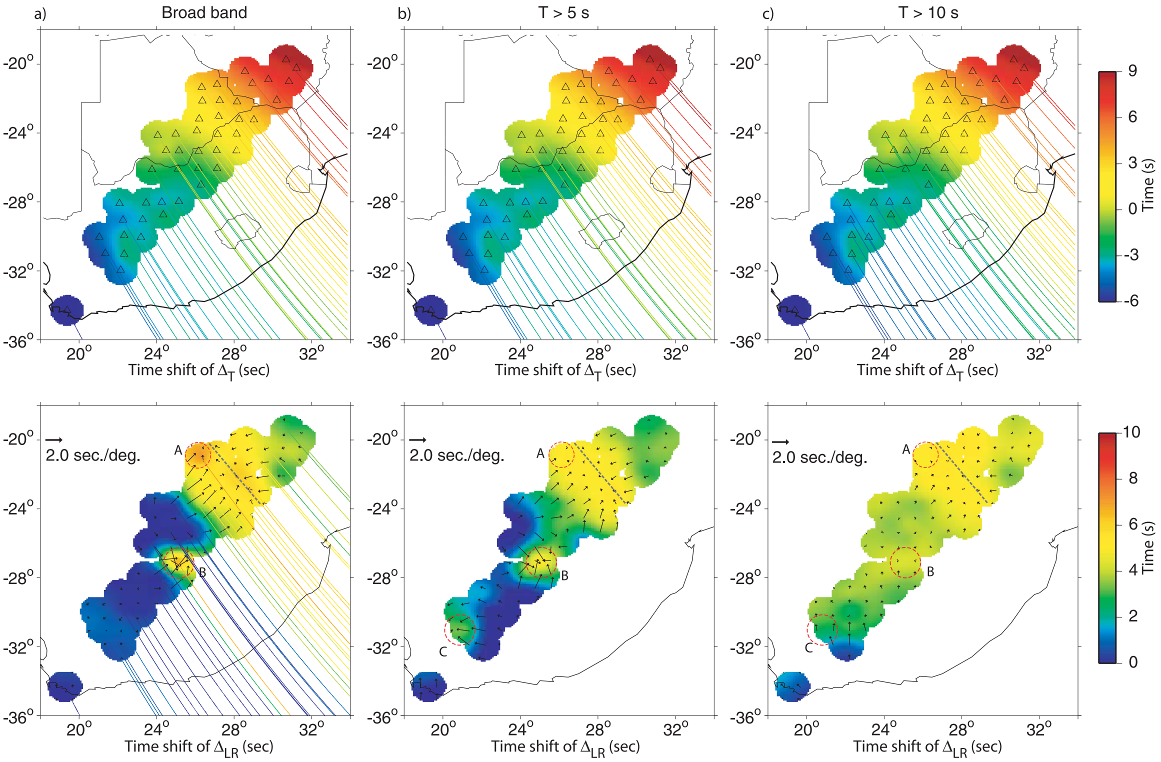

Figure 4.14: Delay time results for data (S_d) in Figure 4.13 with different frequency bands are presented for Δ_T in the top row and Δ_{LR} in the bottom row. We have included the gradient of Δ_{LR} as arrows which display the wall-crossing position indicated by the heavy dashed line. Some small-scale structures occur near the wall (circle A) and to the west (circle B) which have the footprint of ULVZs.

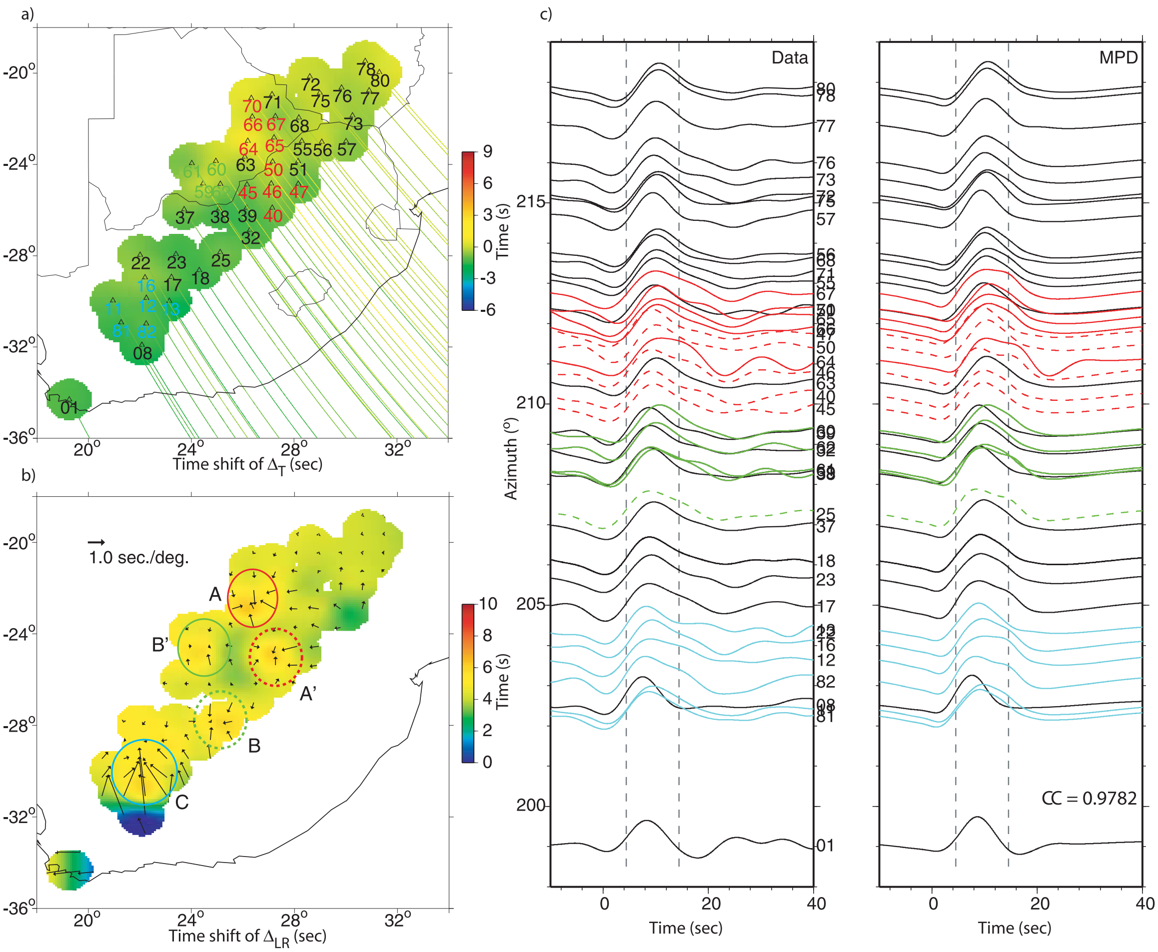

Figure 4.15: Delay time results for P_d (event C) are displayed in (a) and (b). (c) Comparison of P_d observations and MPD simulations. Note that the strong wall signature apparent in S results (Figure 4.14) is nearly absent in P results. Some local or small-scale features with circular patterns are displayed at position A (relatively strong in red), B (weak in dashed blue), and C near the southern edge of the array. We have included some timing lines to help identify a small delay at the top, which is seen in (a) as a slight change in color.

the north pointing south while stations to the south point in a northerly direction. The strength of this multi-pathing requires a segment of the structure to be nearly aligned with the ray-paths such that paths to the south are about 8 s faster than to the north. Note the gradients are large, over 2 s/deg. Some smaller features can be seen in the broadband results labeled A, B, and C. In these images, the multi-pathing is in both azimuthal and radial directions and appears to be small in dimension. Perhaps this small structure along the edge is of the type presented in the metastable model, associated with up-welling. The other two zones are more difficult to interpret but could be similar to the small-scale structures further to the south.

The above small-scale anomalies appear to be also observed in the P-wave analysis as presented in Figure 4.15. The data is plotted relative to PREM and a small timing shift with distance is apparent, with the traces near the bottom arriving slightly early. This feature can be seen in the Δ_T results indicating about a 1.5s delay. These smaller scale features occur in both azimuth and distance, which is more indicative of a D″ feature, perhaps associated with ultra-low velocity zones near the Superdome edges. Unfortunately, the P-waves contain considerable noise which means more events need to be analyzed to confirm the existence of these small-scale features. In contrast, there appears to be little evidence for the wall-defining features in P, a result compatible with the Metastable Superdome interpretation discussed earlier.

4.4.3 A narrow mid-mantle plume below Southern Africa

The resolution of global tomographic models, which have increased through additional data while accounting for the finite frequency of seismic waves, have provided more details on possible plumes in the lower and upper mantle [*Montelli et al.*, 2004; 2006]. Although some of these features have small cylindrical forms, most are broad, especially at the base of the mantle, where they are commonly referred to as Large Low Shear Velocity Provinces (LLSVP, Figure 4.16a). Beneath the mid-Pacific and South Africa are structures we refer to as superdomes because of their large size while appearing rounded on top. Images show considerable differences between these structures but the change of scale from about 1000 km in the lower mantle to a few hundred in the mid-

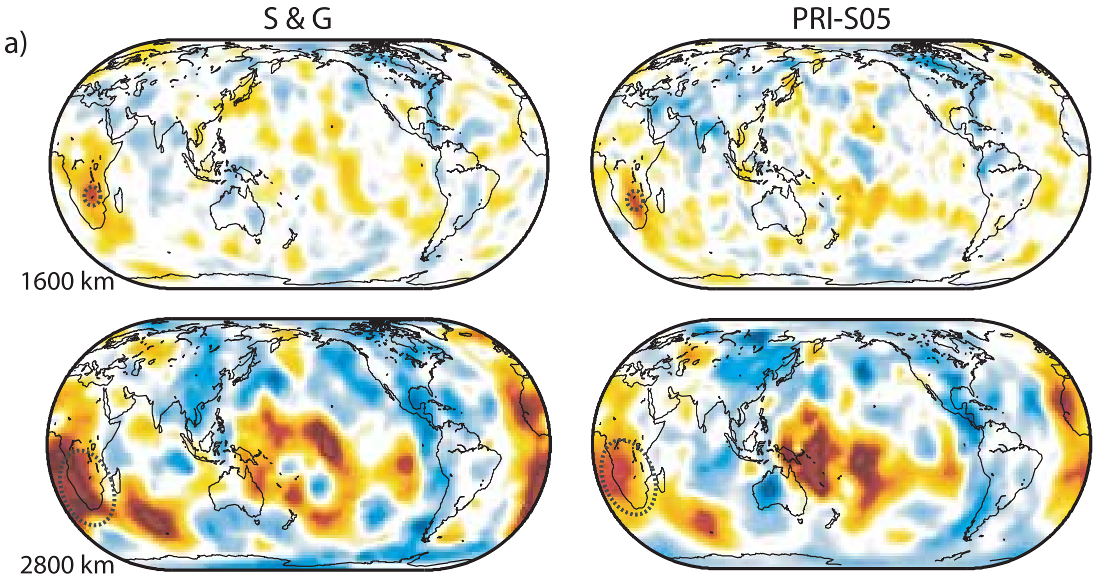

b) Metastable Superdome

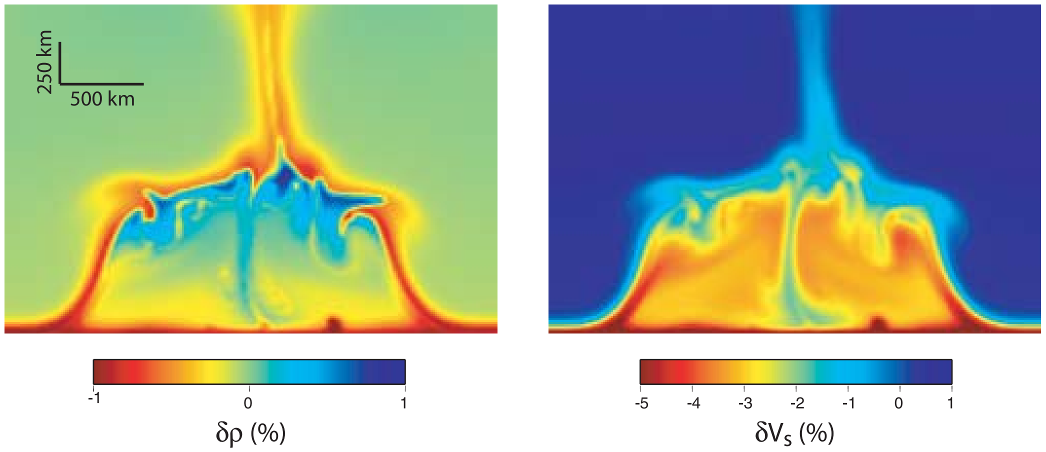

Figure 4.16: A comparison of global tomographic images; (a) at the lower mantle with a predicted cross section, (b) of seismic properties from a meta-stable thermo-chemical structure. The anomalous material has a larger bulk modulus (6% above the ambient) and higher density (2.25%). The S&G shear velocity (left) variations (± 3%, blue and red) are from *Grand* [2002] and the PRI-S05 shear velocity (right) is from *Montelli et al.* [2006]. The agreement between these two models is remarkable considering the complete independence of data and methodology used [*Helmberger et al.*, 2005]. We interpret the broad base in the data at the CMB (Africa) to be a large-scale chemical pile and the upper small dimension feature to be a plume.

mantle is a common feature of nearly all seismic inversions.

In Chapter 2, the high bulk modulus model is introduced to explain the African Superdome. The model gives sharp vertical sides with the apparent long term stability of the African Superdome [*Helmberger and Ni*, 2005b; *Masters et al.*, 2000]. Particularly in that model (Figure 4.16b), a narrow plume emerges from the top with a small amount of entrainment of the high bulk modulus mantle.

Although we have used data in Figure 4.12 and Figure 4.14 to establish the sharpness of the wall, the Sd phases are not not ideal for detailed study because of lack of knowledge about the structure beneath the Indian Ocean [*Wang and Wen*, 2007]. A better geometry is provided by the SKS paths sampling the mostly 2D structure from the west over a 10° by 20° region forming a relatively dense sample (Figure 4.17). Although these small crustal events along the East Pacific-Rise (EPR) have complicated wave trains they remain stable in the MPD. The four EPR events were processed in this manner (Figure 1, Appendix A).

The combined Δ_T delays are plotted with respect to CMB exit points (Figure 4.18a), normalized by a constant time shift for all stations per event. Such baseline shifts are common because of uncertainties in the event origin time and location. However, the relative timing among the stations is maintained. Delays of up to 6s are obtained with the four events producing compatible results. The paths overlay with some crossing paths indicated by the arrows in Figure 4.18a. The splitting analysis is summarized in Figure 4.18a (right) where a serious distortion of waveforms occurs along the southern edge (-45°N15°E). Unfortunately, the details are unclear because of the noisy complex arrivals as well as limitations in data coverage. This location has been studied previously with ScS-S analysis where they suggest a strong ultra low velocity-zone [*Simmons and Grand*, 2002; *Wang and Wen*, 2007; *Wen et al.*, 2001], which may correlated with the slow velocity edge structure in the high bulk modulus model (Figure 4.16b).

Because of SKS relatively steep ray paths, their spatial pattern proves highly effective in mapping horizontal structure. Thus, we will assume that these patterns in Figure 4.18a are controlled entirely by velocity variation along these SKS paths. Furthermore, we will assume that paths inside the structure encounter a -3% reduction in velocity [*Sun et al.*, 2007a]. This is a simplification but allows a structural image to be formed by performing a SKS tomographic projection on Figure 4.18a upward to define the height. A plume feature is added to the 2D profile based on the circular red pattern (Figure 4.18a) located along the upper dotted line near the top of the dome to fit the Δ_{LR} delay. The observations producing this pattern have late arriving energy, roughly delayed by 2 to 3s. These late arriving ray paths are sampling the interior of a plume and are not often sampled directly since energy from the exterior always arrives first, at least in the synthetic models when the radius is less than 100 km. The fattening of observed pulses is clearly seen in the raw seismograms (Figure 1, Appendix A). This type of observation seems to be a direct measure of the existence of a plume. We constructed synthetics from structures with circular plumes arising from the superdome, each with a different radii, by repeating the MPD analysis on artificial data (Figure 4.18b–d). A sample of waveforms is given in Figure 4.19 with the MPD timing results displayed in Figure 4.18 b–d which can be compared directly with the pattern given in Figure 4.18a. Note that this pattern is back projected from the surface along SKS paths to the CMB. Thus, the pattern shifts northeastward for shallower mantle depths as indicated by the circles in Δ_{LR} of Figure 4.18a. Both the S-velocity of Grand [2002] and S-velocity of Montelli et al. [2006] predict this behavior although the P-velocity results suggests some bifurcation at shallower depths [*Montelli et al.*, 2006].

The seismic results for the African structure suggest that a narrow low velocity, generally cylindrical anomaly overlies a broad-scale low velocity structure. The overlying narrow structure is probably smaller than about 150 km across (Figure 4.18). If the structure is greater than 300 km across, we predict that the width of Δ_{LR} anomaly is about 500 km with a strongly localized Δ_T, neither of which is consistent with the observations. The region of strongly localized Δ_T in Figure 4.18d is presented as delayed SKS arrival with no obvious waveform complexity (case with plume radius of 250 km in Figure 4.19), which is not indicated by the data. Although we have constraints on only the basal region of one putative plume, it would appear that lower mantle plumes are quite narrow, probably less than 100 km in radius, in general agreement with geodynamical suggestions [*Griffiths and Campbell*, 1991; *Loper and Stacey*, 1983]. Our result is in contrast with Montelli et al.

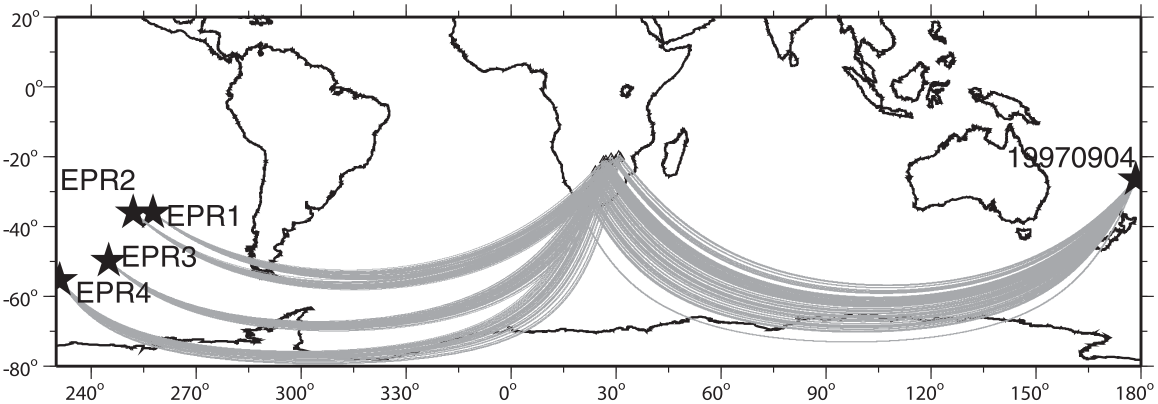

Figure 4.17: Presentation of geometry involving the position of the Kaapvaal array in South Africa, earthquake sources beneath the Pacific and East Pacific Rise (EPR)

Figure 4.18: Composite waveform information from four EPR events compared to corresponding MPD analysis from various plume models. The delay Δ_T and differential values Δ_{LR} are migrated down to the CMB and plotted in map form for various events in (a). Two heavy lines are added to indicate the bottom and top of the superdome where the SKS travel time delays climb to 6 s. Note the blue circle of vectors near the South tip of Africa with radius of 1°. Three sets of simulations are displayed with circular shaped plume (b–d) emitting from the top of the Superdome (Figure 4.19). As the radius of the plume grows, a small zone of delayed Δ_T (dark red on the left) occurs because the wavefield begins to resolve the interior directly which is not in the observations. The small circle indicating the plume position at the CMB in (a) migrate to the northwest for midmantle positions displayed at depths of 1900 km (red circle) and 1400 km (black circle).

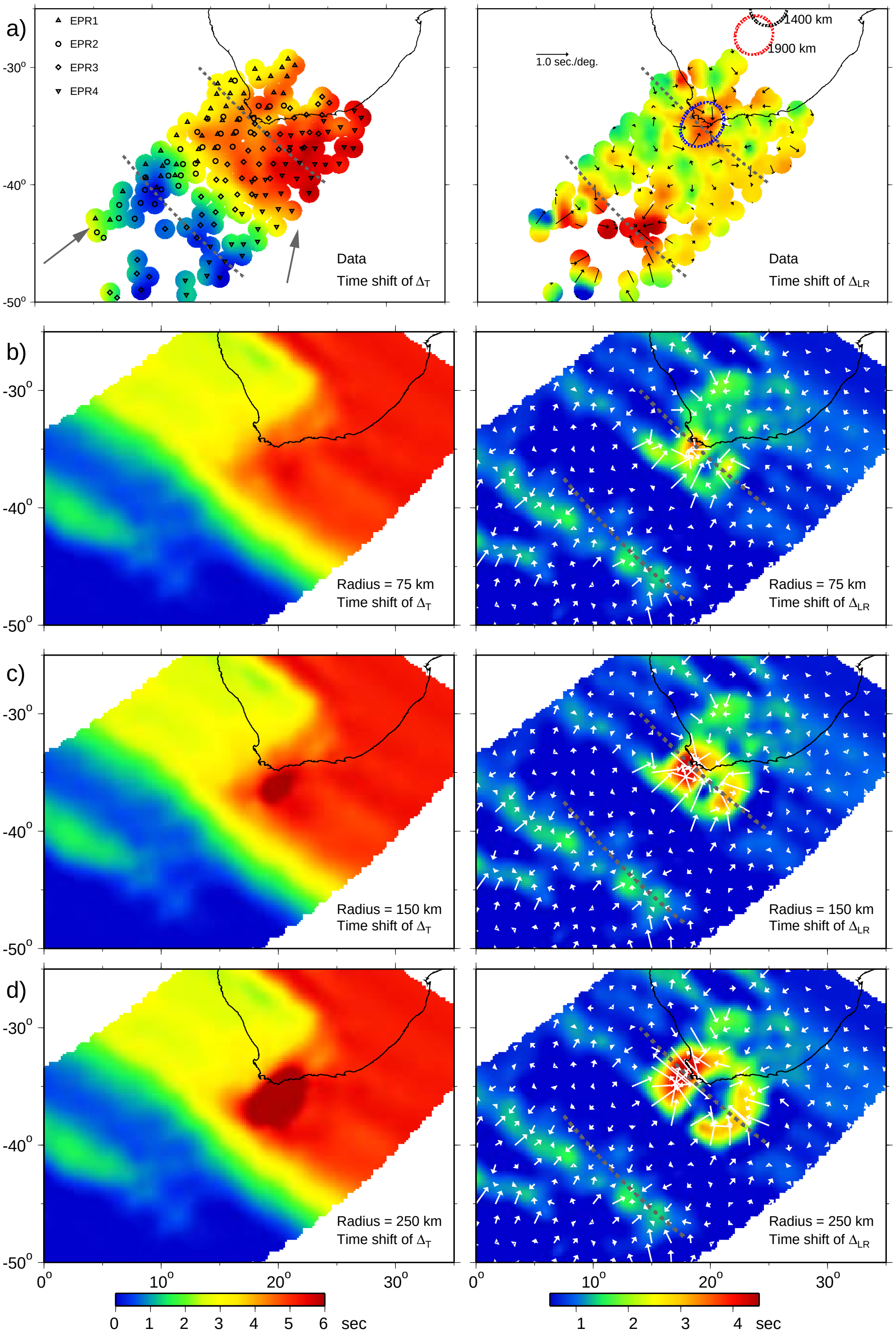
a)
EPR1
EPR2
EPR3
EPR4
Data
Time shift of Δ_T
1400 km
1900 km
1.0 sec./deg.
Data
Time shift of Δ_{LR}
b)
Radius = 75 km
Time shift of Δ_T
Radius = 75 km
Time shift of Δ_{LR}
c)
Radius = 150 km
Time shift of Δ_T
Radius = 150 km
Time shift of Δ_{LR}
d)
Radius = 250 km
Time shift of Δ_T
Radius = 250 km
Time shift of Δ_{LR}
-30°
-40°
-50°
0°
10°
20°
30°
0
1
2
3
4
5
6
sec
1
2
3
4
sec

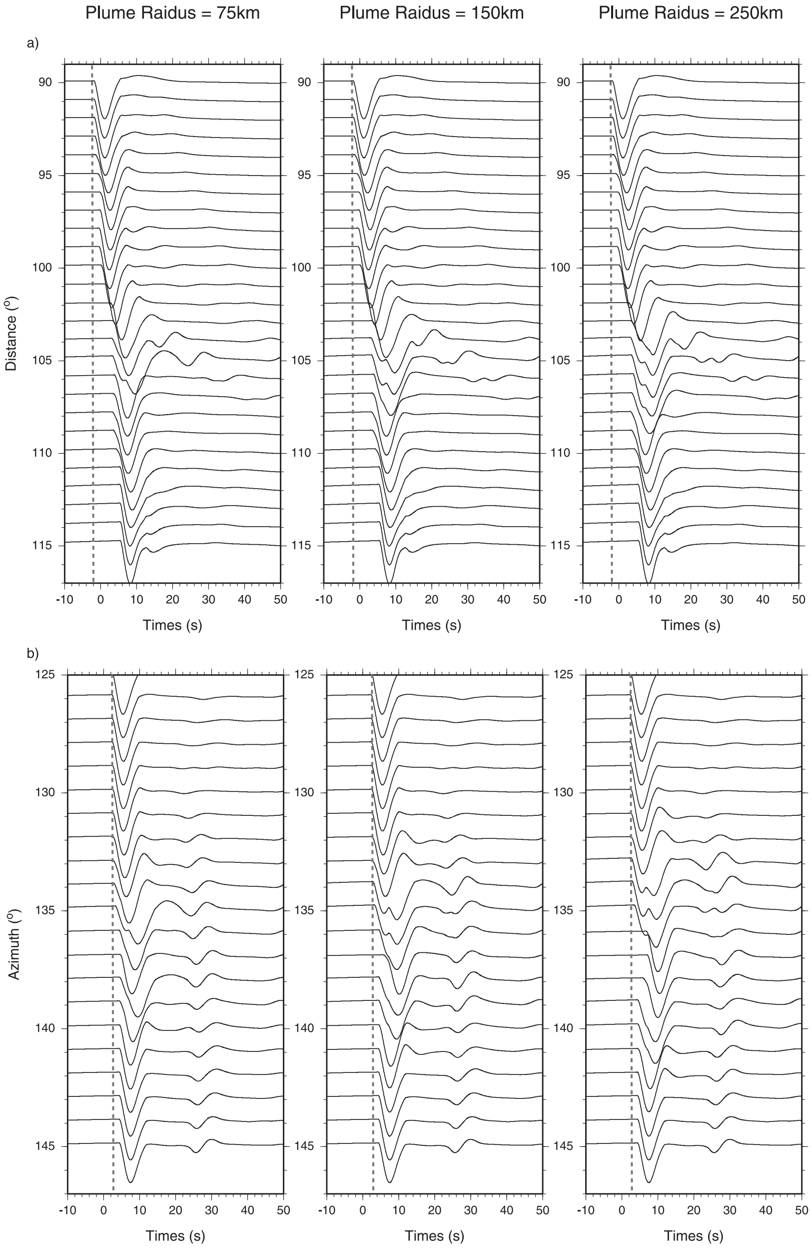

Figure 4.19: 3D synthetics for thin (75 km) to thick (250 km) plumes. Although the MPD maps used a large number of synthetics, we present crossing lines centered on the plume, one (a) in the plane plotted in distance with azimuth of 135° and one as an azimuthal profile (b) for a distance of 105°. Note the time delay (Δ_T) becomes obvious as the radius grows, but it proves difficult to grid SEM for smooth conduits.

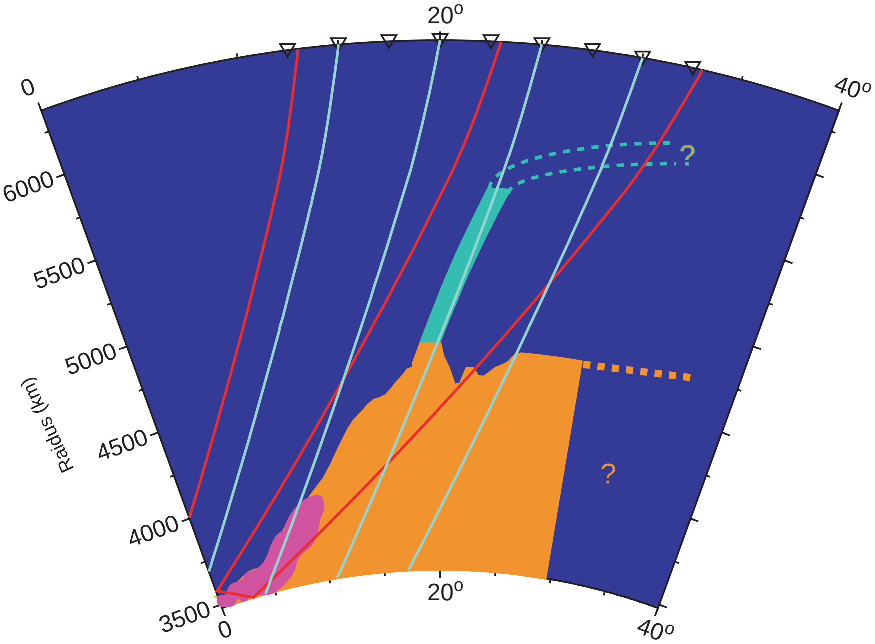

Figure 4.20: A 2D cross-section sampling the plume is displayed idealized with an uniform reduction of 3% inside the superdome (yellow), a 1.5% drop inside the plume (green), which extends about 1000 km into the top part of the lower mantle. A pink zone is added at the edge although not actually modeled because of noisy data but at the proper position. The model looks very much like the models presented in Figure 4.16a with a broad base and a pipe-like feature extending upward towards the north.

[2006] from finite frequency tomography, suggesting a range of widths from 200 to 800 km. Large widths are consistent with only a small viscosity between the plume and mantle rising in the plume [*Olson and Singer*, 1985] or thermo-chemical structures—both favor wide-blunt plumes.

A 2D section of our preferred model crossing through the plume is given in Figure 4.20, where we have assumed the velocity reduction inside the plume is 1.5%. Its height trade-offs with this value because only the timing delay $\Delta_{LR} \sim 3$s is defined by the data. We assumed this value to be compatible with estimates obtained by the high bulk modulus model given in Figure 4.16b, while also being in agreement with tomographic estimates. Two dynamic models have been proposed to explain the LLSVPs, the high bulk modulus model [*Tan and Gurnis*, 2005; 2007] and the chemical pile model [*McNamara and Zhong*, 2004; 2005]. The former has steeper sides (~70°) while the latter one has gentle slopes (~30°). Our results are in the middle (50°~60°). Both MPD images and multi-pathing in SS phase (Figure 2, Appendix A) suggest a rough top of the superdome, which is more profound in high bulk modulus model. In this report, we only covered the southern edge and more data are needed to complete the entire image, which will greatly help to define the dynamics of the system.

4.5 Discussion

Travel time tomography has been one of the main tools in studying Earth structure. Standard practices for geodynamists are to convert these velocity anomalies into density and temperature and infer geophysical observables such as topography and gravity. However, tomographic models produced by smooth, damper inversions underestimate the sharpness of structures. To emphasis this point, we have generated 3D synthetics (Figure 4.21) for event A assuming the well developed model by Ritsema et al. [1999]. Generally only sparse stations are used in such tomographic studies and time-delays are minimized by adjusting locations and origin times. The array data, especially at the shorter periods, indicates the sharpness of such structures which are generally missed in long period studies. Fortunately, these tomographic studies do explain some of the delays and provide crucial information about the geometry of the structure causing these waveform distortions.

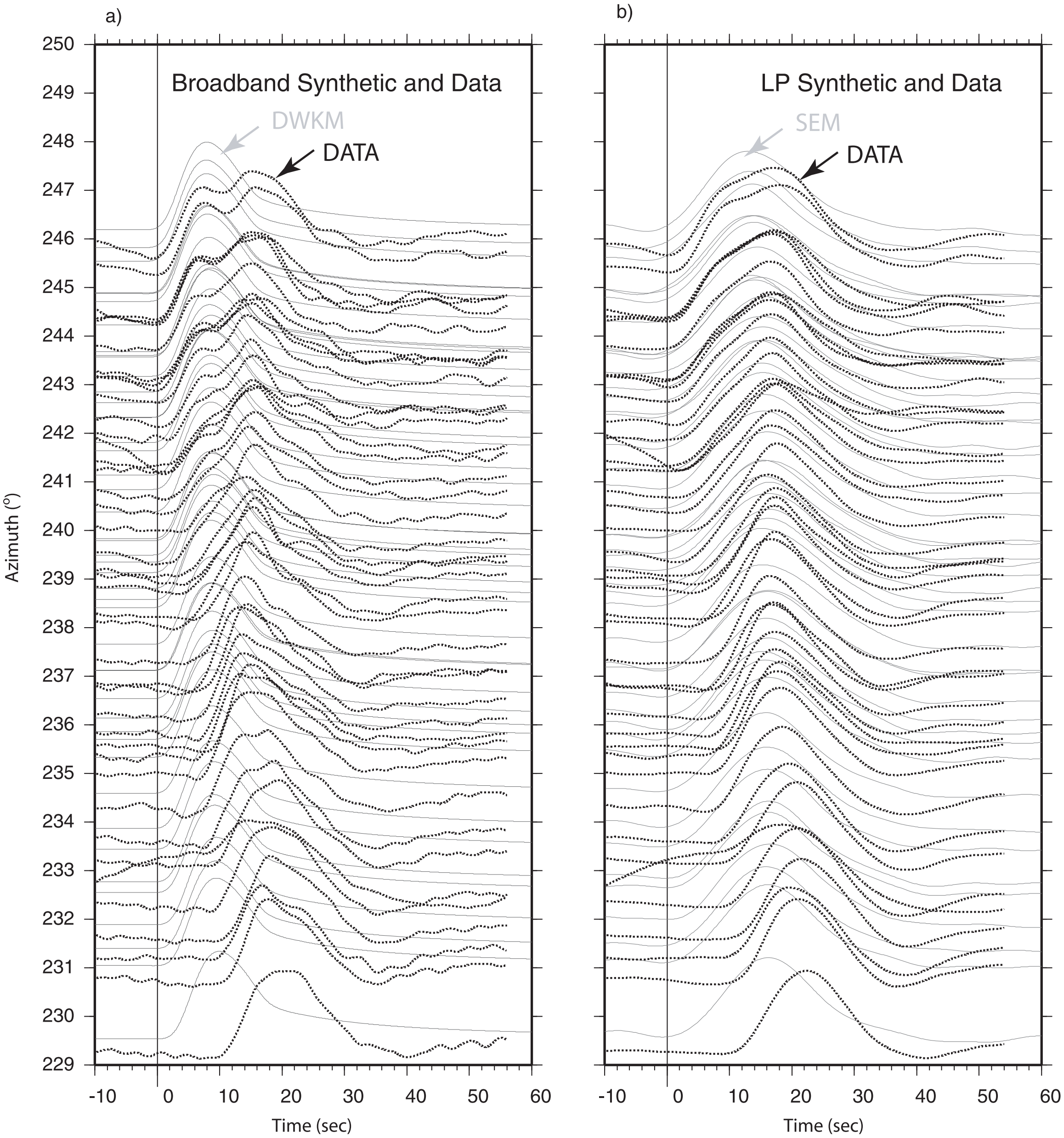

Figure 4.21: Direct comparison of synthetic predictions (solid traces) from Ritsema's tomographic model [*Ritsema et al.*, 1999] with observations (dotted). (a) Observations plotted in azimuth for event A against DWKM synthetics (broadband). (b) Long-period synthetics filtered to 18 sec generated by SEM with data. The synthetics show less than 4s delays which is too small to satisfy the data. Tomography models are generally too smooth to predict the multi-pathing observed here.

Simply enhancing the velocity anomalies and adding sharpness has been proven quite useful in generating models that predict improved synthetics fit to data for both regional data [*Song and Helmberger*, 2007] and lower mantle data [*Helmberger and Ni*, 2005a]. Another recent approach followed by Ritsema et al. [2007] is to examine a large class of models that satisfy the tomographic data but explain additional constraints. DWKM synthetics could then be generated and compared with data directly or use MPD to test for significance of sharp features. In this study, we have provided a new tool for examining the wavefield and providing guidance in how best to approach modification of tomographic results in terms of vertical vs. horizontal structure. Instead of forcing array data to produce pulses that cross-correlate well enough to obtain accurate travel time picks, we suggest using the broad-band wavefield to derive additional MPD-type parameters. From the footprint and timing gradient analysis for a single phase from a single event, we can only determine how sharp the anomaly it is and the orientation of the anomaly. To get exact location and size of the sharp anomaly, we need to combine the MPD parameters derived from different phases and different events. Using different phases for the same event, we can make some decision with respect to what features in the Earth are causing the multi-pathing effects. As discussed in Song and Helmberger [2007], shallow structure in the upper-mantle tends to disturb all phases from a particular azimuth, including P, PP, S and SS etc. If all the phases have strong multi-pathing effects, the sharp anomaly should exist at shallow depth, which affects all phases by the same degree. If strong multi-pathing only appears on those phases sampling the deep mantle (ScS, PcP), we can estimate that the origin of the anomaly is coming from the lower mantle. Figure 4.22 displays the MPD patterns for a Kuril Island event recorded by USArray. The difference patterns between S and ScS indicate anomalies occur not only in upper mantle but also in lower mantle, which is only sampled by ScS. On the other hand, MPD is useful to detect the sharp edges in the shallow structure as in Figure 4.23. The rays from different events sample the sharp anomaly differently and generate different MPD patterns. Those patterns can be migrated to different depths and find the coherent parts, which give the sharp boundary laterally. By connecting those boundaries at different depth, we can construct a 3D image of the sharp edges. Equation (4.7) shows that the radius of lit region changes with the depth of reference

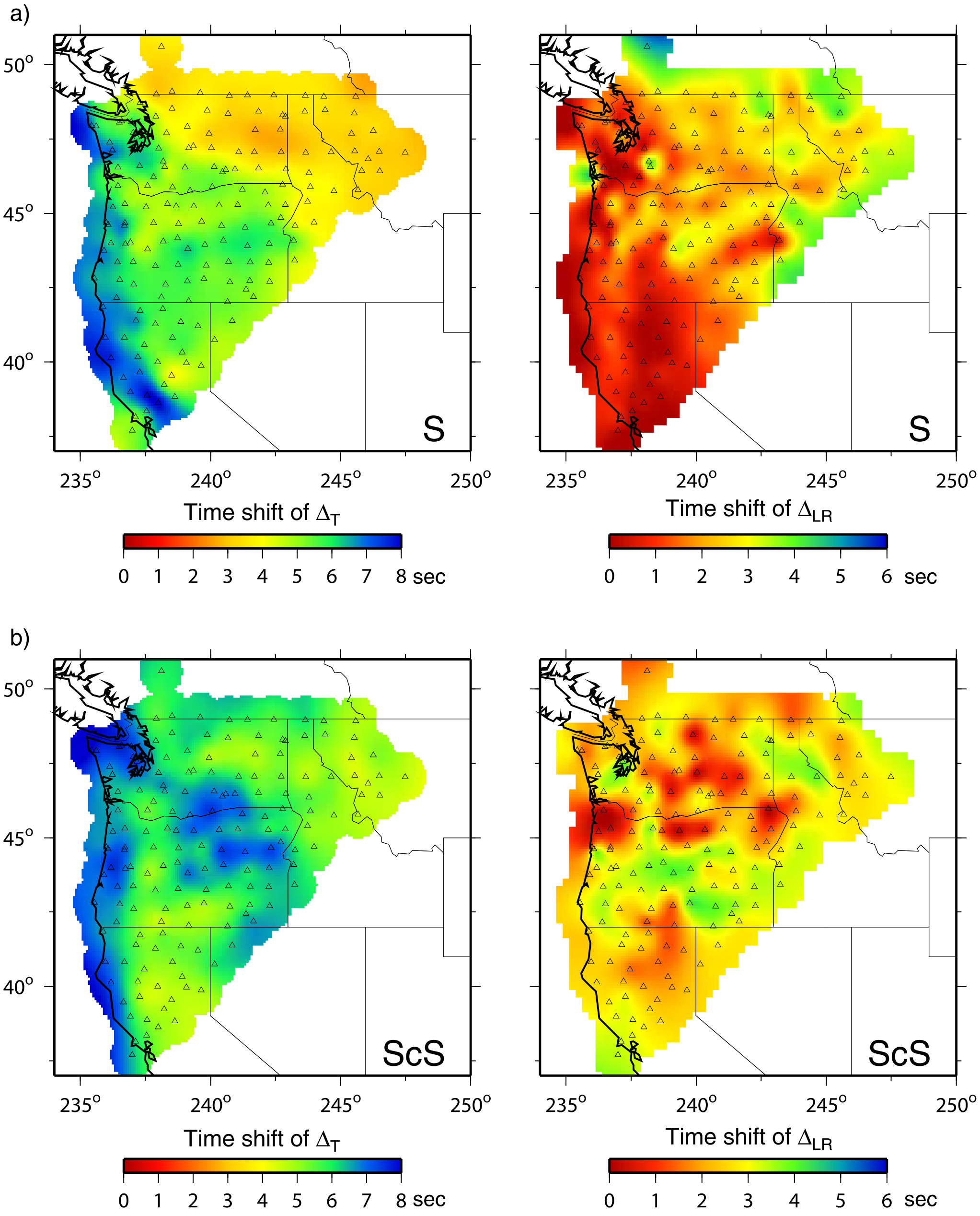

Figure 4.22: MPD patterns of a) S and b) ScS for a Kuril Island event (July 16, 2007)

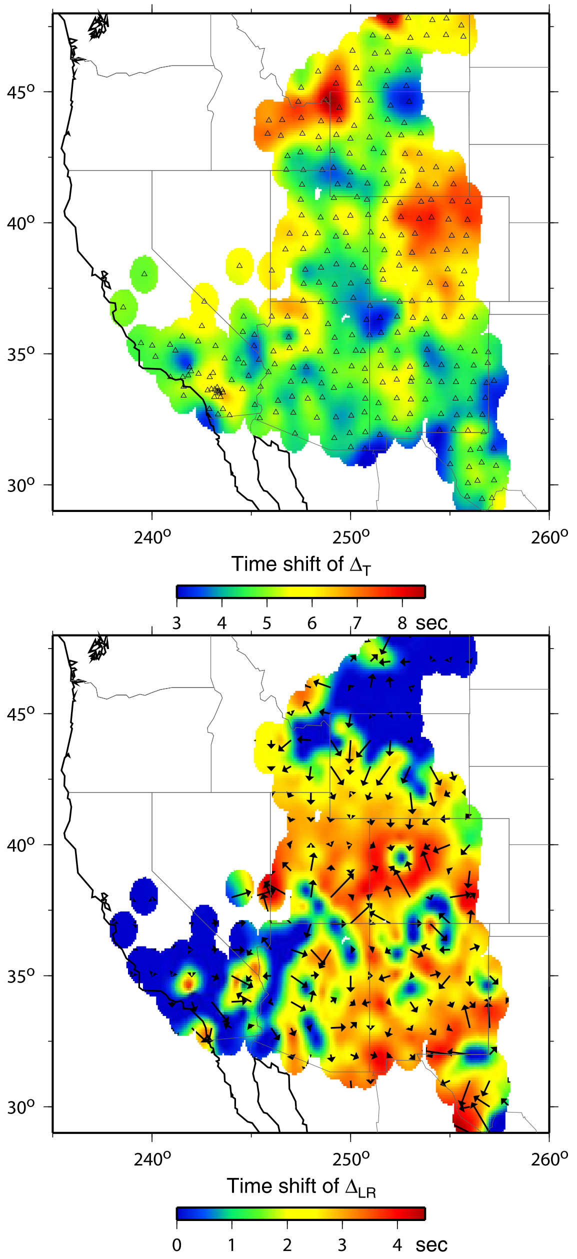

Figure 4.23: MPD patterns for a South American event (Oct 12, 2008). Note the large Δ_{LR} could be related to Aspen anomaly, Jemez lineament, etc.

plane. The deeper the reference plane, the wider the lit region. For an event station couple, a migrated Δ_{LR} image at certain depth is a circle centered at the ray piercing point at that depth with radius Δ_l. The value along the circle is Δ_{LR}. The summation of all migrated images for every event station couple will give a strong indication of sharp boundary if it arises at that depth. This technique is similar to that used in the finite-frequency tomography using adjoint methods, which the summation of finite-frequency sensitivity kernels defines the overall misfit kernel [*Tape et al.*, 2007]. We will discuss this migration method in future efforts.

Since temperature and chemistry affect the P and S velocities differently, studying P and S waveforms from the same events can provide unique detail into differential measures, i.e., $R=dlnV_s/dlnV_p$. This parameter is important in understanding the mineral physics in the deep mantle [*Masters et al.*, 2000]. An approximate value for R is $(V_s\delta t_s/V_p\delta t_p)$ where δt_s and δt_p are travel time perturbations [*Souriau and Woodhouse*, 1985]. Accurate estimates of the δt_s and δt_p are obtained from applying the above operators as displayed in Figure 4.15 for event C. In this case, the R factor is quite high, R>6, because the P-waves show very little change across the Superdome boundary. Generally, the P-waves encounter some delays when crossing the edges, as discussed earlier, and the average value found by Masters et al. [2000] of 3.8 for the Pacific and South African Structures appear to be generally compatible with our results which are somewhat higher. To estimate R, we average over samples inside the Superdome (top seven stations in Figure 4.14) for S-waves and for P-waves (Figure 4.15), where we normalize the Δ_T to the region most-like PREM (bottom six stations).

Then

$$R = \frac{1}{n}\sum_{i=1}^{n}\frac{V_S\Delta_T^i(S)}{V_P\Delta_T^i(P)},$$

which yields R of about 5.5. Such a high value is compatible with the metastable model that was designed for this ratio. Note there is a whole-family of $\Delta\rho$ and K_s that will yield metastable Superdomes, Tan and Gurnis [2005] and resolving this number is essential in defining possible mineralogy.

Another measure of rapid changes in material properties is to use the shift, or Lateral Gradient Coefficient (LGC),

$$LGC = \frac{1}{n}\sum_{i=1}^{n}\frac{V_S \Delta_{LR}^{i}(S)}{V_P \Delta_{LR}^{i}(P)}$$

or perhaps their derivatives with represent to azimuth as displayed in Figure 4.11. Sharp changes in temperature usually yield similar changes in P and S velocities while chemistry is more effective in producing large coefficients. Averaging over the length of arrows in Figure 4.14 and Figure 4.15 for the same set of stations produces estimates greater than 8 where the P-waves are probably near the noise level. The arrow lengths in Figure 4.14a suggest azimuthal jumps of over 2 s/deg, which agree with those produced by the metastable model presented in Figure 4.9. We have not been able to explain such significant lateral gradients without introducing a wall, which is difficult to detect at periods greater than 20 s. In short, there appears to be a number of ways to quantify the obvious complexity introduced in Figure 4.1. Some small–scale features, especially prominent in the P-results given in Figure 4.15, appear to be associated with structure inside the Superdome. More data needs to be processed to establish such detail since other small–scale structures probably exist elsewhere in the Earth.

In summary, we have introduced a new method of processing array data which will make it easier to identify structural boundaries and sharpen tomographic images. The method decomposes observed pulses embedded in body wave observations and uses the relative timing of these array arrivals to identify in-the-plane vs. out-of-plane multi-pathing. Preliminary results for a few events observed by the South African Kaapvaal array reveal strong evidence of 3D wave propagation and the fine-scale nature of boundaries.

Appendix A

African Superdome and mid-mantle plume

After a detailed search for events that have suitable geometry for sampling the superdome edge and possible plume, we found four events (Figure 4.17) that could be analyzed as presented below. The record section in Figure A.1a covers the epicentral distances of 95° to 110°, where each record is plotted relative to PREM. Thus, each trace should start at zero time if the Earth is PREM-like and the event was properly located. However, since these four events are small, they are not well located, nor do they have accurate origin times. But because we are only interested in their relative travel times across the array, it does not cause a serious problem. Moreover, this array has been well studied, with only minor station corrections [*James et al.*, 2001]. Consequently, the travel time delay for stations south of about 100° by 5s is caused by earth structure, assumed to be the LLSVP. A 200 km layer with reduced S velocity of 3% produces 1s of SKS delay relative to PREM. Unfortunately, determining these delays accurately in the presence of noisy oceanic crustal events containing depth phases is difficult. In the first step, we determine or define an empirical source function which is a wavetrain most simple and common to the entire array by a cross-correlation search. The top trace was used in this case. We then generate a synthetic seismogram for a reference model, PREM, and determine the best Δ_{LR} for each record by a grid search along with the Δ_T travel time delay of the composite pulse relative to the reference model defined by Δ_T as discussed earlier. The Δ_Ts are displayed along with their surface projected geometric ray tracks. Note that the structure is roughly perpendicular to these paths producing roughly a 2D sampling. Many of these pulses are broad indicating multi-pathing which appears to be organized as presented in the bottom panels. Because these events are near the background noise, we can expect some artifacts in Δ_{LR}, however, by stacking results, we should highlight the strongest features. The simplest sample is displayed in (a) displaying some strong effects at the outer edge, $\Delta_{LR} \approx 4$ s, but a relatively uniform rise to over 4s delays. Event EPR3 in Figure A.1b and EPR4 in Figure A.1c both show a strong anomaly at the outer edge (normal timing) and at the upper edge with delays in Δ_{LR} of up to 3s. The results for EPR2 are presented in Figure A.1d which display some broadening at the larger ranges but these could be contaminated by SKPdS [*Garnero*, 2000]. However, the sharp delay Δ_T between 100° and 106° is particularly obvious, and is shifted about 4° relative to the results in Figure A.1b, which is compatible with our model prediction.

The height of the African Superdome structure remains an issue but some direct evidence is available [*Ni and Helmberger*, 2003b]. Although the geometry for sources and receivers is lacking for sampling the top of the Superdome with direct S, the phase SS can be used as proposed by these authors where one leg of the SS phase samples along the top of the LLSVP. The roughness of the upper structure also causes multi-pathing, as given in Figure A.2 for the SS phase.

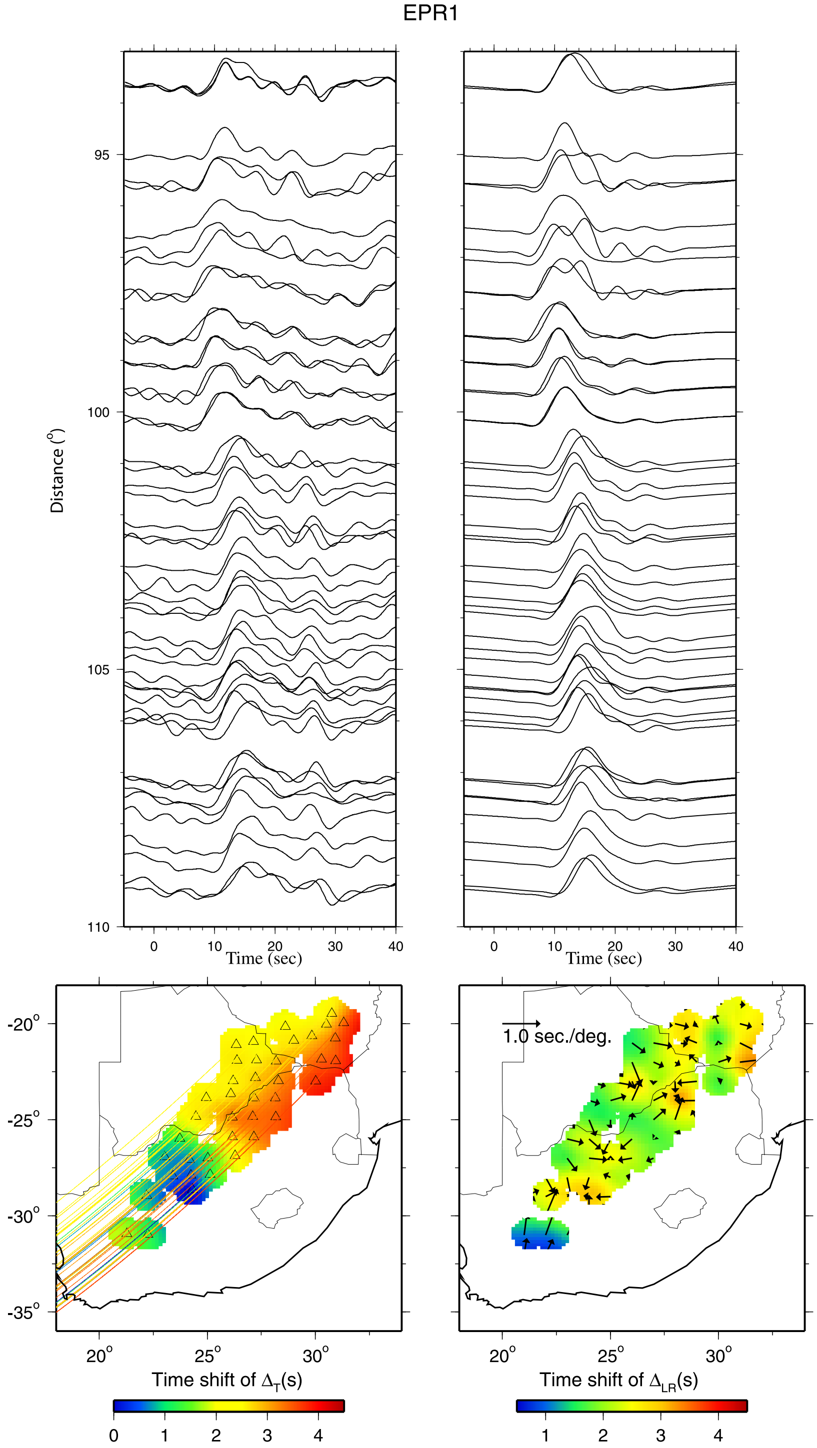
EPR1
Distance (°)
95
100
105
110
0
10
20
30
40
Time (sec)
0
10
20
30
40
Time (sec)
-20°
-25°
-30°
-35°
20°
25°
30°
Time shift of Δ_T(s)
0
1
2
3
4
1.0 sec./deg.
20°
25°
30°
Time shift of Δ_{LR}(s)
1
2
3
4

Figure A.1a

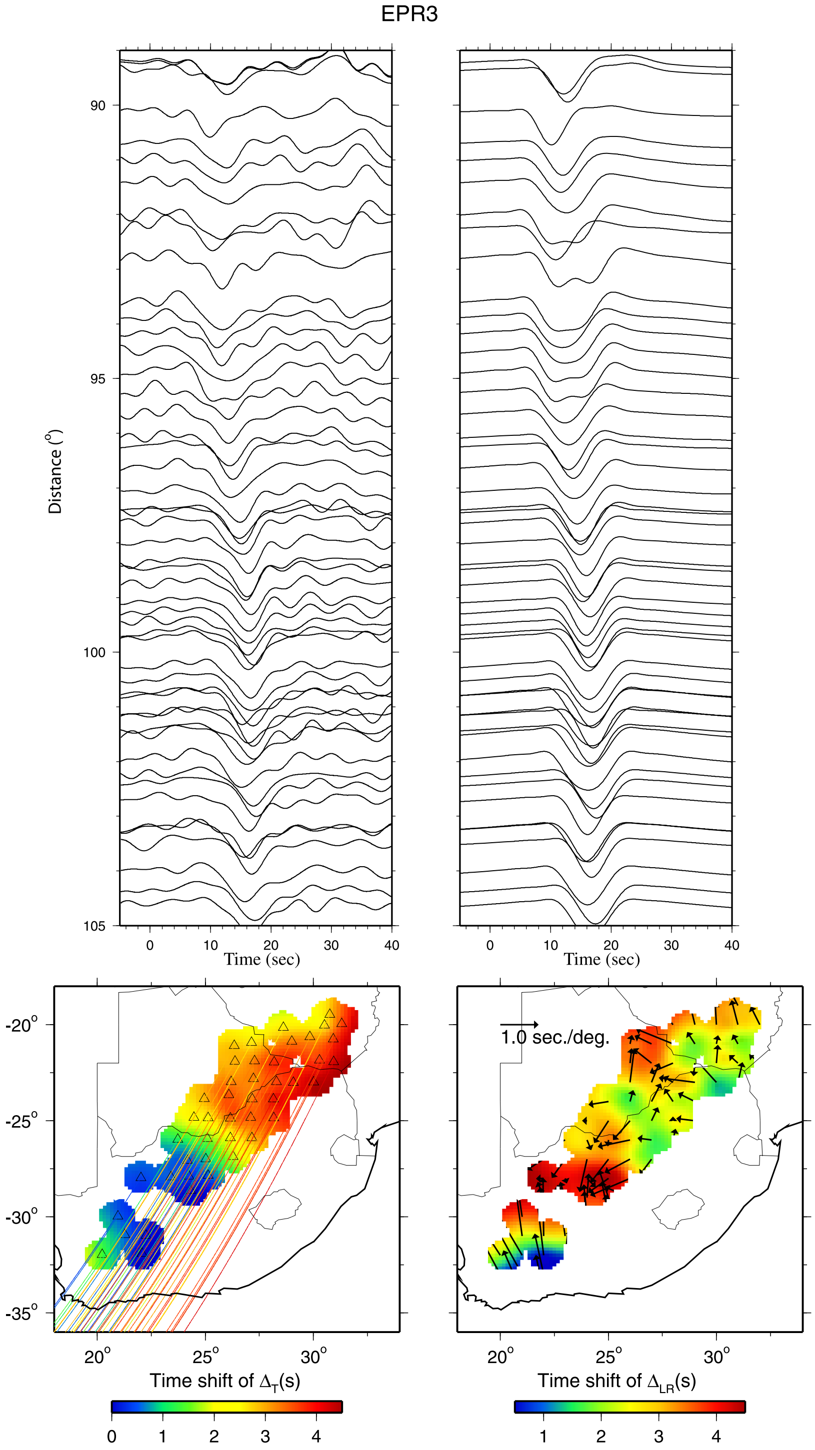
EPR3
Distance (°)
90
95
100
105
0
10
20
30
40
Time (sec)
-20°
-25°
-30°
-35°
20°
25°
30°
1.0 sec./deg.
Time shift of Δ_T(s)
0
1
2
3
4
Time shift of Δ_{LR}(s)
1
2
3
4

Figure A.1b

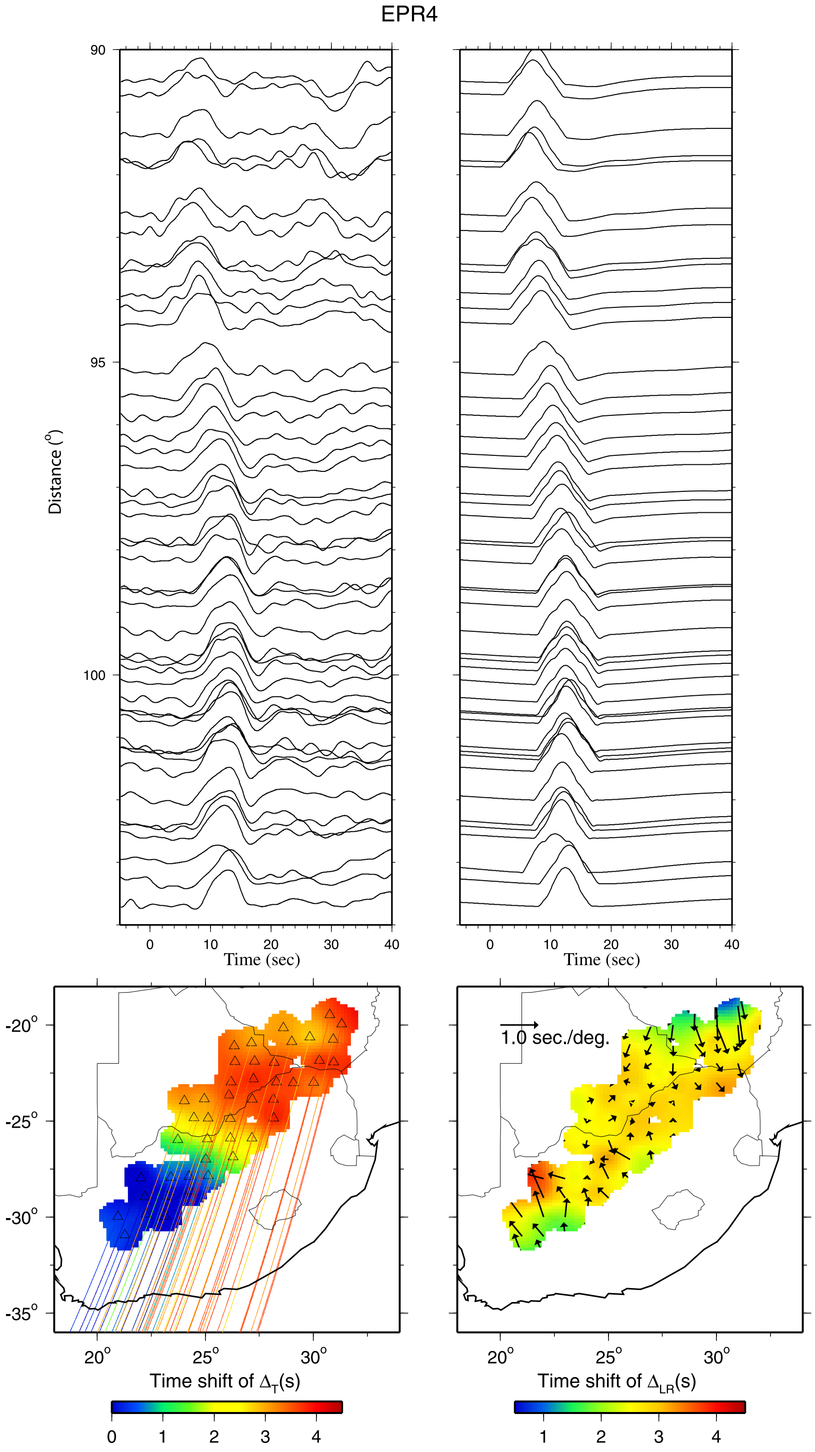
EPR4
90
95
100
Distance (°)
0
10
20
30
40
Time (sec)
0
10
20
30
40
Time (sec)
-20°
-25°
-30°
-35°
20°
25°
30°
Time shift of Δ_T(s)
0
1
2
3
4
1.0 sec./deg.
20°
25°
30°
Time shift of Δ_{LR}(s)
1
2
3
4

Figure A.1c

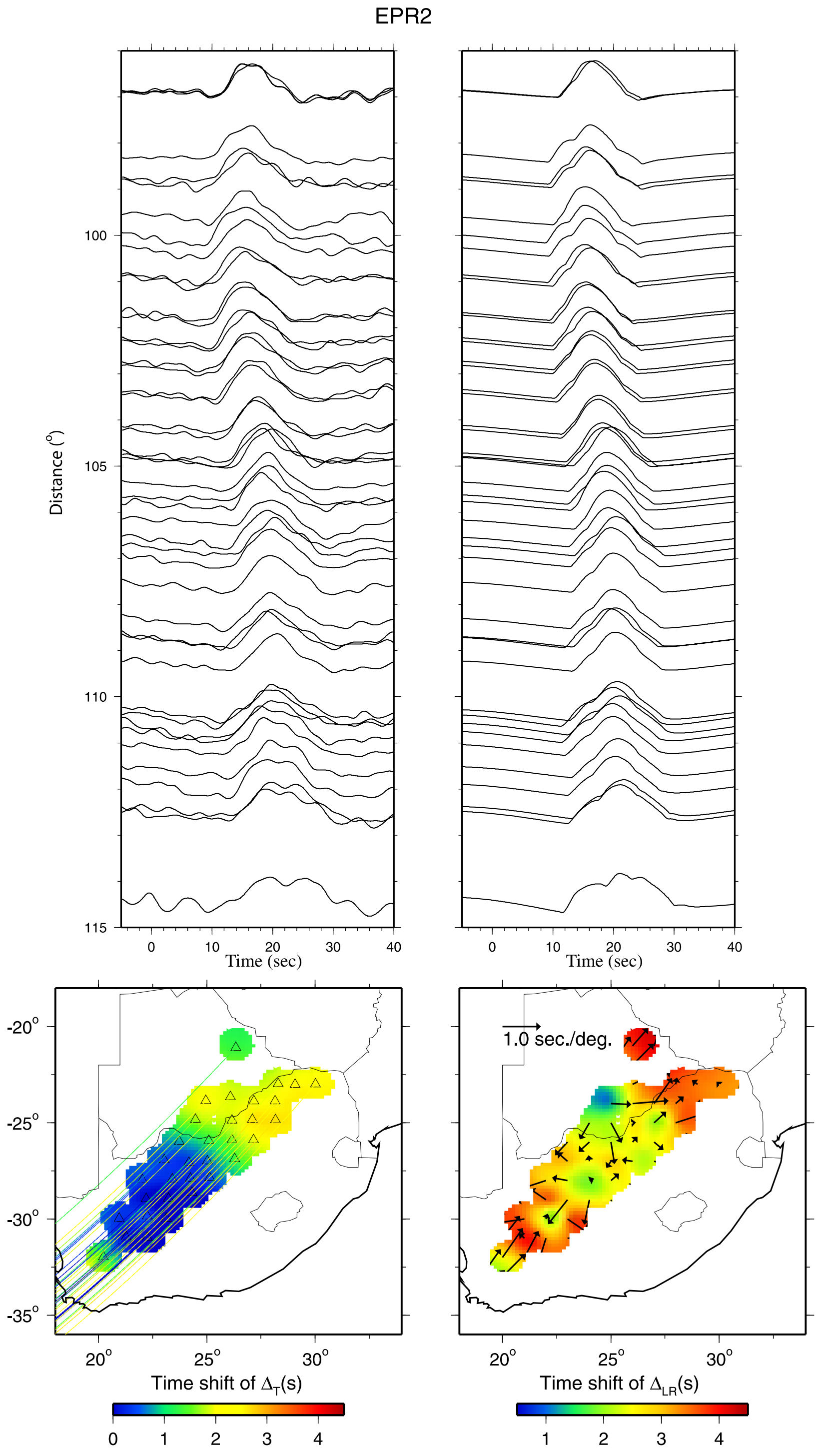

Figure A.1d

Figure A.1: MPD pattern for four East Pacific-Rise events recorded by Kaapvaal Array in South Africa

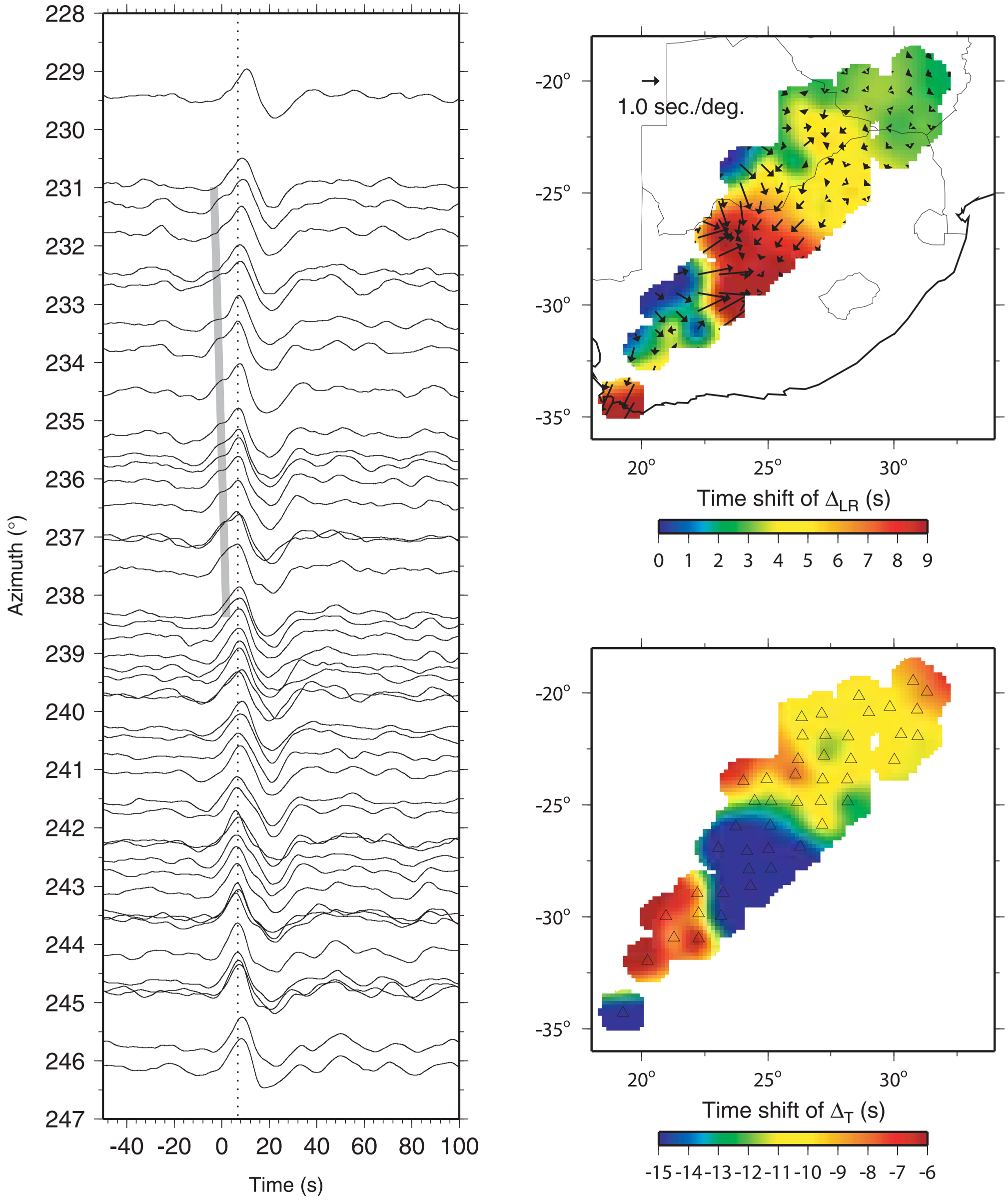

Figure A.2: This record section is a continuation of the same event given in Figure 4.12 but aligned on the SS travel time predictions (PREM). The epicentral distance spans 112° to 119° so that the SS phase is sampling a depth near 2000 km [*Ni et al.*, 2005]. Many of these pulses are relatively fat, i.e., 238°–232°, which produces multi-pathing as displayed on the right. The bright red patch in Δ_{LR} can be interpreted as a fast ridge relative to the slow anomaly as in Figure 4.16b

Bibliography

Akber-Knutson, S., G. Steinle-Neumann, and P. D. Asimow (2005), Effect of Al on the sharpness of the MgSiO3 perovskite to post-perovskite phase transition, *Geophys. Res. Lett*, *32,* L1403, doi:10.1029/2005GL023192.

Aki, K., and P. G. Richards (2002), *Quantitative Seismology, 2nd ed.*, Univ. Sci., Sausalito, Calif.

Anderson, D. L. (2002), The case for irreversible chemical stratification of the mantle, *Int. Geology Rev.*, *44*(2), 97–116.

Anderson, D. L. (2005), Scoring hotspots: The plume and plate paradigms, in *Plate, plumes, and paradigms*, edited by G. R. Foulger, et al., , *Geol. Soc. Am. Spec. Pap.*, *388*, 31–54.

Bunge, H. P., C. R. Hagelberg, and B. J. Travis(2003), Mantle circulation models with variational data assimilation: inferring past mantle flow and structure from plate motion histories and seismic tomography, *Geophys. J. Int.*, *152*, 280–301.

Chapman, C. H. (1976), Exact and approximate generalized ray theory in vertically inhomogeneous-media, *Geophys. J. R. Astro. Soc.*, *46*, 201–233.

Chapman, C. H. (2004), *Fundamentals of Seismic Wave Propagation*, p. 632, Cambridge Univ. Press, New York.

Christensen, U. (1984), Instability of a hot boundary-layer and initiation of thermo-chemical plume, *Ann. Geophys.*, *2*, 311–319.

Davaille, A. (1999), Simultaneous generation of hotspots and superswells by convection in a heterogenous planetary mantle, *Nature*, *402*(6763), 756–760.

Ding, X. M., and D. V. Helmberger (1997), Modelling D″ structure beneath Central America with broadband seismic data, *Phys. Earth Planet Inter.*, *101*(3–4), 245–270.

Duffy, T. S. (2004), Earth science—Deeper understanding, *Nature*, *430*(6998), 409–410.

Dziewonski, A. M., and D. L. Anderson (1981), Preliminary Reference Earth Model, *Phys. Earth Planet. Inter.*, *25*, 297–356.

Flores, C., and T. Lay (2005), The trouble with seeing double, *Geophys. Res. Lett.*, *32*, L24305, doi:10.1029/2005GL024366.

Garnero, E. J., and T. Lay (1997), Lateral variations in lowermost mantle shear wave anisotropy beneath the north Pacific and Alaska, *J. Geophys. Res.*, *102*(B4), 8121–8135.

Garnero, E. J., J. Revenaugh, Q. Williams, T. Lay and L. H. Kellogg (1998), Ultralow velocity zone at the core-mantle boundary, in *The Core-Mantle Boundary Region, Geodyn. Ser*, vol. 28, edited by M. Gurnis et al., pp. 273–297, AGU, Washington, D.C.

Garnero, E. J. (2000), Heterogeneity of the lowermost mantle, *Annu. Rev. Earth Planet. Sci.*, *28*, 509–537.

Garnero, E. J., and T. Lay (2003), D″ shear velocity heterogeneity, anisotropy and discontinuity structure beneath the Caribbean and Central America, *Phys. Earth Planet Inter.*, *140*(1–3), 219–242.

Garnero, E. J. (2004), A new paradigm for Earth's core-mantle boundary, *Science*, *304*(5672), 834–836.

Gilbert, F., and D. V. Helmberger (1972), Generalized ray theory for a layered sphere, *Geophys. J. R. Astron. Soc.*, *27*, 57–80.

Gonnermann, H. M., M. Manga, and A. M. Jellinek (2002), Dynamics and longevity of an initially stratified mantle, *Geophys. Res. Lett.*, *29*(10), 1399, doi:10.1029/2002GL014851.

Grand, S., and D. V. Helmberger (1984), Upper mantle shear structure of North America, *Geophys. J. R. Astron. Soc.*, *76*, 399–438.

Grand, S. P. (1994), Mantle shear structure beneath the Americas and surrounding oceans, *J. Geophys. Res.*, *99*(B6), 11,591–11,621, doi:10.1029/94JB00042.

Grand, S. P., R. D. van der Hilst, and S. Widiyantoro (1997), Global seismic tomography: A snapshot of convection in the earth, *GSA Today*, *7*, 1–7.

Grand, S. P. (2002), Mantle shear-wave tomography and the fate of subducted slabs, *Phil. Trans. R. Soc. London, Ser. A*, *360*(1800), 2475–2491.

Griffiths, R. W., and I. H. Campbell (1991), On the dynamics of long-lived plume conduits in the convecting mantle, *Earth Planet. Sci. Lett.*, *103*(1–4), 214–227.

Gurnis, M., M. E. Wysession, E. Knittle and B. A. Buffett (Eds.) (1998), *The Core-Mantle Boundary Region, Geodynamics Series, veol 28*, p. 334, AGU, Washington, D. C.

Hansen, U., and D. A. Yuen (1989), Dynamical influences from thermal-chemical instabilities at the core-mantle boundary, *Geophys. Res. Lett.*, *16*(7), 629–632.

He, Y. M., L. X. Wen, and T. Y. Zheng (2006), Geographic boundary and shear wave velocity structure of the “Pacific anomaly” near the core-mantle boundary beneath western Pacific, *Earth Planet. Sci. Lett.*, *244*(1–2), 302–314.

Helmberger, D., T. Lay, S. Ni and M. Gurnis (2005), Deep mantle structure and the postperovskite phase transition, *Proc. Natl. Acad. Sci. U. S. A.*,, *102*(48), 17257–17263.

Helmberger, D. V., and S. Ni (20051), Approximate 3D bodywave synthetics for tomographic models, *Bull. Seismol. Soc. Am.*, *95*(1), 212–224.

Helmberger, D. V., and S. D. Ni (2005b), Seismic modeling constraints on the South African Super Plume, in *Earth's Deep Mantle: Structure, Composition, and Evolution, Geophys. Monogr. Ser.*, vol. 160, edited by R. D. van der Hilst et al., pp. 65–84, AGU, Washington, D.C.

Hernlund, J. W., and S. Labrosse (2007), Geophysically consistent values of the perovskite to post-perovskite transition Clapeyron slope, *Geophys. Res. Lett.*, *34*, L05309, doi:10.1029/2006GL028961.

Hernlund, J. W., C. Thomas, and P. J. Tackley (2005), A doubling of the post-perovskite phase boundary and structure of the Earth's lowermost mantle, *Nature*, *434*(7035), 882–886.

Hirose, K. (2006), Postperovskite phase transition and its geophysical implications, *Rev. Geophys.*, *44*, RG3001, doi:10.1029/2005RG000186.

Hutko, A. R., T. Lay, E. J. Garnero, and J. Revenaugh (2006), Seismic detection of folded, subducted lithosphere at the core-mantle boundary, *Nature*, *441*(7091), 333–336.

James, D. E., M. J. Fouch, J. C. VanDecar, S. van der Lee, and Kaapvaal Seismic Group (2001), Tectospheric structure beneath southern Africa, *Geophys. Res. Lett.*, *28*, 2485–2488.

Karato, S., and B. B. Karki (2001), Origin of lateral variation of seismic wave velocities and density in the deep mantle, *J. Geophys. Res.*, *106*(B10), 21,771–21,783.

Kellogg, L. H., B. H. Hager, and R. D. van der Hilst, (1999), Compositional stratification in the deep mantle, *Science*, *283*(5409), 1881–1884.

Kendall, J. M., and P. M. Shearer (1994), Lateral variations in D″ thickness from long period shear-wave data, *J. Geophys. Res.*, *99*(B6), 11,575–11,590.

Komatitsch, D., and J. Tromp (2002a), Spectral-element simulations of global seismic wave propagation: I. Validation, *Geophys. J. Int.*, *149*, 390–412, doi:10.1046/j.1365-246X.2002.01653.x.

Komatitsch, D., and J. Tromp (2002b), Spectral-element simulations of global seismic wave propagation: II. 3D models, oceans, rotation, and gravity, *Geophys. J. Int.*, *150*, 303–318, doi:10.1046/j.1365-246X.2002.01716.x.

Langston, C. A., et al. (2002), Regional wave propagation in Tanzania, East Africa, *J. Geophys. Res.*, *107*(B1), doi:10.1029/2001jb000167

Lay, T., and D. V. Helmberger (1983), A lower mantle S-wave triplication and the shear velocity structure of D, *Geophys. J. R. Astron. Soc.*, *75*(3), 799–837.

Lay, T. (1986), Evidence of a lower mantle shear velocity discontinuity in S and sS phases, *Geophys. Res. Lett.* , *13*(13), 1493–1496.

Lay, T., Q. Williams, and E. J. Garnero (1998), The core-mantle boundary layer and deep Earth dynamics, *Nature*, *392*(6675), 461–468.

Lay, T., J. Hernlund, E. J. Garnero, and M. S. Thorne (2006), A post-perovskite lens and D″ heat flux beneath the central Pacific, *Science*, *314*(5803), 1272–1276.

Lay, T., and E. J. Garnero (2007), Reconciling the Post-perovskite phase with seismological observations of lowermost mantle structure, in *Post-perovkiste: The Last Mantle Phase Transition, Geophys. Monogr. Ser. 174*, edited by K. Hirose, et al., AGU, Washington, D. C.

Lee, K. K., et al. (2005), Phase assemblage and stability of pyroxenite at Lower-Mantle conditions, *EOS Trans AGU*, *86*(V42A-02).

Loper, D. E., and F. D. Stacey (1983), The dynamical and thermal structure of deep mantle plumes, *Phys. Earth Planet Inter.*, *33*(4), 304–317.

Luo, S. N., et al. (2001), Evidence for a sharp lateral variation of velocity at the core-mantle boundary from multipathed PKPab, *Earth Planet. Sci. Lett.*, *189*(3–4), 155–164.

Masters, G., G. Laske, H. Bolton, and A. M. Dziewonski (2000), The relative behavior of shear velocity, bulk sound speed, and compressional velocity in the mantle: Implications for chemical and thermal structure, in *Earth's Deep Interior: Mineral Physics and Tomography From the Atomic to the Global Scale*, *Geophys. Monogr. Ser.*, vol. 117, edited by S. Karato et al., pp. 63–87, AGU, Washington, D. C.

Masters G, L. G., Bolton H, Dziewonski, AM (Ed.) (2000), in *Earth's Deep Interior: Mineral Physics and Tomography From the Atomic to the Global Scale, Geophys. Monogr. Ser., Vol. 117*, p. 289, AGU, Washington, D. C.

Matzel, E., M. K. Sen, and S. P. Grand (1996), Evidence for anisotropy in the deep mantle beneath Alaska, *Geophys. Res. Lett.*, *23*(18), 2417-2420.

McNamara, A. K., and S. Zhong (2004), Thermochemical structures within a spherical mantle: Superplumes or piles?, *J. Geophys. Res.*, *109*, B07402.

McNamara, A. K., and S. J. Zhong (2005), Thermochemical structures beneath Africa and the Pacific Ocean, *Nature*, *437*(7062), 1136–1139.

Montelli, R., G. Nolet, F. A. Dahlen, G. Masters, E. R. Engdahl, and S. H. Hung (2004), Finite-frequency tomography reveals a variety of plumes in the mantle, *Science*, *303*(5656), 338–343.

Montelli, R., G. Nolet, F. A. Dahlen and G. Masters, (2006), A catalogue of deep mantle plumes: New results from finite-frequency tomography, *Geochem. Geophys. Geosyst.*, *7,* doi: 10.1029/2006gc001248.

Murakami, M., K. Hirose, K. Kawamura, N. Sata, and Y. Ohishi (2004), Post-perovskite phase transition in MgSiO3, *Science*, *304*(5672), 855–858.

Ni, S. D., V. F. Cormier, and D. V Helmberger (2003), A comparison of synthetic seismograms for 2D structures: Semianalytical versus numerical, *Bull. Seismol. Soc. Am.*, *93*(6), 2752–2757.

Ni, S. D., X. M. Ding, and D. V. Helmberger (2000), Constructing synthetics from deep earth tomographic models, *Geophys. J. Int.*, *140*(1), 71–82.

Ni, S. D., E. Tan, M. Gurnis, and D. Helmberger (2002), Sharp sides to the African Superplume, *Science*, *296*(5574), 1850–1852.

Ni, S., and D. V. Helmberger (2003a), Seismological constraints on the South African Superplume: Could be the oldest distinct structure on Earth, *Earth Planet. Sci. Lett.*, *206*, 119–131.

Ni, S., and D. V. Helmberger (2003b), Further constraints on the African Superplume structure, *Phys. Earth Planet. Inter.*, *140*, 243–251.

Ni, S., and D. V. Helmberger (2003c), Ridge-like lower mantle structure beneath South Africa, *J. Geophys. Res.*, *108*(B2), 2094, doi:10.1029/2001JB001545.

Ni, S., D. V. Helmberger, and J. Tromp (2005), 3D structure of the African super plume from waveform modeling, *Geophys. J. Int.*, *161*, 283–294, doi:10.1111/j.1365-246X.2005.02508.x.

Oganov, A. R., J. P. Brodholt, and G. D. Price (2001), The elastic constants of MgSiO3 perovskite at pressures and temperatures of the Earth's mantle, *Nature*, *411*(6840), 934–937.

Ohta, K., K. Hirose, T. Lay, N. Sata, and Y. Ohishi (2008), Phase transitions in pyrolite and MORB at lowermost mantle conditions: Implications for a MORB-rich pile above the core-mantle boundary, *Earth Planet. Sci. Lett.*, *267*(1–2), 107–117.

Olson, P., and H. Singer (1985), Creeping plumes, *J. of Fluid Mech.*, *158*(9), 511–531.

Revenaugh, J., and R. Meyer (1997), Seismic evidence of partial melt within a possibly ubiquitous low-velocity layer at the base of the mantle, *Science*, *277*(5326), 670–673.

Ritsema, J., S. Ni, D. V. Helmberger, and H. P. Crotwell (1998), Evidence for strong shear velocity reductions and velocity gradients in the lower mantle beneath Africa, *Geophys. Res. Lett.*, *25*(23), 4245–4248.

Ritsema, J., H. J. van Heijst, and J. H. Woodhouse (1999), Complex shear wave velocity structure imaged beneath Africa and Iceland, *Science*, *286*, 1925–1928.

Ritsema, J., A. K. McNamara, and A. L. Bull (2007), Tomographic filtering of geodynamic models: Implications for model interpretation and large-scale mantle structure, *J. Geophys. Res.*, *112*, B01303, doi:10.1029/2006JB004566.

Russell, S. A., T. Lay, and E.J. Garnero (1998), Seismic evidence for small-scale dynamics in the lowermost mantle at the root of the Hawaiian hotspot, *Nature*, *396*(6708), 255–258.

Russell, S. A., T. Lay, and E.J. Garnero (1999), Small-scale lateral shear velocity and anisotropy heterogeneity near the core-mantle boundary beneath the central Pacific imaged using broadband ScS waves, *J. Geophys. Res.*, *104*(B6), 13183–13199.

Scott, P., and D. V. Helmberger (1985), Applications of the transmitted Kirchhoff-Holmholtz method to transmitted body waves and possible structural effects at NTS, *Bull. Seismol. Soc. Am.*, *75*, 131–156.

Shearer, P. (1993), Global mapping of upper mantle reflectors from long-period SS precursors, *Geophys. J. Int.*, *115*, 878–904, doi:10.1111/j.1365-246X.1993.tb01499.x.

Sidorin, I., M. Gurnis, D. V. Helmberger, and X. M. Ding (1998), Interpreting D″ seismic structure using synthetic waveforms computed from dynamic models, *Earth Planet. Sci. Lett.*, *163*(1–4), 31–41.

Sidorin, I., M. Gurnis, and D. V. Helmberger (1999), Evidence for a ubiquitous seismic discontinuity at the base of the mantle, *Science*, *286*(5443), 1326–1331.

Simmons, N. A., and S. P. Grand (2002), Partial melting in the deepest mantle, *Geophys. Res. Lett.*, *29*(11).

Song, T. R., and D. V. Helmberger (2007), Validating tomographic model with broadband waveform modeling: An example from the LA RISTRA transect in the southwestern United States, *Geophys. J. Int.*, *171*, 244–258, doi:10.1111/j.1365-246X.2007.03508.x.

Song, X. D., and D. V. Helmberger (1993), Effect of velocity structure in D" on PKP phases, *Geophys. Res. Lett.*, *20*(4), 285–288.

Souriau, A., and J. H. Woodhouse (1985), A worldwide comparison of predicted S-wave delays from a three-dimensional upper mantle model with P wave station corrections, *Phys. Earth Planet. Inter.*, *39*, 75–88.

Su WJ, D. A. (1997), Simultaneous inversion for 3-D variations in shear and bulk velocity in the mantle, *Phys. Earth Planet. Inter.*, *100*, 135–156.

Sun, D. Y., T. R. A. Song, and D. Helmberger (2006), Complexity of D″ in the presence of slab-debris and phase changes, *Geophys. Res. Lett.*, *33*, L12S07, doi:10.1029/2005GL025384.

Sun, D., E. Tan, D. V. Helmberger, and M. Gurnis (2007a), Seismological support for the metastable Superplume model, sharp features, and phase changes, within the lower mantle, *Proc. Natl. Acad. Sci. U. S. A.*, *104*(22), 9151–9155.

Sun, X. L., D. X. Song, S. H. Zheng, and D. V. Helmberger (2007b), Evidence for a chemical-thermal structure at base of mantle from sharp lateral *P* wave variations beneath Central America, *Proc. Natl. Acad. Sci. U. S. A.*, *104*(1), 26–30.

Sun, D., D. Helmberger, X. Song, and S. P. Grand (2007c), Predicting a global Perovskite to Post-Perovskite phase boundary, in *Post-perovkiste: The Last Mantle Phase Transition, Geophys. Monogr. Ser. 174*, edited by K. Hirose, et al., pp. 155-170, AGU, Washington, D. C.

Sun, D., D. Helmberger (2008), Lower mantle tomography and phase change mapping, *J. Geophys. Res.*, 113, B10305, doi:10.1029/2007JB005289.

Sun, D., D. Helmberger, S. Ni, and D. Bower (2009), Direct measures of lateral velocity variation in the deep Earth, *J. Geophys. Res.*, 114, B05303, doi:10.1029/2008JB005873.

Tackley, P. (2000), Mantle convection and plate tectonics: Toward an integrated physical and chemical theory, *Science*, *288*, 2002–2007.

Tan, E., M. Gurnis, and L. J. Han (2002), Slabs in the lower mantle and their modulation of plume formation, *Geochem. Geophys. Geosyst.*, *3*(11), 1067, doi:10.1029/2001GC000238.

Tan, E., and M. Gurnis (2005), Metastable Superplumes and mantle compressibility, *Geophys. Res. Lett.*, *32*, L20307, doi:10.1029/2005GL024190.

Tan, E., and M. Gurnis (2007), Compressible thermochemical convection and application to lower mantle structures, *J. Geophys. Res.*, *112*, B06304, doi:10.1029/2006JB004505.

Tape, C., Q. Liu, and J. Tromp (2007), Finite-frequency tomography using adjoint methods: Methodology and examples using membrane surface waves, *Geophys. J. Int.*, *168*, 1105–1129, doi:10.1111/j.1365-246X.2006.03191.x.

Thomas, C., J. Garnero, and T. Lay (2004), High-resolution imaging of lowermost mantle structure under the Cocos plate, *J. Geophys. Res.*, *109*(B8), B08307, doi:10.1029/2004JB003013.

Thomas, C., J. Wookey, and M. Simpson (2007), D″ anisotropy beneath Southeast Asia, *Geophys. Res. Lett.*, *34*, L04301, doi:10.1029/2006GL028965.

Thorne, M. S., T. Lay, E. J. Garnero, G. Jahnke, and H. Igel (2007), Seismic imaging of the laterally varying D″ region beneath the Cocos Plate, *Geophys. J. Int.*, *170*(2), 635–648, doi:10.1111/j.1365-246X.2006.03279.x.

Tsuchiya, T., and J. Tsuchiya (2006), Effect of impurity on the elasticity of perovskite and postperovskite: Velocity contrast across the postperovskite transition in (Mg,Fe,Al)(Si,Al)O-3, *Geophys. Res. Lett*, *33*, doi: 10.1029/2006gl025706.

van der Hilst, R. D. (2004), Geophysics—Changing views on Earth's deep mantle, *Science*, *306*(5697), 817–818.

van der Hilst, R., M. V. de Hoop, P. Wang, S.-H. Shim, P. Ma, and L. Tenorio (2007), Seismostratigraphy and thermal structure of Earth's core-mantle boundary region, *Science*, *315*(5820), 1813–1817

Wang, P., M. V. deHoop, R. D. vanderHilst, P. Ma, and L. Tenorio (2006), Imaging of structure at and near the core mantle boundary using a generalized radon transform: 1. Construction of image gathers, *J. Geophys. Res.*, *111*, B12304,doi:10.1029/2005JB004241.

Wang, Y., and L. Wen (2007), Geometry and P and S velocity structure of the “African Anomaly”, *J. Geophys. Res.*, *112*, B05313, doi:10.1029/2006JB004483.

Wen, L. (2001), Seismic evidence for a rapidly varying compositional anomaly at the base of the Earth's mantle beneath the Indian Ocean, *Earth Planet. Sci. Lett.*, *194*, 83–95

Wen, L. X., P. Silver, D. James, and R. Kuehnel (2001), Seismic evidence for a thermo-chemical boundary at the base of the Earth's mantle, *Earth Planet. Sci. Lett.*, *189*(3–4), 141–153.

Wiggins, R. A., and J. A. Madrid (1974), Body wave amplitude calculations, *Geophys. J. R. Astron. Soc.*, *37*(3), 423–433.

Wysession, M. E., et al. (1998), The D″ discontinuity and its implications, in *The Core-Mantle Boundary Region*, *Geodyn. Ser*, vol. 28, edited by M. Gurnis et al., pp. 273–297, AGU, Washington, D.C.

Zhu, L. P., and D. V. Helmberger (1998), Moho offset across the northern margin of the Tibetan Plateau, *Science*, *281*(5380), 1170–1172.